An Examination of Design Practices for Mixing Tanks Using Computational Fluid Dynamics

Nicodemus B. Muchemu

Submission date: May 2023

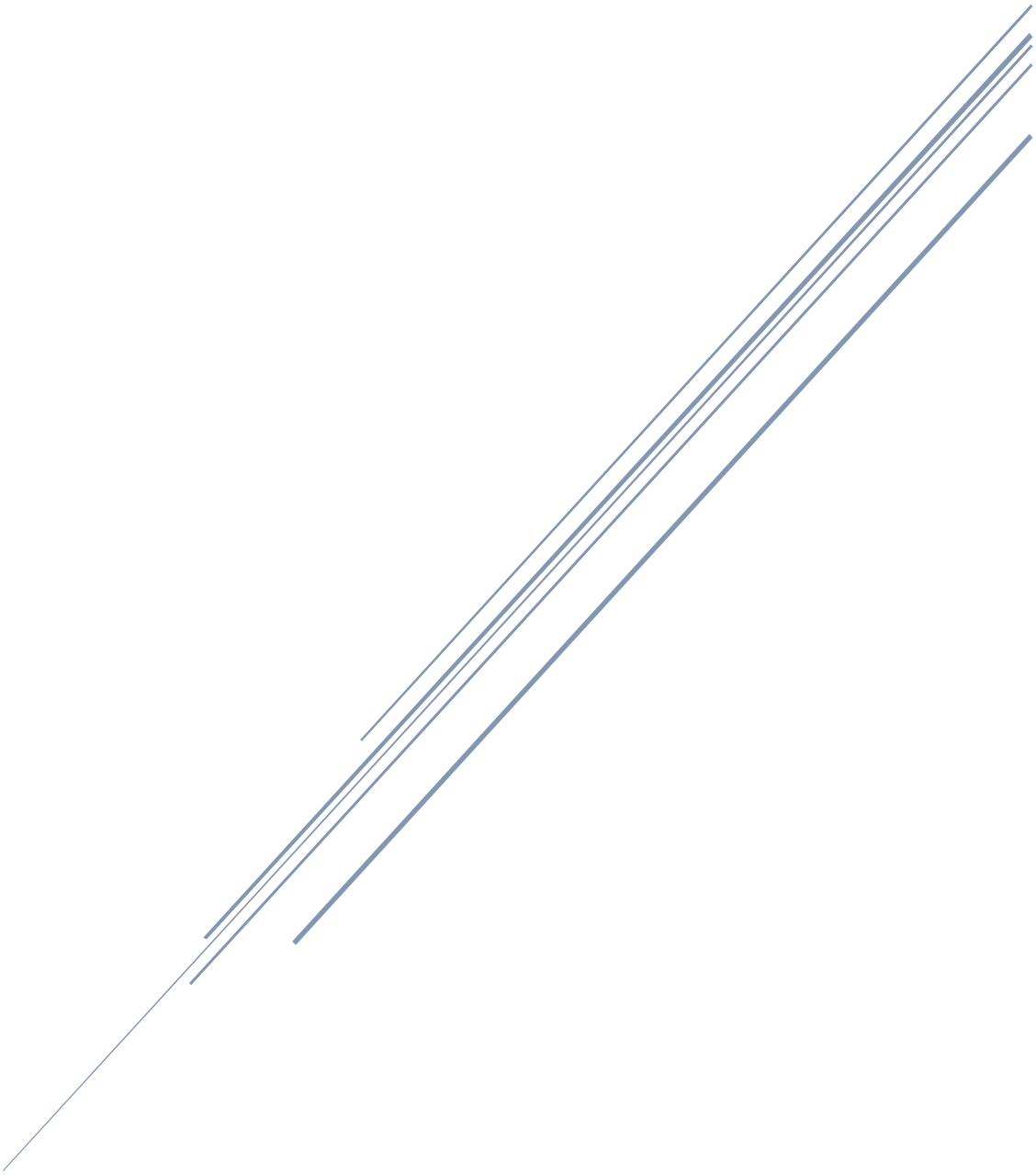

University of Huddersfield
PhD Chemical Engineering

Copyright statement

Acknowledgements

I am grateful for the help offered by Lande Liu as my main supervisor throughout the project. John Chai and Viacheslav Stetsyuk also provided some help and feedback when writing publications. I would also like to offer thanks to the University library for providing access to articles and books for research.

Publications

Nicodemus Muchemu, Lande Liu, 2022, Mixing Tank with Baffles: A CFD Approach Towards Baffle Design, Chemical Engineering Research and Design, Submitted.

Nicodemus Muchemu, Lande Liu, Viacheslav Stetsyuk, John Chee Chai, 2019, Turbulence modelling of mixing tanks: A review, Trends in Chemical Engineering, 17, 37-50

Declaration

Certain sections of this thesis were used in articles that I submitted for publication.

List of sections

- Analysis of Fluid Flow
- General Structure of Stirred Tank Reactors
- Some Commonly Used Equations in Mixing Tank Analysis
- Conservation Equations
- Eddy Viscosity Models
- Eddy Viscosity Models for RANS
- k-ε Model
- Factor analysis and principal component analysis
- Simulation results with optimised mesh size and convergence criterion
- Effect of baffle size on flow
- Effect of baffle shape on fluid flow

Abstract

Background and Objectives

This thesis examines design practices of mixing tanks with baffles using the tools of computational fluid dynamics in a technique known as a multiple reference frame analysis. The goal of this thesis is to optimise the simulation process as well as to examine the effect of varying the impeller size and shape on fluid flow within the confines of a mixing tank. This was done for both a single-phase flow (water) and a multiphase flow (crude oil and water mixture).

Methods and Results

A model tank of cylindrical shape of height to diameter ratio of 1:1 was used in the simulation. The diameter of the proposed mixing tank design was 1.08 m with the tank diameter being based on a mixing tank from an industrial supplier. AutoCAD was then used to construct this geometric shape. The model tank has a paddle blade impeller operating at a clearance of 0.36 m and diameter of 0.54 m with a moving fluid zone surrounding the agitator paddles. The tank also has two baffles on either side of the agitator with each of them having a width of 0.18 m and thickness of 0.045 m. Ansys workbench was used to further process this geometric model with Boolean operation to remove the solid regions within the mixing tank and separate the moving and stationary fluid zones.

Principal component analysis based factor analysis approach was used to optimise the element size and residual to stabilise the convergence and accuracy. The optimised element size was found to be 1.34 cm and 1.3×10^{-3} was found to be the optimised residual value for the CFD simulation.

Baffle dimensions were proposed based on their effect on fluid flow patterns and were labelled according to baffle length to width ratios. The $2{:}\,1$ baffle $(0.36\ \text{m}{:}\ 0.18\ \text{m})$ was found to be the most suitable when analysing pressure and velocity profiles at different regions within the mixing tank.

With the baffle ratio of $2{:}\,1$, three shapes with the same baffle length were constructed: rectangle (standard), normal distribution and error functions based were simulated. When observing average pressure and various velocity profiles at specified locations, the normal distribution curve was seen to produce the best mixing results. In particular, at the horizontal line location labelled x-axis line location, the pressure profile for the normal distribution curve had the largest maxima and minima at 208217.1 Pa and -458357 Pa respectively with an average pressure value of -115047 Pa. In contrast, the average pressure values for the error and standard baffle configurations respectively were -52345.8 Pa and -57675.5 Pa. The same pattern of the normal distribution shape producing better mixing results was consistently observed with the rest of the pressure and velocity profiles provided at different locations.

To examine the viability of proposed baffle designs in multiphase mixing, 10% volume of water and 90% volume of Conroe crude oil was introduced to the mixing tank for the simulation for baffles of the proposed shapes. They were the modelled using the Eulerian multiphase model under the optimised settings. The average water volume fractions at different regions of the mixing tank were used to determine the dispersion quality of each baffle design. The normal distribution baffle had an average volume fraction of 2.2×10^{-3} at the distance furthest from the impeller paddles. This implied that of the 3 baffle configurations, for water to disperse in crude oil the normal distribution shape produced the best quality of dispersion.

Conclusions

Of the proposed rectangle (standard) baffle designs, the $2:1$ baffle configuration was found to be the most suitable from the profile analyses when operating at the optimised CFD settings. Likewise, of the proposed shapes the normal distribution baffle configuration was fluid to be the most suitable for both multiphase and single-phase mixing.

Contents

List of Tables

1 Introduction

Due to the prevalence of mixing tanks in industries an understanding of their structure and how this affects flow patterns and mixing quality can be invaluable when it comes to minimizing power draw and maximising production output. As such, a great amount of research has been carried out in this field. This includes experimental studies on scaled down models to determine the efficacy of specific geometric configurations via means of particle image velocimetry as well as via computational means otherwise referred to as computational fluid dynamics (CFD). An understanding of the underlying transport equations in any given CFD program can enable a wide variety of analytical uses that are not limited to mixing tank analysis including turbomachinery analysis and aerofoil studies.

Within this thesis, an examination of modelling practices of stirred tank reactors has been undertaken. There is a particular focus on the use of the multiple reference technique (MRF) to model fluid flow within the mixing tank. Aside from this, the simulation itself can consume a lot of computational resources, as a result it can be useful to optimise the simulation process. This attempted to reduce the time taken to run a simulation while maintaining a reasonable level of accuracy.

Further, this thesis will attempt to examine the effect of internals on fluid flow. This will involve analysing how different baffle shapes and sizes effect how fluids move within the system.

Stirred tank reactors are usually used in multiphase mixing, whether particle-fluid or fluid-fluid. CFD techniques can be used to model multiphase flows within stirred tank reactors. As such, an attempt was made to model the flow and mixing of water in crude oil.

Initially, this thesis was going to involve the experimental analysis of a stirred tank reactor. The intention was to use a scaled down stirred tank reactor based on the dimensions of the simulated stirred tank reactor and compare the experimental to the simulated results of a crude oil and water mixture. However, due to the COVID-19 pandemic, the sourcing of the experimental material proved impossible. As a result, the decision was made to focus on simulation work.

Research question

How can one optimise the simulation setup for a bespoke mixing tank design?

What is the ideal baffle size and shape for bespoke mixing tank for single-phase mixing?

What is the ideal baffle shape for multiphase mixing within the proposed mixing tank design?

Project Objectives

Thus, what this thesis seeks to design an optimisation scheme for the simulation of a novel mixing design. Following on from this, examine the effect of baffle size on a single-phase (water) fluid flow and use the various pressure and velocity profiles at various locations within the mixing tank to determine the most ideal (optimum) baffle size. Upon arriving at the ideal size, various baffle shapes of identical baffle lengths will be analysed to determine their effect on fluid flow within the mixing tank for both single and multiphasic flows and determine the ideal baffle shape.

2 Literature Review

2.1 Analysis of Fluid Flow

The analysis of fluid flow, mass transfer and heat transfer are critical components in industry. This is because understanding the interactions of fluids with other fluids or solid objects is a crucial part of optimisation. The process of fluid dynamic examination has enabled an increase in efficiency and thereby increasing the quantity and quality of products produced in various fields ranging from biochemistry to pharmacy as well as more mechanically aligned fields such as aeronautics and motor vehicle design. As a result of this, methods of analysing fluid dynamics are constantly being developed and as such there are various methods of prediction such as theoretical calculations using classical mathematics (which tends to be limited to very simple calculations) and numerical solutions. The use of experimental measurement techniques can also be employed such as the use of Planar Laser Induced Fluorescence (PLIF) [1, 2], Particle Image Velocimetry (PIV) [3-5] and Laser Doppler Velociemetry (LDV) [6, 7]. PIV was employed by Cara et al. to analyse the velocity field generated by a Rushton impeller and compared with simulation results obtained by carrying out a detached eddy simulation (DES) [8]. PIV works by instantaneously getting 2D velocity fields [9]. This is especially useful when it comes to analysing mixing time as a factor of mixing tank design. Mixing time can be seen as the duration of time required to a given level of homogeneity of a given tracer in a particular operation vessel [10]. The mixing time in a stirred vessel was also investigated by Ascanio et al. via colorimetry. The objective was to determine the efficacy of periodic stirring when compared to steady stirring. This came down to analysing the mixing time of a solution of aqueous CMC (carboxymethyl cellulose) and xanthan gum with the aid of calorimetry. They arrived at the conclusion that the periodic mixing configuration proposed was a viable alternative to steady mixing[11]. Colorimetry can be described as the quantitative measurement of colour [12].

A fairly new experimental technique known as electrical resistance tomography (ERT) can also be employed in experimental analysis when it comes to mixing patterns and involves the use of electrodes to measure electrical conductivity in a stirred vessel. This method is at times preferable

due to its non-intrusive nature in that it is a sealed system and does not require the introduction of any tracer. One draw-back is that it is only applicable when dealing with fluids which have differing electrical conductivity values [13].

Other examples of non-invasive techniques include radioactive particle tracking (RPT) and positron emission particle tracking (PEPT) [14].

X-ray techniques can also be employed to analyse mixing patterns. This involves the introduction of a heavy tracer for instance Lead or Barium to a vessel with an agitator [15].

Another common technique for mixing tank analysis is via pH analysis. This was done by Bonvillani et al. [16], who used pH analysis to determine the efficiency of a biochemical reactor to determine its suitability for scaling up. The efficiency measurement to be considered was mixing time and was done by measuring the periodic pH changes taking place within the bioreactor.

One can also use computational methods to analyse various aspects of fluid dynamics. For instance, Duan et al. used computational fluid dynamics to model the turbulence in a semi-batch stirred tank reactor [17]. Computational modelling shall be the main consideration for this thesis. Using computational analysis, it's possible to predict the distribution of various aspects of fluids such as velocity, pressure, temperature, and concentration within a given calculation domain under specific operating conditions.

2.1.1 Advantages of Using Computational Methods

Computational analysis of aspects of fluid flow has some very distinct advantages over its counterparts. For one, using a fluid dynamic software such as Ansys Fluent and Ansys CFX is far less expensive than the corresponding experimental method which would normally involve scaling down the desired object for example a mixing tank and physically varying its particular internals such as impeller diameter or baffle length which can prove to be an expensive endeavour. As more and more analyses are carried out, the cost would only increase. Using a computational technique is also much quicker and therefore many design cases can be handled in one go cutting down on time and manpower. Another advantage is that it provides you with very detailed results aiding in understanding very particular aspects of the fluid in question and its interactions. Using computational analysis also enables the simulation of very realistic conditions as it is not limited to only small sized cases as is the case in the experimental method, can also deal with high temperature scenarios which may be beyond physical experiments and can also handle toxic substances and fast transients. It can also simulate ideal conditions such as operating in two dimensions and having constant density.

While there are no disadvantages in most situations, there are some disadvantages to be attributed to using CFD analysis tools. One is that the implications of a mathematical model may not correspond to what is observed in real life conditions. This might be due to inherent model-form uncertainties. Model form uncertainties are natural variances within the model itself that might lead to the model making incorrect predictions[18]. Simulation might also present issues when handling problems for which an adequate mathematical description has been worked out. This is most apparent when attempting to analyse complex highly turbulent flows. For especially difficult problems, the numerical solution might experience instability and divergence within the simulation process. Another disadvantage of using CFD tools is that it might simply be less expensive to perform an experimental analysis.

2.1.2 Stirred Tank Reactor

Stirred tank reactors are very often used in industry especially when dealing with fluid mixing processes. The importance of stirred tank reactors cannot be understated. According to Bartels et al. [19], half the annual output of the American chemical industry at a certain point of production passed through a stirred tank reactor [19]. A basic stirred tank reactor consists of a tank and impeller and other internals if necessary, such as spargers and baffles. Stirred tanks have a wide variety of uses ranging from liquid-liquid extraction to leaching and crystallisation operations and heterogenous catalysis and as such understanding their operations is crucial [20, 21]. Stirred tank reactors also fulfil a great number of needs in large scale production such as mixing miscible liquids to form a homogenous mixture, dispersing gases and immiscible liquids within another liquid to form an emulsion. Understanding the droplet size within emulsions is of interest to a variety of field for instance the chemical process industry, emergency planning and the pharmaceutical industry (a good example of a common emulsion is Scott's emulsion which is cod liver oil in a liquid suspension) [22]. Vibro-mixing, a relatively new mixing system, can also be used instead of the more common stirred tank system and employ vibromixers which are essentially perforated flat disks which vibrates to promote liquid-liquid homogenization [23]. A power consumption analysis for a vibromixer was carried out by Masiuk [24].

Mixing tanks are also useful in suspension of solid particles in liquids and promoting heat and mass transfer and chemical reactions [20]. For instance, mixing tanks can be used to homogenize slurries [25, 26] which are solid-liquid suspensions. Analysis of this was carried out by Carletti et al. who examined the dynamics of mixing in a fully baffled slurry stirred tank reactor via means of electrical resistance tomography as an investigation tool to observe the fluid fields generated [27] Agitators are also widely used in fermentation procedures, treatment of effluent and various other biochemical

processes. These are often referred to as digesters and can be anaerobic or aerobic and can be either operated in batch or as a continuous stirred tank reactor. Digesters however have a high capital cost (enzymes or bacteria are expensive materials) and maintenance is relatively expensive [28]. The agitation process is also widely employed in petroleum production especially in the oil hydrogenation stage [29]. The use of mixing tanks in such a wide variety of industrial processes further highlights the importance and applicability of this project.

2.2 General Structure of Stirred Tank Reactors

As stated, a stirred tank reactor generally comprises of an agitator and a tank/container. If needed, an assortment of internals can be employed such as baffles and spargers to further enhance the mixing process.

2.2.1 Baffles

Baffles are widely employed in mixing tanks. The absence of baffles promotes a more circular movement of fluids. This therefore leads to poor axial mixing. Unbaffled mixing tanks tend to therefore be considered in industry to be poor mixers in comparison to their baffled counterparts and are seldom in use [30]. Due to the free surface present, vortex formation is promoted which further hinders mixing. The depth of the vortex is highly dependent upon the impeller rotation speed employed but generally the higher the rotation speed, the larger the vortex. This is where baffles come in as they operate by breaking up velocity patterns and hindering the formation of vortices and in many cases promoting mixing. According to Chara et al. [8], the size of the vortex can be given by a non-dimensional unit, ξ, calculated as,

$$\xi = \omega \frac{T}{U_{Tip}} \tag{2.1}$$

where ω is the dimensional vorticity, T is the diameter of the mixing tank and U_{Tip} is the velocity at the tip of the impeller in ms^{-1}. The act of reducing the size of vortices aids in cost saving due to more efficient mixing and higher quality results.

Different baffles can be employed for a variety of situations such as helical baffles and vertical wall baffles.

The action of breaking up velocity fields also aids convection thereby promoting heat transfer. As such heat exchangers on occasion employ baffles. For example shell tube heat exhangers can have different baffle configurations [31]. In fact, baffles have been shown to increase heat transfer and

increase the drop in pressure. An analysis of pressure variation and heat transfer was carried out by Ambekar et al. [32]. The effect of baffles on heat transfer in heat exchangers was also investigated by Dong et al. [33] whereby the effect of different helical baffle schemes on heat transfer was examined and compared. More work was carried out on this whereby a shell-and-tube heat exchanger with folded baffles and low resistance circumferential overlap trisection helical baffle was analysed to observe its efficiency by Dong et al. [34]. Shell-and-tube heat exchangers are very widely used when it comes to the petrochemical industry in petroleum refinery. Duan et al. [35] also did similar work on the effect of a non-continuous helical baffle configuration with varying helix angles. Baffles can also be employed to prevent/suppress sloshing as well as self-pressurisation in 2-phase fluids such as a liquid hydrogen and oxygen mixture in a cryogenic tank. This was investigated by Zuo et al. [36] . Baffles are also employed in exhaust mufflers. In this they function as a means of improving transmission loss [37].

The use of baffles can also be employed to promote biochemical reactions for instance to promote microalgae production within a given raceway pond. Baffles are normally situated at the bottom of the pond. An investigation of the vortex flow field generated in a baffled raceway pond with conical baffles was carried out by Cheng et al. who found them to decrease mixing time while also increasing the mass transfer coefficient and promoting the production of *spirulina* (microalgae) [38]. It is however not always advisable to introduce baffles to an ecological system as it can lead to irreversible and drastic changes. This was shown to be the case by Bylak et al.,[39] who studied the effect of the application of a baffled chute in Poland's Lebunka stream which turned out to be a bad example of human intervention and lead to great changes in the biological community in the area.

However un-baffled tanks also have a place in industry. The main attraction of unbaffled vessels is that they generate very a strong swirling motion by the liquid. This and the centrifugal forces leads to the generation of vortices [40]. High viscosity fluids however operate well in un-baffled tanks. This prevents the formation of dead-zones that would otherwise form in the area surrounding the baffles leading to poor mixing quality. The high viscous nature also inhibits the formation of vortices due to the lower fluid velocity as well as friction with the tank wall thus negating the need for baffles. Crystallisation reactions also very much prefer an un-baffled system as it prevents the premature crystallisation along the baffle walls [20].

2.2.2 Impellers/Agitators

Agitators, as the name implies, are necessary in generating a velocity field in a mixing tank by creating a velocity gradient between the portion of the fluid nearest to the agitator and the section of the fluid furthest from it. Impellers create a pair of vortices above and below the impeller blades. The fluid that surrounds the eddy ends up getting very finely sheared resulting in the reduction of a

property for example concentration. The swirling contributes to a recirculating turbulent flow which enables mixing. Stationary baffles can interact with the flow generated to further enhance the mixing quality [41]. Having more than one impeller in any given system would increase how complex the turbulent flow is.

The most crucial part of any given impeller is the part right behind each individual blade as this is where the two vertical structures are created (above and below the impeller blades) and act as pumps to push the fluid away from the centre and towards the tank wall [8].

There are various impeller types and each of them serves a specific purpose. Angled/axial and bladed agitators are useful in promoting axial flow especially for low viscosity fluids. Its diameter tends to be about a third that of the mixing tank. Aubin et al. [42] investigated the effect of differently configured axial impellers in a single phase mixing tank on the flow pattern being generated using experimental method via means of LDV (Laser Doppler velocimetry). There are also pendulum agitators. These are fairly rare and are normally employed in cheese production in the food processing sector [43]. Another agitator type is turbine sometimes known as paddle agitators which are used when radial flow is preferred for example to fragment fluids in bubbles or drops. Wide radius agitators such as large, inclined paddles or simple anchor agitators are useful to produce peripheral tangential flow to mix viscous products nearer to the tank wall. Archimedes screw agitators such as simple screw agitators and simple helical ribbon agitators are also useful in mixing high viscosity fluids and provide a counter-current flow. Helical ribbon agitators can also be used. They are similar due to their high capacity for homogenization and are widely used in industry especially when dealing with viscous fluids as shown by Dieulot et al. [44] who investigated the mixing of a glucose solution in a laminar regime. This was observed through the conductivity of the tracer introduced to the solution. Another example of an impeller is the grid disk impeller [45, 46] which as the name suggests consists of a disc with grids. Another common impeller type is the Rushton impeller [47, 48] which consists of a disc with six perpendicular paddles that are equidistant to one another. There are even cup-shaped Rushton impellers [49].

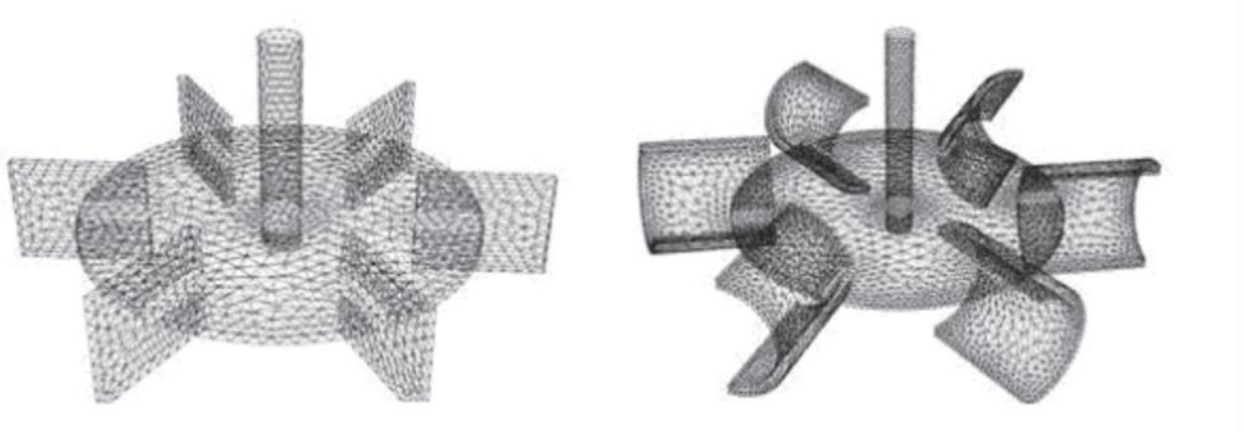

Figure 2-1 Examples of Rushton impellers[50]

It's not uncommon to find more than one impeller in a mixing tank configuration in industry [51]. An experimental study of a dual-rushton turbine impeller mixing tank was carried out by Jaworski et al. [52] to determine local axial and radial mean velocities that arise via means of conductivity probes and further comparison was undertaken with CFD modelling results. This revealed four distinct axial-radial circulation loops (two for each impeller) with the CFD code exhibiting a very high over prediction of the mixing time likely a result of model form uncertainties.

As for positioning, Impellers are not always located at the top and centre of a mixing tank. In industry, it is at times more preferable to use side-entering impellers [53]. This is very common in the petrochemical industry in the blending process to obtain different grades of oil in cylindrical storage tanks.

It should be noted that while stirring is often steady, it can also be more productive and cost effective to employ unsteady stirring whereby the agitation speed is varied at regular intervals. Dieulot et al. observed that this variance saved as much as 60% energy consumption in their experimental runs while maintaining the same mixing time [44].

2.3 Some Commonly Used Equations in Mixing Tank Analysis

2.3.1 Power Number

The power consumption of a mixing tank is a fundamental consideration when it comes to mixing tanks [54, 55] . It is useful to compare various configurations of mixing tanks to determine which is most suitable prior to actual construction. To do this a dimensionless number is employed referred to as the power number.. It’s calculated as follows:

$$N_p = \frac{P}{n^3 D^5 \rho}$$

(2.2)

where P is the power consumed in watts, n is the rotational speed of the agitator in revs s^{-1}, D is the diameter of the impeller in m and ρ is the density of the fluid in kg m^{-3} [20]. By comparing the power number of differing impeller diameter configuration, we can compare the power draw of two different mixing tanks and by extension decide which is most efficient for any given purpose.

2.3.2 Torque

Torque is also a very useful measure of comparing performances of any two given mixing tanks. Torque is the product of the lever arm vector and the applied force vector. Torque is useful as it is directly proportional to power draw and is calculated as such:

$$P = 2\pi n \tau$$

(2.3)

where τ is the torque in N m [50]. Thus, the power number can be calculated as:

$$N_p = \frac{2\pi\tau}{\rho n^2 D^5}$$

(2.4)

2.3.3 Reynolds Number

Reynolds number can be used to determine the level of turbulence being induced in any given mixing system via the impeller to determine whether the flow is laminar, transient, or turbulent. This is given by equation(*2.5*):

$$Re = \frac{nD^2\rho}{\mu}$$

(2.5)

where μ is the dynamic viscosity of the fluid in Pa s.

2.3.4 Pumping Capacity

Another useful aspect in comparing two or more mixing tank geometries is the pumping capacity. In order to achieve this, it is necessary to obtain the radial pumping flowrate of the impeller. According to Zadghaffari et al., [41] the radial pumping flowrate, Q_r, is defined as the volumetric flowrate exiting the turbine blades along a given radial position, r, from the centre of the mixing tank. As such it can be expressed as:

$$Q_r = 2\pi r \int_{z_1}^{z_2} \overline{U_r} dz$$

(2.6)

where z is the coordinate vector in the z direction in m and $\overline{U_r}$ is the average velocity component in the radial direction. $\overline{U_r}$ is assumed to be directly proportional to the tip speed of the blades, that is, $\overline{U_r} \propto \pi n D$ and the integration is carried out over the height of the blade.

$$Q_p = N_q n D^3$$

(2.7)

where N_q is the pumping number and Q_p is the pumping capacity in $m^3 s^{-1}$ and D is the diameter of the impeller [41].

2.4 Discretisation

In CFD, there are two distinct types of discretisation. These are the discretisation of space and the discretisation of equations.

2.4.1 Discretisation of equations

Discretisation is required when moving from a physical mathematical problem to a discrete algorithm due to the inherent difficulty of solving differential equations using analytical methods. This is necessary due to the inability of computers to directly solve differential or partial differential equations (PDE). This is because differential equations have infinite dimensionality and as such representing these differential equations (for instance the various conservation and transport equations), as a finite set of algebraic equations means that they become solvable by computational methods.

Consider the differential equation:

$$\frac{du}{dt} = -\Omega v$$

(2.8)

This can be discretised using the explicit euler formulation resulting in:

$$\frac{v^{v+1} - v^v}{\Delta t} = -\Omega v^v$$

(2.9)

This is the approximation of the first time derivative where v^v is the value of the variable v at the current timestep and v^{v+1} is the value at the next timestep. What this represents is the movement from the infinite dimension described in equation (2.8) to a finite dimension as defined in equation (2.9).

At this point, this algebraic expression can then be put through a numerical scheme. A numerical scheme can be defined as an algorithmic description which when used in the right manner, produces a solution to a given mathematical problem[56]. A numerical scheme that is consistent and stable is guaranteed to converge (solution to the finite difference approximation approaches the true solution of the PDE). The consistency of the numerical scheme means that if one were to go down towards zero with the timestep size or mesh size, the set of algebraic equations should continue to approximate the deferential equation. A numerical scheme is stated to be stable if as the computation proceeds from iteration to iteration or timestep to timestep the errors decay.

2.4.2 Spatial discretisation

As the title suggests, this is the discretisation of the domain over which the user wants to solve a given differential problem or PDE. To represent this, consider a one-dimensional line existing in the x axis:

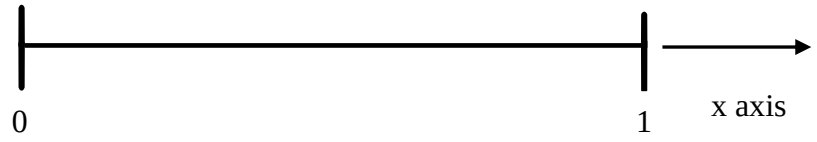

Figure 2-2 Line in the x axis

If the user is interested in the x axis from $(x = 0)$ to $(x = 1)$, spatial discretisation dictates that one needs to subdivide this target area (which contains an infinite number of locations/points) into a set and finite number of computational intervals.

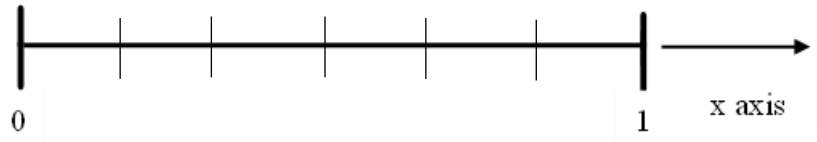

Figure 2-3 one dimensional structured mesh

The region between each interval is referred to as an element or sometimes a volume. The connection points are called nodes. Square elements in 2D are referred to as quadrilaterals while 3 sided elements are called triangles. 3D triangles are referred to as tetrahedra. This thesis employs a tetrahedral mesh for computation.

In 3D there are 4 standard types of elements:

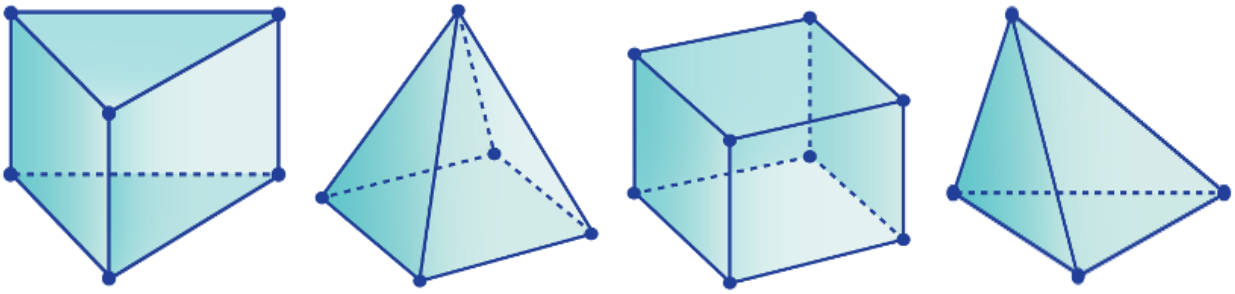

Prismatic cell Pyramid Hexahedron tetrahedron

Figure 2-4 mesh element types

3 Computational Fluid Dynamics

Computational Fluid dynamics (CFD) [57-59] is a modelling system used to analyse fluid changes because of external stimuli. These fluid changes include heat transfer, velocity flux, pressure changes etc. Temperature distribution can also be analysed via CFD for instance in the polymerization of propylene in a fluidized bed reactor [60]. When it comes to its biological application, CFD can be used to model blood flow patterns as carried out by Khalafvand et al. who employed Arbitrary Langrangian-Eulerian formulation of the Navier-Stokes equation[61]. CFD was also employed by Mohizin et al., as an analysis tool for an air-powered needle-free injection system [62].

CFD can also be employed to model the residence in a continuous stirred tank reactor and therefore determine how much time is spent in the reactor by the reagents [63]. This examination of residence time distribution (RTD) can also be performed for tubular stirred tank reactors [64]. CFD also has applications in the food processing industry for instance modelling the food drying process that is the dehydration of food for storage purposes [65].

3.1 Conservation Equations

To fully understand the operating criteria of CFD, it is necessary to first cover the nature of fluids. Fluids are substances that can be seen to deform and change continuously and permanently when acted upon by forces that vary spatially in either magnitude or direction. Mechanics on the other hand is concerned with external effects such as forces and heat effect on a given physical object. Therefore, the study of fluid mechanics is the observation of how these external forces affect fluids. The same is true for solid mechanics. Both fields have mathematical equations describing physical laws being encompassed. These are referred to as field equations [66]. These field equations are based on the laws of conservation of energy, momentum, and mass.

In order to investigate fluid mechanics, the continuum hypothesis is employed. This states that we may treat any fluid property as varying continuously from one point to the next within a fluid and as such we can associate any volume of fluid regardless of size (must not be zero), the same macroscopic properties such as temperature and velocity, that are associated to the bulk fluid. This creates a unified system known as continuum mechanics for the study of both fluid and solid mechanics [66].

In the case of fluid mechanics, the field equations are normally referred to as transport equations and the general transport equation will adopt the form:

$$\underbrace{\frac{\partial(\rho\phi)}{\partial t}}_{Transient} + \underbrace{\frac{\partial(\rho u\phi)}{\partial x}}_{Convection} = \underbrace{\frac{\partial}{\partial x}\left(\Gamma\frac{\partial\phi}{\partial x}\right)}_{Diffusion} \underbrace{+S}_{Source/sink}$$

(3.1)

In Eq. (3.1), u is the velocity in m s^{-1}, x represents the spatial variable in m of the fluid and φ is the dependent variable. φ can constitute of velocity, enthalpy, temperature, mass fraction, a turbulence quantity and more. As such, each component of φ brings with it a specific value of Γ, S and boundary conditions. The source term S is primarily related to heat generation in a given solid, the generation or deconstruction of a given chemical species in a chemical reaction, body forces in a given fluid and anything else that does not fit into the transient, convection and diffusion terms adequately. Γ also known as the diffusion coefficient generally relates to fluid aspects such as conductivity and viscosity.

Therefore, for conservation of mass:

$$\underbrace{\frac{\partial\rho}{\partial t}}_{Transient} + \underbrace{\frac{\partial(\rho u)}{\partial x}}_{Convection} = 0$$

(3.2)

The same principle of $transient + convection = diffusion + source$ can be employed when defining conservation of momentum. This gives the following equation.

$$\underbrace{\frac{\partial(\rho u)}{\partial t}}_{Transient} + \underbrace{\frac{\partial(\rho uu)}{\partial x}}_{Convection} = \underbrace{\frac{\partial}{\partial x}\left(\mu\frac{\partial u}{\partial x}\right)}_{Diffusion} \underbrace{-\frac{\partial P}{\partial x} + S_u}_{Source/sink}$$

(3.3)

For the conservation of energy:

$$\underbrace{\frac{\partial(\rho C_p T)}{\partial t}}_{Transient} + \underbrace{\frac{\partial(\rho C_p u T)}{\partial x}}_{Convection} = \underbrace{\frac{\partial}{\partial x}\left(k\frac{\partial T}{\partial x}\right)}_{Diffusion} \underbrace{+S_T}_{Source/Sink}$$

(3.4)

3.2 Turbulence Modelling

According to Fisher et al., turbulence can be defined as the complex motion of a fluid occurring at high enough flowrates in a variety of systems and as such has very broadly extending technological implications [67]. Due to the impact that turbulence can have on design it is of great value to model it and define it at specific locations at a particular time when dealing with moving fluids. When trying to understand turbulent flows, the most widely used reference is turbulence eddies which can best be described simply as localized swirling fluid motion. In nature, turbulence has the following properties: it is irregular and heavily randomized, it is known to diffuse through a system, dissipates and disperses without a constant flow of energy from an external source and only occurs when the system is operating with a large Reynolds number (as low Re is indicative of a laminar flow pattern). Turbulent flow consists of different structures all bearing different length scales and velocity fluctuations.

When discussing turbulence modelling, one must first discuss the Navier-Stokes equation. This equation is the basis of describing viscous fluid flow and it is therefore vital that we devise an accurate, stable and efficient method of finding the numerical solutions of these equations [68]. The Navier-Stokes equation takes the form:

$$\overbrace{\overbrace{\rho}^{mass}\overbrace{\left(\frac{\partial u}{\partial t} + \nabla . uu\right)}^{acceleration}}^{} = \overbrace{-\nabla P + \mu\nabla^2 u}^{Force}$$

(3.5)

where μ is viscosity in Pa.S and ∇P is the pressure gradient. This is the fluid equivalent of Newton's second law of motion where the force exerted by an object is given by the product of the object mass and its acceleration.

It should be noted that this is only applicable when dealing with incompressible Newtonian fluids. The fluid must also be viscous. Euler's equations on the other hand, are used for ideal fluids.

The most common representation of this equation involves dividing both sides by the density value providing us with:

$$\frac{\partial u}{\partial t} + \nabla \cdot uu = -\frac{1}{\rho}\nabla P + \frac{\mu}{\rho}\nabla^2 u$$

(3.6)

Finding ways to solve this equation is the entire basis of turbulence modelling.

However turbulent flows can be challenging things to deal with due to their nature in that they are unsteady and have a strong dependence on initial conditions as well as having a wide range of eddies thus it is necessary to employ various techniques to account for this. There are three commonly referenced techniques:

i) Large Eddy Simulations (LES)

ii) Reynolds Averaged Navier-Stokes (RANS)

iii) Direct Numerical Simulation (DNS)

The employment of direct numerical simulation involves the resolution of every time scale and length. This means that a complete three dimensional and time-dependent solution of the Navier-Stokes equations must be obtained for an instantaneous fluid velocity as a function of both time and velocity [69]. In this case the Navier-Stokes equations are solved without the need of any turbulence model and is given by:

$$\overbrace{\frac{\partial u}{\partial t}}^{\substack{Transient\\ Term}} + \overbrace{\nabla \cdot uu}^{\substack{Convective\\ Term}} = -\frac{1}{\rho}\overbrace{\nabla P}^{\substack{Pressure\\ Term}} + \overbrace{\frac{\mu}{\rho}\nabla^2 u}^{\substack{Diffusion\\ Term}} + \overbrace{\rho g}^{\substack{Body\\ Force}}$$

(3.7)

Although using this would be desirable it lacks any practical applications for a huge array of fluid flow situations due to it being only possible for low Reynolds number flows and very simple geometries and also the complex nature of transport equations in and of themselves [69]. It should also be noted that the time and space details acquired using DNS are not generally required for design purposes which is another downside of employing it as a means of resolving turbulence.

3.2.1 Large Eddy Simulation (LES)

Large eddy simulation operates under the premise of resolving large scales of turbulent eddies and modelling small scales of turbulence. It is one of the most popular means for resolving numerical simulations for turbulent systems. It is an unsteady and three-dimensional computation and as such needs supercomputing resources to solve. This is because a significant amount of computing resources is necessary in accurately capturing the length-scales that propagate the energy [70]. The

motivation of resolving in such a manner is that large scales are problem dependent and as such come with inherent modelling difficulties. Small scales however, tend to get more universal and isotropic/uniform and are therefore more easily modelled due to their general lack of complexity. LES is based on filtering the Navier-Stokes equations over a finite grid volume. This will resolve it in such a manner that portions of turbulence larger than the desired filter width can be resolved separately and those smaller ones can then be separately modelled normally through employing the simple eddy viscosity model [71].

The use of LES to model turbulence flow has its origins in meteorology and is based on the premise that large-scale motion can vary greatly between two or more turbulent flows whereas small-scale turbulence is much more predictable and universal[72]. The need for vast amounts of computing power can be a major hindrance in that, for complex enough flow patterns, it may be necessary to employ supercomputer clusters which can prove to be extremely expensive. Work was carried out by Udin, Neumann and Weigand [73] on Large Eddy Simulation analysis of an impinging jet using a dynamic Smagorinsky model with the objective of mapping heat transfer and flow characteristics of an orthogonally impinging cold jet on a heated plate. This required the employment of two supercomputer clusters in Stuttgart, Germany. It also has a long computational time factor. It is also largely confined to small domains. These are viewed as major impediments to the viability of using LES as a turbulence simulation system in industry. Despite all these it can still be implemented for stirred tank analysis. This was carried out by Min et al. who found a greater agreement of results found via experimental method with LES than conventional RANS [74].The LES system can be said to be a bridging the gap between Reynolds Averaged Navier-Stokes system and Direct Numerical Simulation. .

3.2.2 Reynolds Averaged Navier-Stokes (RANS)

When employing Reynolds Averaged Navier-Stokes turbulent analysis models the average motion is the only quantity that is computed. That is to say, the effect of fluctuations is what is modelled. It therefore can be said to model all scales of eddies as opposed to LES which focuses on resolving large scale eddies while modelling small scale eddies [75].

When solving for mean motion as required in the case of the Reynolds Averaged Navier-Stokes equation, the equations are derived by averaging the actual Navier-Stokes equations. The velocities as well as other quantities such as pressure are then decomposed into separate average and fluctuating parts. This decomposition takes the general form of:

$$a = A + a' \tag{3.8}$$

This holds for spatial averaging (spatial averages are most common in climate science and are estimations obtained by averaging over point observations [76]), ensemble averaging and temporal averaging. That is to say, that any steady RANS equation will accurately display the distribution in space of any quantity that is averaged over a given period of time, in this instance, pressure and velocity. In fact, any proper RANS simulation must be time dependent in an effort to properly apply the RANS methodology. This however substantially increases the computational cost that comes with it [77]. Considering the Navier-Stokes equation in Eq. (3.8) above, introducing decomposition terms for both pressure and velocity and converting them into mean and fluctuating parts:

$$p = P + p' \tag{3.9}$$

where P is the mean pressure and p' is the pressure fluctuation and,

$$u = U + u' \tag{3.10}$$

where U is the mean velocity and u' is the velocity fluctuation over a given period of time.

This averaging alters the Navier-Stokes equation into:

$$\frac{\partial U}{\partial t} + \nabla \cdot UU = -\frac{1}{\rho}\nabla P + \frac{\mu}{\rho}\nabla^2 U + \nabla \cdot \langle u'u' \rangle \tag{3.11}$$

where $\langle u'u' \rangle$ is referred to as the Reynold's stress tensor.

$$\langle u'u' \rangle = \begin{bmatrix} u'u' & u'v' & u'w' \\ u'v' & v'v' & v'w' \\ u'w' & v'w' & w'w' \end{bmatrix} \tag{3.12}$$

RANS equations have a multitude of applications ranging from subsonic mixing tank fluid dynamic analysis to supersonic ejector refrigeration analysis [78]. Due to these Reynolds stresses, RANS equations, as widely used in engineering design as they are, are known for their unreliability in many flow patterns that are somewhat relevant in engineering. This is due to the fact that they introduce model-form uncertainties [79].This however can be somewhat overcome via means of data driven methods. This is of significant interest to the community of computational fluid dynamics as it promotes the efficiency of RANS by quantifying the uncertainty. This is done by use of machine-

learning algorithms to increase the accuracy of prediction [80]. A source of this model form uncertainty is that RANS simulations tend to under-predict the level of kinetic energy [81].

The relationship between Reynolds stresses and mean velocity was first postulated by Joseph Valentin Boussinesq [82]. Boussinesq is widely regarded as the first person to propose the phenomenon of eddy viscosities which is a major field of study in turbulence modelling. He has made some major contributions to science and in fact scientists are constantly rediscovering his results such as Reyleigh rediscovering the equation for solitary waves in 1876. Boussinesq also pioneered viscous boundary layers and his works are therefore of great importance to the field of turbulence modelling [82]. The relationship between Reynolds stresses and mean velocity is referred to as the Boussinesq hypothesis. This essentially states that the Reynolds stresses have a linear relationship with mean strains via the turbulent and eddy viscosity. This relationship can be expressed as;

$$\nabla.\langle u'u'\rangle_{ij} = \frac{\partial}{\partial x_j}\left(\mu_t\left(\frac{\partial \bar{u}_i}{\partial x_j}+\frac{\partial \bar{u}_j}{\partial x_i}\right)\right) \tag{3.13}$$

where μ_t represents the eddy viscosity gradient in m^2/s.

Therefore, the Reynolds averaged Navier-Stokes equations are;

$$U\frac{\partial U}{\partial x}+V\frac{\partial U}{\partial y}+W\frac{\partial U}{\partial z} = -\frac{1}{\rho}\frac{\partial P}{\partial x}+\frac{\mu}{\rho}\left[\frac{\partial^2 U}{\partial x^2}+\frac{\partial^2 U}{\partial y^2}+\frac{\partial^2 U}{\partial z^2}\right]-\left[\frac{\partial \overline{u'^2}}{\partial x}+\frac{\partial \overline{u'v'}}{\partial y}+\frac{\partial \overline{u'w'}}{\partial z}\right] \tag{3.14}$$

$$U\frac{\partial V}{\partial x}+V\frac{\partial V}{\partial y}+W\frac{\partial V}{\partial z} = -\frac{1}{\rho}\frac{\partial P}{\partial x}+\frac{\mu}{\rho}\left[\frac{\partial^2 V}{\partial x^2}+\frac{\partial^2 V}{\partial y^2}+\frac{\partial^2 V}{\partial z^2}\right]-\left[\frac{\partial \overline{u'^2}}{\partial x}+\frac{\partial \overline{u'v'}}{\partial y}+\frac{\partial \overline{u'w'}}{\partial z}\right] \tag{3.15}$$

$$U\frac{\partial W}{\partial x}+V\frac{\partial W}{\partial y}+W\frac{\partial W}{\partial z} = -\frac{1}{\rho}\frac{\partial P}{\partial x}+\frac{\mu}{\rho}\left[\frac{\partial^2 U}{\partial x^2}+\frac{\partial^2 U}{\partial y^2}+\frac{\partial^2 U}{\partial z^2}\right]-\left[\frac{\partial \overline{u'^2}}{\partial x}+\frac{\partial \overline{u'v'}}{\partial y}+\frac{\partial \overline{u'w'}}{\partial z}\right]\text{-g} \tag{3.16}$$

For the RANS equation, $\left[\frac{\partial \overline{u'^2}}{\partial x}+\frac{\partial \overline{u'v'}}{\partial y}+\frac{\partial \overline{u'w'}}{\partial z}\right]$ is known as the closure problem.

4 Eddy Viscosity Models

Any Reynolds averaged equation developed to resolve the turbulent regime of a given system requires a closure model in order to find the required complete set of differential equations [83]. These are

normally classified according to the number of equations comprising of a given system. There are close to two hundred models in use. Below are examples of some common turbulence model systems.

4.1.1 Zero-equation models

These are sometimes referred to as algebraic models. A common system is the Prandtl mixing length model. As the name suggests, this was proposed by Ludwig Prandtl who is generally regarded as the father of modern aerodynamics due to his contribution in the boundary layer concept [84]. He also developed the Prandtl number which is a dimensionless number that correlates the viscosity of a fluid with its thermal conductivity properties [85]. For the Prandtl mixing length;

$$\mu_t = l_0 \left| \frac{\partial \bar{u}}{\partial y} \right| \tag{4.1}$$

In this l_0 can be the thickness of boundary layers or mixing layers.

Another model is the Smagorinsky model [86, 87]. It is known to overly dissipate flows and this can be a drawback [88]. It is however a very popular large eddy simulation method and has applications in a variety of fields for instance gas flow dynamics [89]. It adopts the form;

$$\mu_t = {l_0}^2 \left(2 \bar{S}_{ij} \bar{S}_{ij}\right) \tag{4.2}$$

where

$$\bar{S}_{ij} = \frac{1}{2}\left(\frac{\partial u_i}{\partial x_j} + \frac{\partial u_j}{\partial x_i}\right) \tag{4.3}$$

4.1.2 One equation models

Examples of one equation models include the Baldwin and Barth model [90, 91] and the Spallart and Allmaras model [92]. The Baldwin and Barth model is a one equation model developed by Barret Baldwin and Timothy Barth as a means of eliminating the need to use an algebraic length scale as stated in their paper titled "A one-equation turbulence transport model for high Reynolds number wall-bounded flows" [93].

Another example is the Prandtl one-equation model. This takes the form;

$$\mu_t = k^{1/2} l_0 \tag{4.4}$$

where

$$k = \frac{1}{2}(\langle u'u' \rangle + \langle v'v' \rangle + \langle w'w' \rangle)$$

(4.5)

4.1.3 Two equation models

Examples include the $k - \varepsilon$ model, $k - L$ model, $k - \omega$ model and the $k - T$ model. The $k - L$ model can be employed to model blood flow in arteries with a no-slip boundary wall condition [94]. In the two equation models listed above k denotes the turbulent kinetic energy. The adjoining terms all serve to represent a different aspect. For instance in the $k - \omega$ two equation model, ω is a representation of the turbulence frequency [95].

The $k - \varepsilon$ equation [96, 97] is a two-equation system whereε denotes the dissipation rate of turbulent energy within the system. Variants of the standard $k - \varepsilon$ two equation model include $RNG\ k - \varepsilon$ and realizable $k - \varepsilon$. Other variants of the $k - \varepsilon$ model include the Chen-Kim $k - \varepsilon$ and the optimised Chen-Kim $k - \varepsilon$ [98-100].

Two equation models do have inherent disadvantages. They have a problem with being stiff in certain regions requiring a minimization of the employed time-step. Another means of overcoming this is by means of employing an implicit scheme in any given computational fluid dynamics program. Another issue is with the kinetic energy dissipation. It goes to zero at/nearest to the walls and therefore cannot be resolved by the grid and it's therefore necessary to employ a separate wall function to go along with the simulation. Work on error analysis as it pertains to the use of RANS equations was done by Coroneo et al.to determine the limits of RANS by carefully verifying the numerical uncertainties that come with it and comparing the overall results obtained by modelling a single phase stirred tank and the experimental data readily available in literature [101].

Zero, one and two equation models are not the only equation models employed in fluid dynamic analysis. There are three equation models such as the $k - \varepsilon - A$ model and also four equation models such as the $V^2 - f$ [102] which is a variation of the standard $k - \varepsilon$is anisotropic in nature of the turbulence nearest to the wall that is absent in the other Reynolds averaged Navier-Stokes equations [103].

5 Eddy Viscosity Models for RANS

RANS calculations are the primary means for performing computational fluid dynamics (CFD) simulations in fluid flow analysis tools used in industry due to it being more affordable than

employing direct numerical simulations or large eddy simulations [104]. Understanding eddy viscosity models and how they are used to solve the RANS equation is therefore useful.

The Reynolds-averaged Navier-Stokes equations in tensor notation are:

$$\frac{\partial}{\partial t}\rho U_i + \frac{\partial}{\partial x_j}\left(\rho U_i U_j\right) = -\frac{\partial}{\partial x_i}P + \frac{\partial}{\partial x_j}\left[\mu\left(\frac{\partial}{\partial x_j}U_i + \frac{\partial}{\partial x_i}U_j\right) - \overline{\rho \acute{u}_i \acute{u}_j}\right] \tag{5.1}$$

The Reynolds averaging process produces what is referred to as the Reynolds stress tensor:

$$-\overline{\rho \acute{u}_i \acute{u}_j} \tag{5.2}$$

That is to say that the Reynolds averaging process is done to decompose the Navier Stokes equation into the time averaged component and the fluctuating velocity component (Reynolds stress tensor). The importance of the Reynolds stress term in Eq. (*5.2*) above is that we do not solve any equations for the fluctuating velocity components represented by u. This results in us being unable to solve for the full Navier Stokes equation for the mean velocity U. This issue is referred to as the turbulence closure problem.

Solving for the Reynolds stress tensor would enable us to have all the variables required to solve for the momentum equations and as a result calculate the mean velocity field of the fluid. Coming up with a method to solve the Reynolds stress term is therefore crucial to CFD modelling using RANS. Eddy viscosity models are a class of models that we use to calculate the Reynolds stress term. It should be noted that not all turbulence models are eddy viscosity models, however all eddy viscosity models are classified as turbulence models.

Table 5-1 Table of turbulence models.

Eddy viscosity model	Other models
k-ω SST	Full subgrid scale [105]
k-ε	Reynolds Stress (RSM) [106]
Smagorinsky [107]	
DSM (Dynamic Smagorinsky Model) [108]	

5.1 Derivation of Eddy Viscosity Models

Let us consider a boundary layer flow. As the fluid flows along the surface of the boundary layer in such a manner that as you move away from the boundary wall, the mean velocity (U) increases resulting in a sheared flow profile as displayed in Figure 5-1.

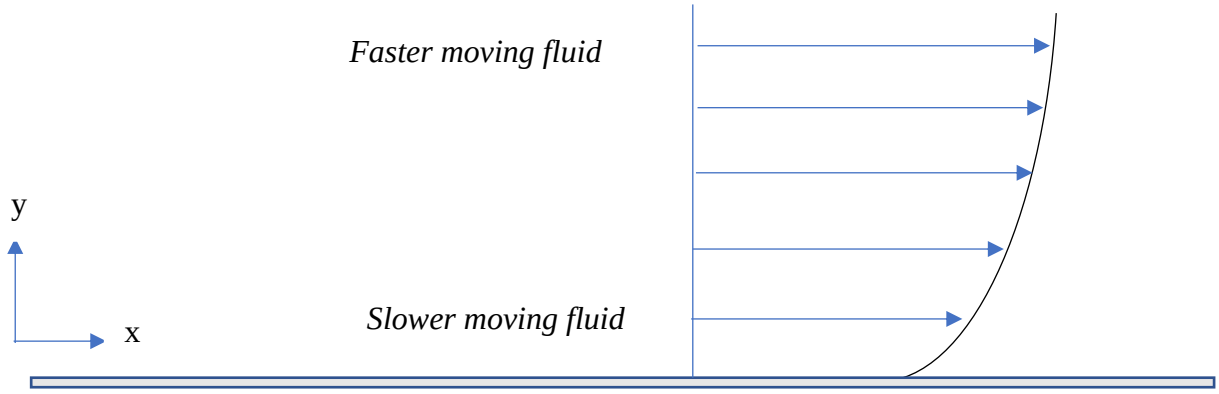

Figure 5-1 Illustration of the shear velocity.

Due to the fluid flow being turbulent in nature, we have turbulent fluctuations overlaying the mean flow. Consider therefore a parcel of the bulk fluid flowing across the boundary wall. This parcel of fluid is sheared by both the mean flow and the turbulence eddies. These two effects are represented by Figure 5-2.

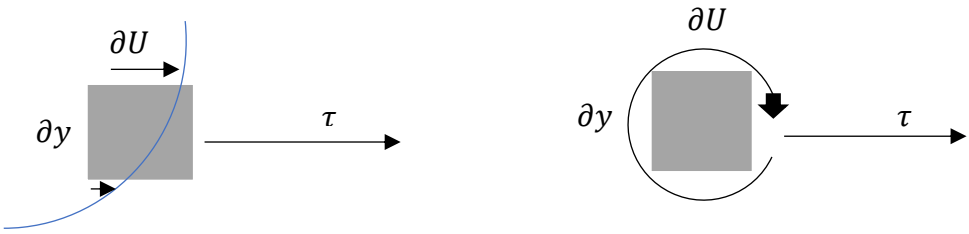

Figure 5-2 Illustration of shearing because of mean flow and turbulence eddies respectively.

Due to the fluid swirling within the element, the flow direction within the fluid is different at the top of the element than at the bottom of the element resulting in shearing of the flow within the element. There is also a faster section of moving fluid at the top of the element than at the bottom of the element resulting in further shearing of the fluid element. These two factors contribute to the shearing of the fluid flow.

We can therefore write equations to represent these two effects:

$$\tau = \mu \frac{\partial U}{\partial y}$$

(5.3)

Equation for the viscous shear (mean flow shear).

$$\tau = \overline{-\rho u' v'}$$

(5.4)

Equation for the shear stress resulting from turbulence.

As seen in Eq. (5.4), the shear stress component is the same as the Reynolds stress for an incompressible flow. As mentioned, we do not solve this directly since there are no transport equations for them. Instead, we must relate the shear stress term to the mean velocity values within the flow field (*U, V, W*).

To do this, we relate the turbulence fluctuations to Brownian motion in gases. As such we assume that the flow and interactions within the fluid are as random as those in gas particle collisions. In Brownian motion, the gas particles are colliding in randomized patterns transferring energy and momentum from one particle to another. It's this random nature of movement that we assign to the turbulence fluctuations. In reality, turbulent flows are not random, instead being made up of eddies/swirls.

If we introduce gas particles to the fluid flowing within boundary layer construct in Figure 5-1 above, we will have a situation where the gas particles further away from the boundary layer were moving at a higher velocity than those nearer to the wall. This leads to the particles lower down being influenced and accelerated by the particles higher up. Thus, there is a transfer of momentum from the particles higher up to those lower down. Meaning that momentum is transferred in the direction of the velocity gradient within a given fluid flow. This is key to conceiving eddy viscosity models. Reynolds stress can be assumed to be directly proportional to the velocity gradient.

$$\overline{-\rho u' v'} = \mu_t \frac{\partial U}{\partial y}$$

(5.5)

where μ_t is the constant of proportionality referred to as the turbulent/eddy viscosity. This is analogous to Newton's law of viscosity sometimes being referred to as the eddy viscosity of Boussinesq or simply the Bousinesq hypothesis [109]. Further modelling is required to solve for the constant μ_t.

Therefore, instead of modelling the Reynolds stress tensor, using turbulence modelling, we shift the emphasis of our modelling to the turbulent viscosity.

For the CFD modelling of a stirred tank reactor, Eq. (*5.5*) above needs to be mapped onto a three-dimensional format.

Swapping the co-ordinate systems around in equation (*5.5*) above, we arrive at the formula:

$$\overline{-\rho v'u'} = \mu_t \frac{\partial V}{\partial x} \tag{5.6}$$

Since $\overline{-\rho v'u'} = \overline{-\rho u'v'}$:

$$\overline{-\rho u'v'} = \mu_t \left(\frac{\partial U}{\partial y} + \frac{\partial V}{\partial x}\right) \tag{5.7}$$

This means that Eq. (5.4) and Eq. (*5.6*) can be written in the form of Eq. (*5.7*). This is particularly useful when it comes to analysing the normal stress components.

Consider $\overline{-\rho u'u'}$:

$$\overline{-\rho u'u'} = 2\mu_t \left(\frac{\partial U}{\partial x}\right) \tag{5.8}$$

Adding up the normal stress component for all dimensions:

$$\overline{-\rho u'u'} + \overline{-\rho v'v'} + \overline{-\rho w'w'} = 2\mu_t \left(\frac{\partial U}{\partial x} + \frac{\partial V}{\partial y} + \frac{\partial W}{\partial z}\right) \tag{5.9}$$

Instantaneous kinetic energy $k(t)$ within a turbulent flow regime in an incompressible fluid is described as the sum of the mean kinetic energy K and the turbulent kinetic energy k. Where:

$$k = \frac{1}{2}\left(\overline{u'^2} + \overline{v'^2} + \overline{+w'^2}\right)$$

$$K = \frac{1}{2}(U^2 + V^2 + W^2)$$

$$k(t) = K + k \tag{5.10}$$

This can be related back to the normal stresses in Eq. (*5.9*) as:

$$-\rho(\overline{u'u'} + \overline{v'v'} + \overline{w'w'}) = -2\rho k$$

(5.11)

However, in our derivations we can see that:

$$2\mu_t\left(\frac{\partial U}{\partial x} + \frac{\partial V}{\partial y} + \frac{\partial W}{\partial z}\right) \neq -2\rho k$$

(5.12)

This error compounds with the fact that for an incompressible flow, the continuity equation dictates that [110]:

$$\frac{\partial U}{\partial x} + \frac{\partial V}{\partial y} + \frac{\partial W}{\partial z} = 0$$

(5.13)

Therefore:

$$\overline{-\rho u'u'} + \overline{-\rho v'v'} + \overline{-\rho w'w'} = 0$$

(5.14)

The sum of the normal stresses should equate to our turbulent kinetic energy as already discussed above and not zero. We therefore have two sources of error. There is an overprediction of $2\mu_t\left(\frac{\partial U}{\partial x} + \frac{\partial V}{\partial y} + \frac{\partial W}{\partial z}\right)$ and an underprediction of the turbulent kinetic energy. When corrected for this, the resulting set of equations are [110]:

$$\overline{-\rho u'u'} = 2\mu_t\left(\frac{\partial U}{\partial x}\right) - \frac{2}{3}\rho k$$

$$\overline{-\rho v'v'} = 2\mu_t\left(\frac{\partial V}{\partial y}\right) - \frac{2}{3}\rho k$$

$$\overline{-\rho w'w'} = 2\mu_t\left(\frac{\partial W}{\partial z}\right) - \frac{2}{3}\rho k$$

(5.15)

The normal stress equations and the shear stress equations are combined within the CFD code i.e., Eq. (*5.5*) and Eq. (*5.8*). This is done by first writing both sets of equations in tensor notation.

$$\overline{-\rho u_i{}' u_j{}'} = \mu_t \left(\frac{\partial U_i}{\partial x_j} + \frac{\partial U_j}{\partial x_i} \right)$$

(5.16)

for the shear stress.

$$\overline{-\rho u_i{}' u_j{}'} = \mu_t \left(\frac{\partial U_i}{\partial x_j} + \frac{\partial U_j}{\partial x_i} - \frac{1}{3} \frac{\partial U_k}{\partial x_k} \right) - \frac{2}{3} \rho k$$

(5.17)

for the normal stress.

Introducing the Kronecker delta therefore results in:

$$\overline{-\rho u_i{}' u_j{}'} = \mu_t \left(\frac{\partial U_i}{\partial x_j} + \frac{\partial U_j}{\partial x_i} - \frac{1}{3} \frac{\partial U_k}{\partial x_k} \delta_{ij} \right) - \frac{2}{3} \rho k \delta_{ij}$$

(5.18)

This is works for both normal and shear stress components. This is the basis for the eddy viscosity hypothesis. The new unknown μ_t(eddy viscosity term) is then solved for using the chosen turbulence model, in this case the realizable $k - \varepsilon$ model.

6 k-ε Model

To solve for μ_t, the equations for k (turbulent kinetic energy) and ε (turbulent energy dissipation) must be solved for and plugged into the equation [111]:

$$\mu_t = \rho C_\mu \frac{k^2}{\varepsilon}$$

(6.1)

Early turbulence models employed the use of mixing length (l_m) to solve for the eddy viscosity. The mixing length is a representative measure of the size of the eddies where a large mixing length indicates a large quantity of turbulence which means that there is a lot of mixing in the RANS equations. This was proposed to be related to the eddy viscosity through the equation:

$$\mu_t = \rho {l_m}^2 \left| \frac{\partial U}{\partial y} \right|$$

(6.2)

In attempting to specify the mixing length, Ludwig Prandtl in 1925 proposed that the size of the eddies from a point away from wall surface is limited by the distance from the wall surface to the

point. In other words, the mixing length is the average distance over which a fluid element transfers momentum [112]. Thus, the maximum size of the eddies (mixing length) is directly proportional to the distance y from the boundary wall.

$$l_m = ky \tag{6.3}$$

where k is a scalar quantity with $k = 0.41$.

Viscosity also acts to limit the size of the eddies at or near the boundary wall. The act of which, distorts and reduces the size of the eddies. This is referred to as damping and leads to the introduction of a damping function. This can be seen in the equation proposed by Van Driest [113] in his modification of the standard Prandtl mixing length model.

$$l_m = ky\left[1 - exp\left(\frac{-y}{A^+}\right)\right] \tag{6.4}$$

where A^+ is a damping length constant and is equivalent to 26.0 [114]. This can further be modified to take into account the effect of surface roughness as shown in the work done by Krogstad et al. [115].

The objective is to solve a transport equation for both the turbulent kinetic energy (k), and the turbulent dissipation rate (ε) which are substituted into Eq. (*6.1*) to solve for the turbulent viscosity and close the RANS equation. The transport equation for the turbulent kinetic energy is given as:

$$\frac{\partial(\rho k)}{\partial t} + \nabla.(\rho U k) = \nabla.\left[\left(\mu + \frac{\mu_t}{\sigma_k}\right)\nabla k\right] + (G_k + G_b + S_k - Y_M - \rho_\varepsilon) \tag{6.5}$$

where G_b is the generation due to buoyancy, G_k is the generation of turbulent kinetic energy due to the mean velocity shear, Y_M represents the contribution of the fluctuating dilation in compressible turbulence to the overall dissipation rate and S_k is representative of any other desired source or sink terms. Of note is the presence of the negative dissipation term, implying that the turbulent dissipation rate acts to reduce the turbulent kinetic energy within the flow. It's important to understand that this equation is identical to all modified versions of the $k - \varepsilon$ model. How these models are differentiated is in the transport equation for the turbulent kinetic energy dissipation rate as discussed below.

$$\frac{\partial(\rho\varepsilon)}{\partial t} + \nabla.(\rho U\varepsilon) = \nabla.\left[\left(\mu + \frac{\mu_t}{\sigma_\varepsilon}\right)\nabla\varepsilon\right] + \left(C_1\frac{\varepsilon}{k}(G_k + C_3G_b) + S_\varepsilon - C_2\rho\frac{\varepsilon^2}{k}\right)$$

(6.6)

The source and sink terms have the model coefficients C_1, C_2 and C_3. These are empirical and are what vary between the standard, realizable and RNG $k-\varepsilon$ models. σ_ε and σ_k are the turbulent Prandtl numbers for ε and k [116]. In the Fluent manual, the $k-\varepsilon$ coefficients are $C_1 = 1.44$, $C_2 = 1.92$, $C_\mu = 0.09$, $\sigma_k = 1$ and $\sigma_\varepsilon = 1.3$. These values were determined experimentally as seen in the work done by Launder and Sharma and have been shown to give more accurate results [117].

For this thesis, the realizable $k-\varepsilon$ model was the chosen model. The term realizable is in reference to the mathematical constraints being applied to the Reynolds stresses and are absent in both the RNG and standard $k-\varepsilon$ models. The realizability is ensured by making C_μ a variable and not a constant and making it sensitive to both the turbulence and mean flow [118, 119]. The transport equation for ε in the realizable $k-\varepsilon$ model is given by:

$$\frac{\partial(\rho\varepsilon)}{\partial t} + \nabla.(\rho U\varepsilon) = \nabla.\left[\left(\mu + \frac{\mu_t}{\sigma_\varepsilon}\right)\nabla\varepsilon\right] + \left(C_1\frac{\varepsilon}{k}(C_3G_b) + S_\varepsilon + \rho C_1S_\varepsilon - C_2\rho\frac{\varepsilon^2}{k+\sqrt{v\varepsilon}}\right)$$

(6.7)

7 Multiple reference frame model

There are three general approaches for simulating fluid flow in an agitator. These are multiple reference frame, sliding mesh approach and computational snapshot [29]. Multiple reference frame and computational snapshot methods are based on steady state modelling while the sliding mesh approach is utilised in transient modelling.

When modelling turbomachinery in any CFD package, mesh motion must be considered. For a vast majority of cases of CFD simulations, the meshes are said to be stationary. Examples include modelling flow along aerofoils and fluid flow along pipe systems. In these cases, we must solve the incompressible steady Navier-Stokes equation. This equation is given below [109].

$$\nabla.(UU) = -\frac{1}{\rho}\nabla P + \nabla.(v\nabla U)$$

(7.1)

In CFD when dealing with turbomachinery, as is the case with the rotary impeller, we can introduce a moving section of mesh at the start of each timestep. We then need to solve the incompressible unsteady Navier-Stokes equations [109].

$$\frac{\partial U}{\partial t} + \nabla.(UU) = -\frac{1}{\rho}\nabla P + \nabla.(\nu \nabla U)$$

(7.2)

This technique is referred to as the sliding mesh interface approach whereby sliding-mesh interfaces are formed between the rotating mesh and the stationary mesh [120]. This method does have some inherent drawbacks. For instance, the unsteady computation requires very small time-steps to account for the revolution of the impeller (a minimum of 360 timesteps to model each revolution) which can be very computationally expensive since we need to model a minimum of 10 revolutions. Secondly, the meshes along the interface region are stated to be non-conformal and this can affect and can lead to problems when trying to get the solution to converge. Another issue that might contribute to the sliding mesh approach being computationally expensive is the fact that one need to set an initial condition. This means that if our initial guess isn't quite accurate, a lot more rotations of the impeller would be necessary and as stated above, for accurate results we need at least 360 timesteps per revolution. This means that running the simulation to convergence can be expensive.

Due to these downsides, we must come up with a way of not physically rotating or sliding a mesh region. This is the principal purpose of the moving reference frame. That's to say, rendering an unsteady problem in the inertial (stationary) frame with respect to the moving frame enabling us to find a relatively accurate solution in steady state [116, 121]. This would significantly cut down the cost of running the simulation as well as providing a suitable initial condition should you desire to still use the sliding mesh approach. Despite the advantages over the sliding mesh approach, the MRF approach does have the downside of being unable to account for impeller-baffle transient interactions [58].

Where the MRF method is employed, we would solve a single set of Navier-Stokes equations for the entire mixing tank with extra source terms in the region that is rotating. The extra source terms are produced by introducing three variables, the relative velocity U_r, the distance vector r, and the rotation vector Ω (the rotation vector is the product of the axis of rotation and the speed of rotation). The relationship between these three variables and the global velocity U is given by:

$$U = U_r + \Omega \times r$$

(7.3)

When substituted into the incompressible Navier-Stokes equation and performing some careful rearrangement we end up with the Navier-Stokes equation adopting the form:

$$\underbrace{\nabla.(UU_r)}_{\substack{convection\\Term}} = -\nabla P + \nabla.(v\nabla U) - \underbrace{\Omega \times U}_{\substack{source\\Term}}$$

(7.4)

This derivation has one additional source term that is only applied in the rotating region (region occupied by the impeller) with the unknown being the inertial/global velocity. The presence of the relative velocity and global velocity in the convection term brings up the issue of having two different velocity variables which is resolved in the CFD code via the finite volume discretisation method.

7.1 Finite Volume Discretisation

In the MRF approach, the Navier-Stokes equation is modified in the moving/rotating zone by adding an additional source term as well as performing a volume flux correction due to the presence of the relative velocity, U_r in the convection term.

Consider therefore the integrated form of the Navier-Stokes equation over a specific volume, in this case the volume of each mesh:

$$\int_V [\nabla.(UU)]dV = \int_V \left[-\frac{1}{\rho}\nabla P\right]dV + \int_V [\nabla.(v\nabla U)]dV$$

(7.5)

Drawing particular focus to the convection term:

$$\int_V [\nabla.(UU)]dV$$

(7.6)

Gauss' divergent theorem is then employed to manipulate the convection term. This is particularly useful in that it converts the integral from being limited by the volume to being limited by the surface area. That's to say, it converts the integral of the volume over the divergence to the surface integral across the bounded volume [122]. This means that the shape of the mesh doesn't matter if the volume is taken as finite. The resultant relationship is:

$$\int_V [\nabla.(UU)]dV = \int_s [U(U.\hat{n})]ds$$

(7.7)

where V denotes the volume and S is the bounded surface with $\hat{n}$ being the outward pointing normal unit vector at the face of the bounding surface [109]. Due to divergence being a net outflow of flux from a given control volume, in simple terms the Gauss's theorem also known as the divergence

theorem can be phrased as the rate of accumulation of a given material in the unit cell of the mesh must be equivalent to the flux of that material over the bunding surface of the cell that is the total outflow from that cell [123, 124].

It should be noted that equation above is for all bounding faces. The finite volume method involves splitting up this derivation such that you have:

$$\int_s [U(U.\hat{n})]ds = \sum_{faces} \int_s [U(U.\hat{n})]ds$$

(7.8)

Due to quantities having a linear variation of quantities across both the face and the cell the value of the integral function can be represented as a product of the value at the centre of the surface face and the area of the face.

$$\sum_{faces} \int_s [U(U.\hat{n})]ds = \sum_{faces} \underbrace{U_c(U_c.\hat{n}_c)A_c}_{\substack{face\ volume \\ flux}}$$

(7.9)

This is known as the face volume flux where A_c is the area of the face and U_c is the velocity vector at the centre of the face. Consider equation,

$$U_r = U - (\Omega \times r)$$

(7.10)

In the MRF method, where the convection term contains both the global and inertial velocity, the face volume flux will also contain a relative velocity component:

$$\sum_{faces} U_c(U_r.\hat{n}_c)A_c$$

(7.11)

Substituting equation to eliminate the relative velocity we arrive at:

$$\sum_{faces} U_c(U_r.\hat{n}_c)A_c = \sum_{faces} U_c(U_c.\hat{n}_c)A_c - \sum_{faces} U_c((\Omega \times r).\hat{n}_c)A_c$$

(7.12)

The second part of the solution, $\sum_{faces} U_c((\Omega \times r).\hat{n}_c)A_c$, is known as the flux correction as its purpose is to change the standard face volume flux to account for the relative velocity in the moving section of the mesh.

This is the basis for the finite volume discretisation.

8 Optimisation of The Mixing Tank CFD Parameters

The purpose of optimisation is to maximise or minimise a quantity called the objective (for instance time). In this thesis, the method used to optimise the simulation process is based in part on a statistical method called factor analysis. Factor analysis as described by Alkarkhi et al., [125] is a multivariable technique that describes how different variables that are under observation (for instance mesh size and residual criteria) relate to another set of variables (convergence point and solution time) and includes both a principal component analysis as well as common factor analysis [126]. To optimise the simulation runs, principal component analysis was used. This is a statistical technique that is useful in taking a large number of data sets and reducing it to a few meaningful ones capture the essence of the entire data set [127]. In this case it was used to deduce the optimal absolute criteria for convergence and the optimal element size for meshing.

8.1 Geometry construction and Setup

The mixing tank was constructed using AutoCAD. The mixing tank design was that of a fully filled closed mixing. The mixing tank had the following dimensions:

Table 8-1Table of mixing tank dimensions.

Part Name	Component Name	Dimensions (m)
Impeller (I)	Impeller diameter (I_d)	0.54
	Impeller shaft diameter ($I.S_d$)	0.108
	Impeller shaft height ($I.S_h$)	0.72
	Impeller paddle thickness (I_{th})	0.04
Tank (T)	Tank height (T_h)	1.08
	Tank diameter (T_d)	1.08
Baffle (B)	Baffle length (B_l)	0.18
	Baffle height (B_h)	1.08

	Baffle thickness (B_t)	0.045
Moving fluid zone (F)	Diameter (F_d)	0.58
	Height (F_h)	0.16

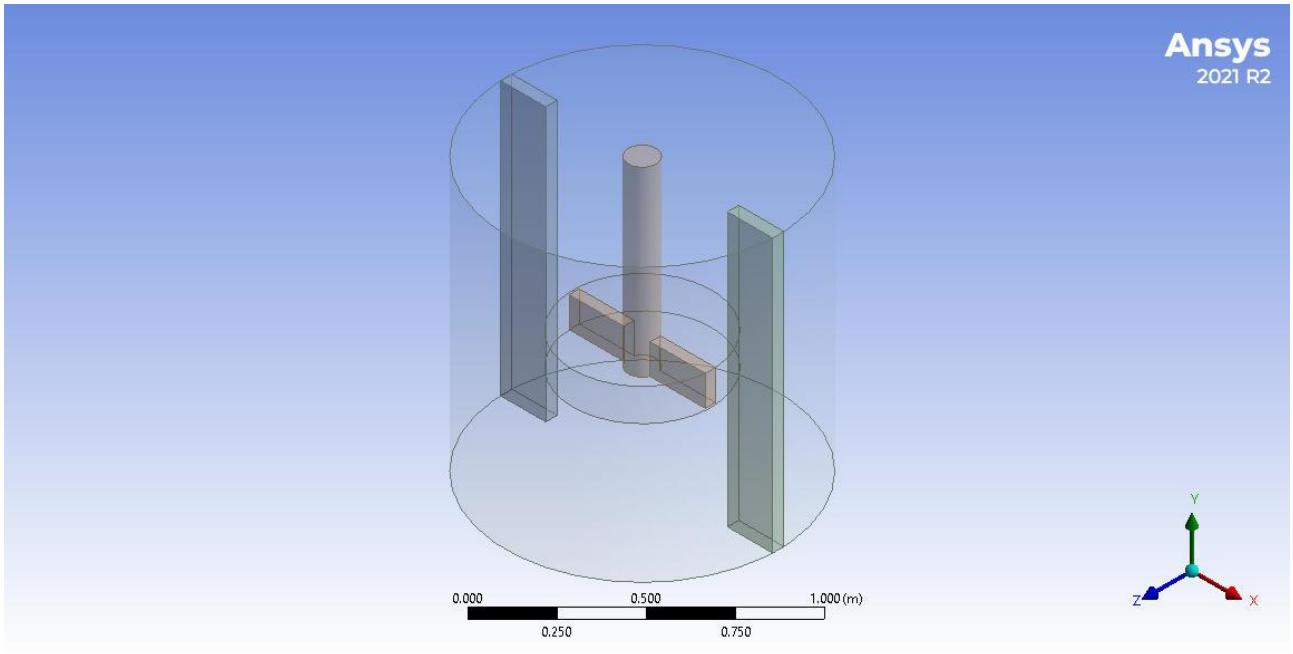

Figure 8-1 Stirred tank reactor image as it appears in designmodeler.

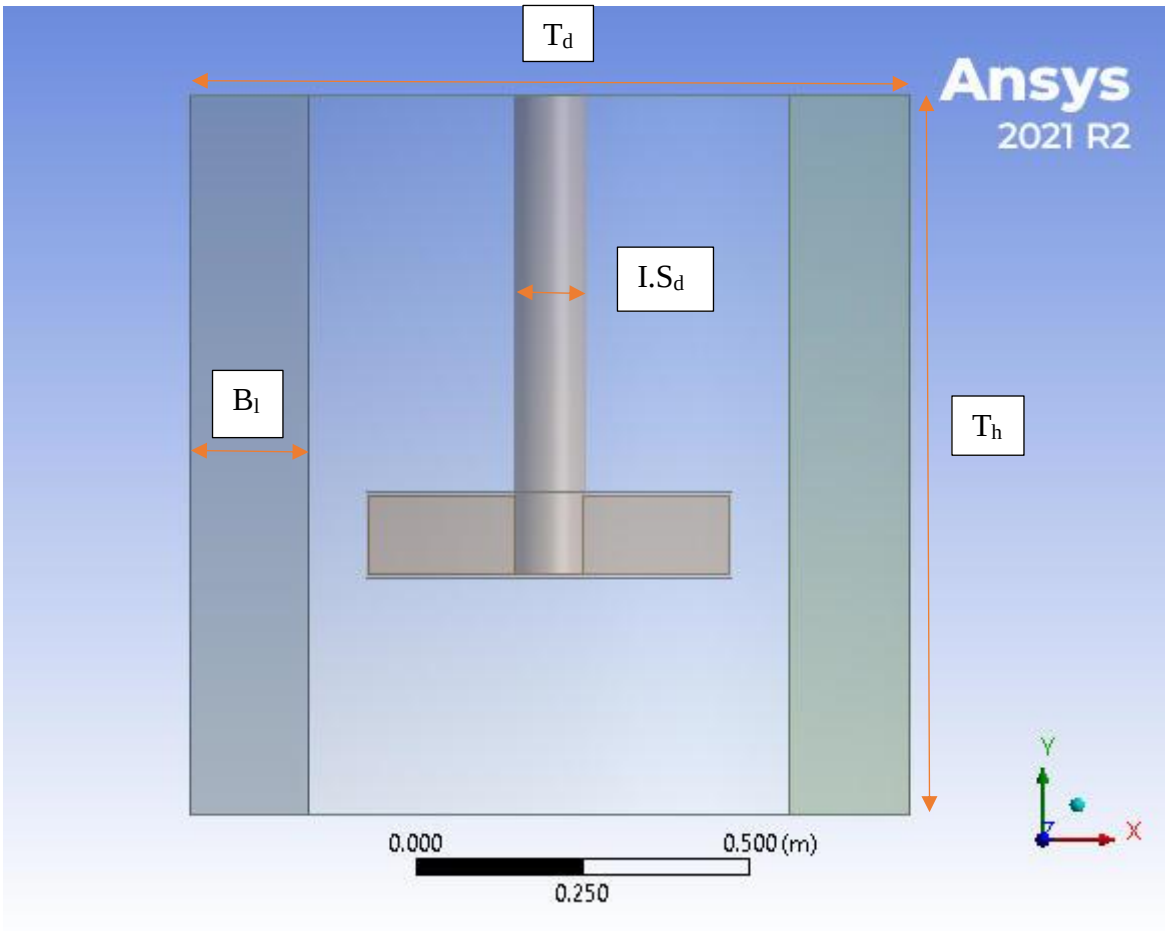

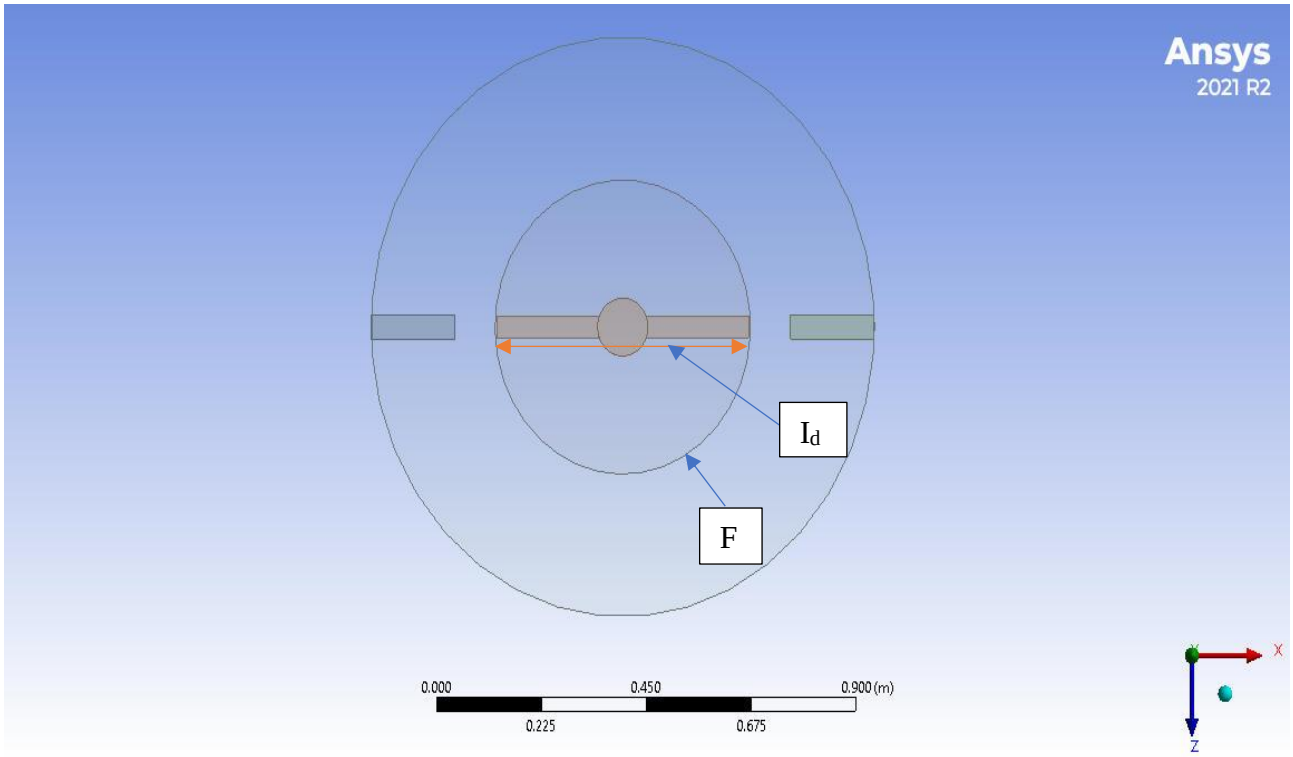

Figure 8-2 Annotated mixing tank.

The mixing tank diameter was sourced from stirred tank reactors supplied by an industrial supplier called ‘Frank Berg industrial supplies and more’.

8.1.1 Geometry design setup and mesh setup

A new fluid flow (fluent) project was started. The design from AutoCAD was then imported to DesignModeler.

A Boolean operation was then employed to eliminate the solid internals of the mixing tank for meshing and CFD analysis. In this case, the baffles and impeller. This allows the remaining zones to only consist of fluid zones. The moving fluid zone and stationary fluid zones were then separated from one another using a Boolean operation. This is an important step as it enables the creation of the fluid-fluid interface within the mixing tank which facilitates the multiple reference frame model.

8.2 Meshing

The next step of the simulation was to generate the mesh file. The mesh was generated using ANSYS Meshing. The first step involved naming all the faces. Named selections were created to make setting operating conditions in Fluent Setup easier. This was followed by setting the mesh of the system to a patch conforming tetrahedral mesh.

The mesh element size was then set. This is important as it is a variable in the optimisation process. The table below displays the designated element sizes.

Table 8-2 The element sizes of the moving and stationary zones.

Moving Fluid zone	**Stationary Fluid Zone**
0.01m	0.01m
0.0125m	0.0125m
0.015m	0.015m
0.0175m	0.075m
0.02m	0.02m
0.025m	0.025m
0.03m	0.03m

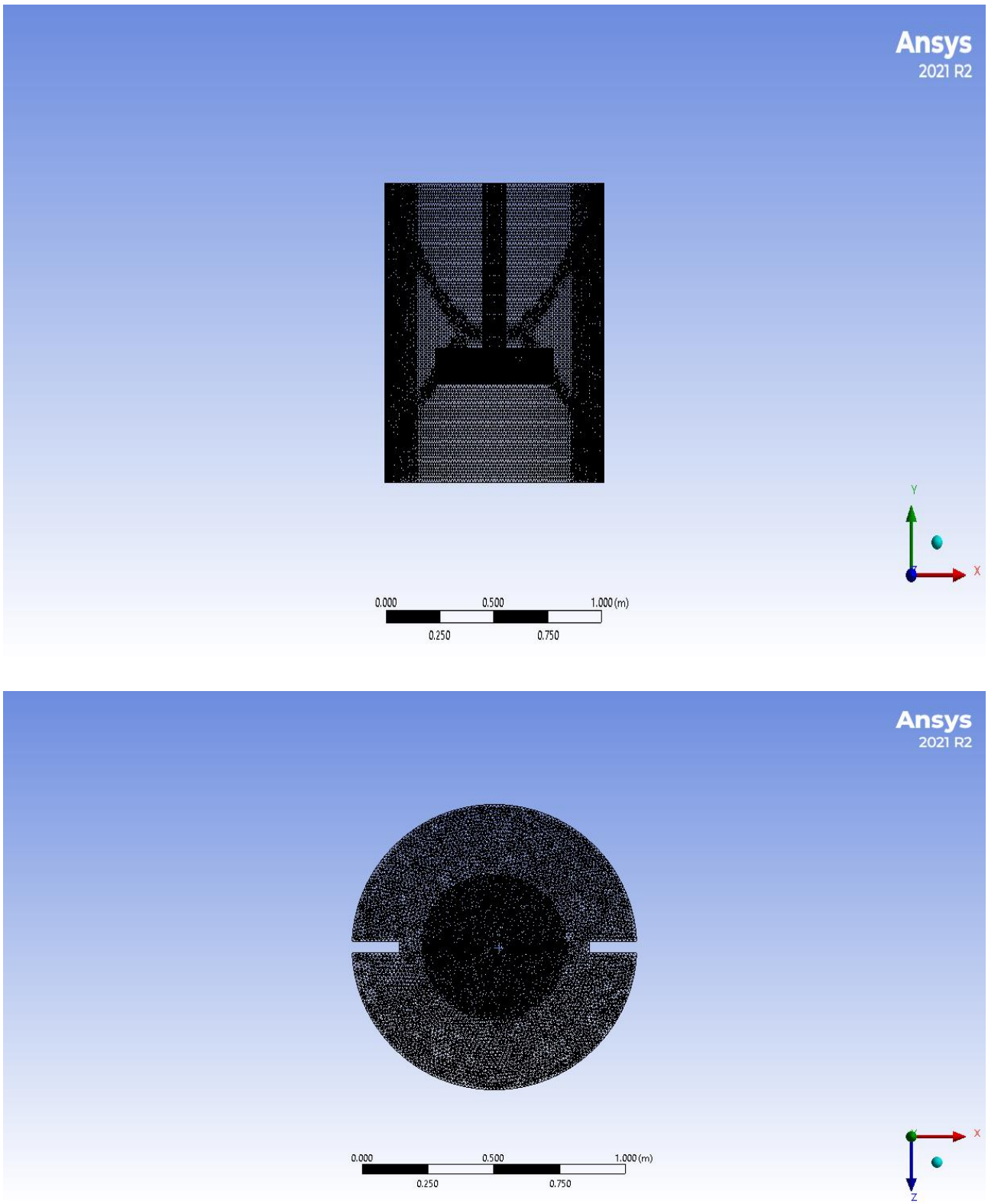

Figure 8-3 mesh of optimised mixing tank with the standard baffle design

8.3 Simulation setup

The first step of the actual simulation involved setting up the general physical parameters. As such, gravity was enabled and set to the global gravity of -9.81m s^{-2} acting in the y-axis. The computational

units were then defined with the angular velocity being set to revolutions per minute as opposed to the default units of radians per second.

The next stage involved designating the solution models to be employed. There are various turbulence models available. These are shown below along with a brief description in Table *8-3*.

Table 8-3 Types of turbulence models.

Turbulence model	Description
Standard $\boldsymbol{k-\varepsilon}$	A robust model. Very widely used industrially due to this as well as its ability to rapidly calculate reasonable and stable results especially when it comes to flows with high Reynolds numbers. However, it is not well suited for high swirling flows and flows with high separation. [128]
RNG $\boldsymbol{k-\varepsilon}$	A modified version of the $k-\varepsilon$ model which benefits from improved results with flow separation and swirling flows. It however does not share the stability of the standard $k-\varepsilon$ model [128].
Realizable $\boldsymbol{k-\varepsilon}$	A modified version of the $k-\varepsilon$ model with much more improved results with high swirling flows and high separation flows [128].
LES (Large eddy simulation)	A transient formulation requiring a lot of computational power and is excellent for all systems. A very fine grid is also needed to gain maximum benefit from this model [128].
RSM (Reynolds Stress Model)	Provides good predictions of all types of flows. However has much longer solution times than all the $k-\varepsilon$ models as it solves the transport equations for the Reynolds stresses directly [128].
Scale adaptive simulation	This method is divided into two computational regions where the outer region is modelled using the LES model while the RANS (Reynolds Averaged Navier Stokes) model is used for the inner layer [129].

The viscous model used was realizable k-ε. The near-wall treatment was specified to be standard wall functions. The material under investigation was water. The rotation velocity for the moving fluid zone was specified as 750 rpm with a y axis of rotation. The pressure operating condition was set to atmospheric (101325 Pa).

Table 8-4 operating parameters

Viscous model	Realizable k-ε
Near wall treatment	Standard wall function
Rotational velocity	750 rpm
Pressure	101325 Pa

The nature and types of wall movements for each region were then set for the fluid-to-fluid interactions in the system. This is crucial for areas where there is an interface for an MRF system. The contact wall closest to the moving fluid zone and adjacent to the interface was stated to be a moving wall. This means that there is no hard boundary between the moving fluid and the stationary fluid. Its motion was also stated to be relative to the adjacent cell zone with its motion being rotational as opposed to translational and at a speed of 0 rpm as is standard in an MRF approach. An identical set of conditions was applied to the internal wall that is directly in contact with the interface and stationary fluid zone.

8.4 Solution

8.4.1 Method

The pressure velocity coupling system selected was the semi-implicit method for pressure linked equations (SIMPLE) scheme. This is based on deriving an equation to describe the pressure from momentum and continuity equations and from this, calculating the pressure field via iterating an initial guess to the actual value with a corrector to the velocity field to ensure that the continuity equation remains satisfied. This velocity corrector is based on the pressure field thus the SIMPLE algorithm can sometimes be referred to as a pressure corrector algorithm [130] .

The spatial discretisation was then set as shown in Table *8-5*.

Table 8-5 Table of the spatial discretisation factors used to simulate the mixing tank.

Gradient	Least square cells based
Pressure	Second order
Momentum	Second order upwind
Turbulent kinetic energy	Second order upwind
Turbulent dissipation rate	Second order upwind

The under-relaxation factors were left as default as is standard practise. This is due to them being optimal and relevant to the largest number of case studies[116].

The criteria for convergence were then set up through the absolute criteria for all the residuals. The residuals for the run were continuity, x-velocity, y-velocity, z-velocity, k and epsilon. The convergence criteria were set to absolute. Each of the seven mesh element sizes was simulated under multiple absolute criteria. For the optimisation process, the absolute criteria for convergence were 2.5×10^{-4}, 5×10^{-4}, 7.5×10^{-4}, 1.0×10^{-3}, 1.5×10^{-3}, 2.0×10^{-3}, 2.5×10^{-3}, 3.0×10^{-3} and 3.5×10^{-3}. Each simulation was solved via hybrid initialization and set to a maximum of 2000 iterations for a solution to be reached.

8.5 Results and data analysis

8.5.1 Geometry scale

Table 8-6 Mixing tank geometry scale.

X_{min}	-0.31m	X_{max}	0.77m
Y_{min}	0m	Y_{max}	1.08m
Z_{min}	-1.42m	Z_{max}	-0.35m

This means that the co-ordinates of the origin of the mixing tank (centre of the mixing tank base) is 0.23, 0, -0.88. This is identical for all the mixing tank designs throughout this thesis.

The scale above is useful in creating locations for analysis.

8.5.2 Effect of convergence criteria and mesh size on convergence

Simulations were carried out under different conditions via altering the absolute convergence criteria and mesh geometry. The resultant time taken for convergence and number of iterations required for

convergence (convergence point) were recorded for optimisation. These results are shown from Table *8-7* –

Table *8-13*.

Table 8-7 The convergence time vs absolute criteria for grid size 1 cm.

Element size	**1 cm**	
Absolute criteria	time (s)	convergence point
0.00025	13086.44	790
0.0005	4009.174	258
0.00075	3815.491	226
0.001	3332.884	215
0.0015	2343.068	147
0.002	2254.093	136
0.0025	2380.213	118
0.003	1600.575	99
0.0035	1489.742	93

Table 8-8 The convergence time vs absolute criteria for grid size 1.25 cm.

Element size	**1.25 cm**	
Absolute criteria	Time (s)	convergence point
0.0005	2055.704	279
0.00075	1510.611	190
0.001	1856.433	177
0.0015	1456.676	161
0.002	783.825	107
0.0025	770.234	102

0.003	790.572	98
0.0035	670.421	94

Table 8-9 The convergence time vs absolute criteria for grid size 1.5 cm.

Element size	**1.5 cm**	
Absolute criteria	time (s)	convergence point
0.0005	1637.47	373
0.00075	784.307	169
0.001	631.29	152
0.0015	624.48	139
0.002	492.391	110
0.0025	388.819	86
0.003	384.398	83
0.0035	373.212	81

Table 8-10 The convergence time vs absolute criteria for grid size 1.75 cm.

Element size	**1.75 cm**	
Absolute criteria	time (s)	convergence point
0.0005	3250.815	1296
0.00075	523.871	204
0.001	394.349	137
0.0015	355.33	124
0.002	319.098	112
0.0025	276.807	89

0.003	190.109	73
0.0035	182.114	71

Table 8-11 The convergence time vs absolute criteria for grid size 2 cm.

Element size	**2 cm**	
Absolute Criteria	Time (s)	convergence point
0.00075	1879.883	1016
0.001	258.918	137
0.0015	210.815	109
0.002	186.534	100
0.0025	188.859	88
0.003	129.014	65
0.0035	158.524	63

Table 8-12 The convergence time vs absolute criteria for grid size 2.5 cm.

Element size	**2.5 cm**	
Absolute criteria	time (s)	convergence point
0.001	1051.753	1042
0.0015	648.719	707
0.002	90.688	87
0.0025	75.302	81
0.003	72.142	74
0.0035	65.299	65

Table 8-13 The convergence time vs absolute criteria for grid size 3 cm.

Element size	**3 cm**	
Absolute criteria	time (s)	convergence point
0.0015	517.261	1013
0.002	395.81	714
0.0025	336.154	568
0.003	291.366	511
0.0035	31.692	63

A cursory view of the above tables shows that the time taken for the solution to converge as well as the number of iterations required for the simulation to arrive at the solution was affected by a combination of the element size of the mesh as well as the absolute criteria for convergence.

As such, for an optimal run the above data was used to get the ideal mesh size and absolute criteria through principal component analysis-based factor analysis.

8.6 Determining the Optimised mesh element size and convergence point

8.6.1 Factor analysis and principal component analysis

The purpose of factor analysis and principal component analysis is to act as dimensionality reduction techniques. That means that they are used to compress a large set of data to a few meaningful data points. For instance, factor analysis performs this by creating a model that seeks to explain shared/common variance between a set of observed variables (e.g., time taken to run a simulation) in a population by a set of typically fewer unobserved factors and assigning weightings to each factor[131]. PCA (Principal component analysis) varies slightly in that it employs total variance as opposed to shared variance as in the case of FA.

Due to the large quantity of data, a proprietary program written by Lande Liu [127] was used to extract the optimised values. The two main results are shown in Figure 8-4Figure 8-5 below.

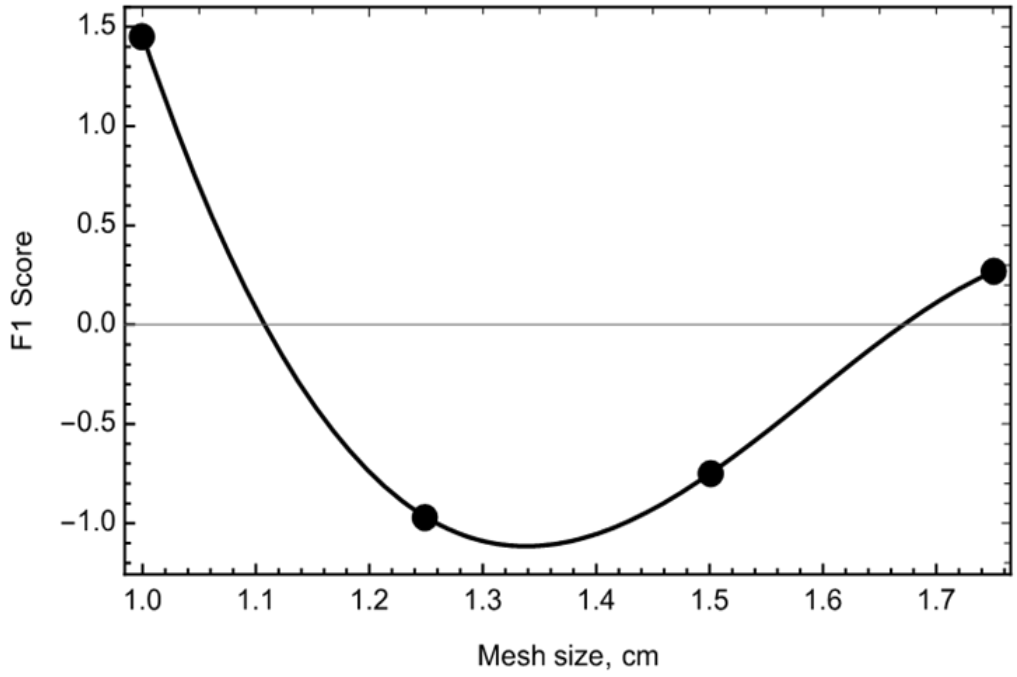

Figure 8-4 F1 score vs Mesh size.

Where the F1 score, sometimes called f score, is a metric of how close a factor adheres to a given model. In Figure 8-4, the scores on the first major factor vs mesh size plot gives the indication that the minimum score (implying the convergence time) was at a mesh size of 1.34 cm. This is our first optimised variable.

The next desired variable is the absolute criteria for convergence. Figure 3 shows the plot of the F1 scores vs residual criterion. As seen in this figure, there are two local minimums in this interested region. The minimum on the left was taken to be the optimised residual for the simulation. This was because if the residual on the right is taken, a larger error can be expected as the computation precision is reduced. Therefore, the left minimum (1.3×10^{-3}) is a compromise of less error relative to slightly longer convergence time (indicated by the value of F1 score).

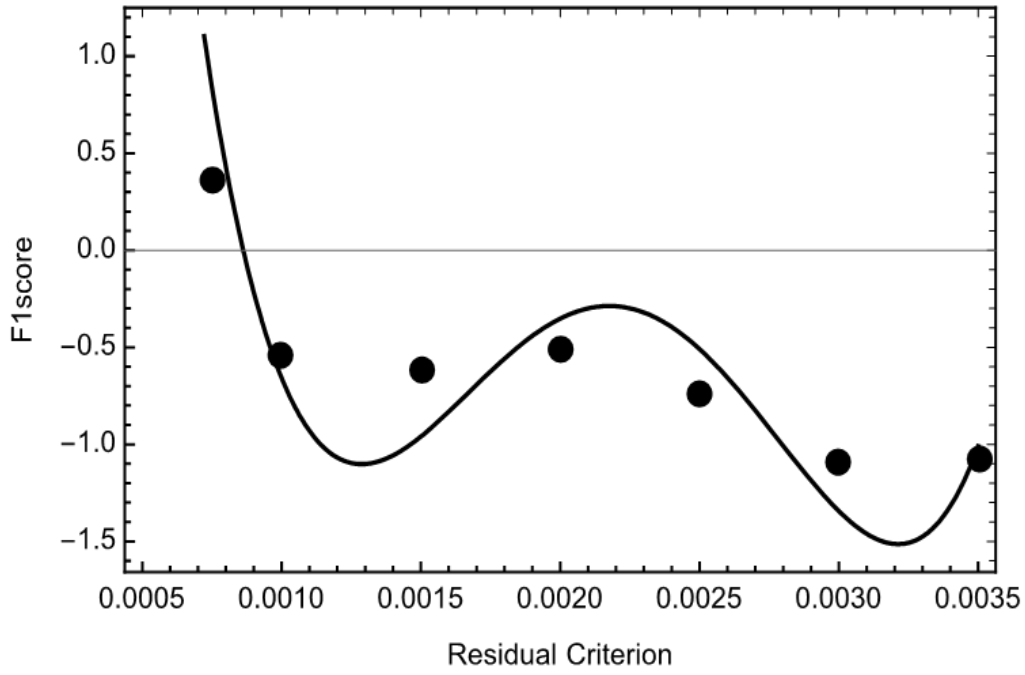

Figure 8-5 F1 score vs residual criteria.

Therefore, for optimal simulation the mesh generation is limited to an element size of 1.34×10^{-2} m for both the moving and stationary fluid zones as well as an absolute convergence criterion of 1.3×10^{-3} for each residual.

8.7 Simulation results with optimised mesh size and convergence criterion

8.7.1 Pressure & velocity distribution

The purpose of this was to find out how the stirred fluid was affected by the baffles at various location of the mixing tank design.

8.7.1.1 Region along the tank wall

Data was extracted along the wall of the mixing tank parallel to the impeller paddles at several points. This was done at 6 points labelled A, B, C, D, E and F. The locations for these points can be seen in Table 8-14.

Table 8-14 Table of co-ordinate locations for point A-F.

Point	**X**	**Y**	**Z**
A	0.227814	0.42	-0.4349
B	0.546012	0.42	-0.566702
C	0.64356	0.42	-0.712693
D	0.669167	0.42	-0.79711
E	0.675647	0.42	-0.840792
F	0.677272	0.42	-0.86282

The arc length between points A and the baffle centre is twice of the arc length between point B and the baffle centre which is again twice the distance between C and the baffle centre with the same principal kept up to the distance between F and the baffle centre. Each point was at a height of 0.42m.

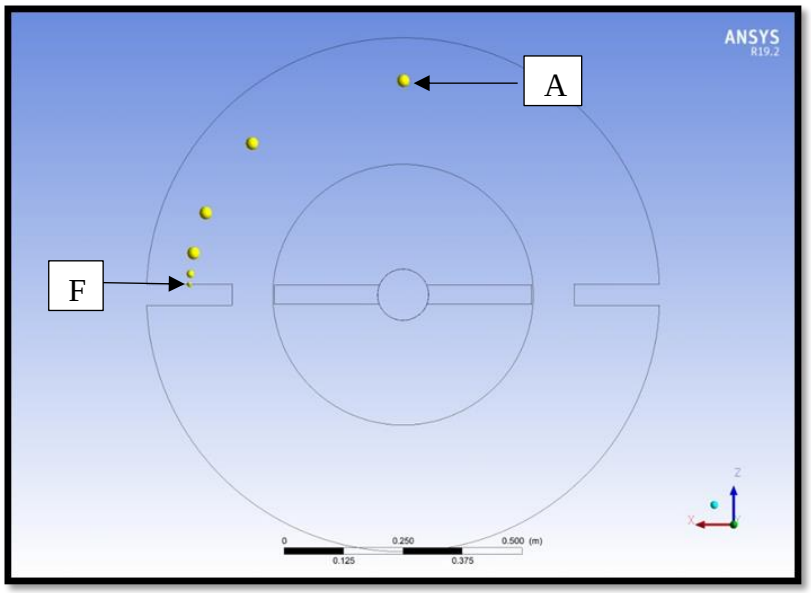

Figure 8-6 Image of points of analysis A-F.

Below is the pressure data obtained at each point.

Table 8-15 Table of pressure data at different locations for the optimised simulation.

Location	Arc length from baffle midpoint (m)	Pressure (Pa)
A	0.708858	-5.12E+04
B	0.353429	-6.79E+04
C	0.176715	-6.35E+04
D	0.088357	-5.96E+04
E	0.044179	-5.74E+04
F	0.022089	-5.95E+04

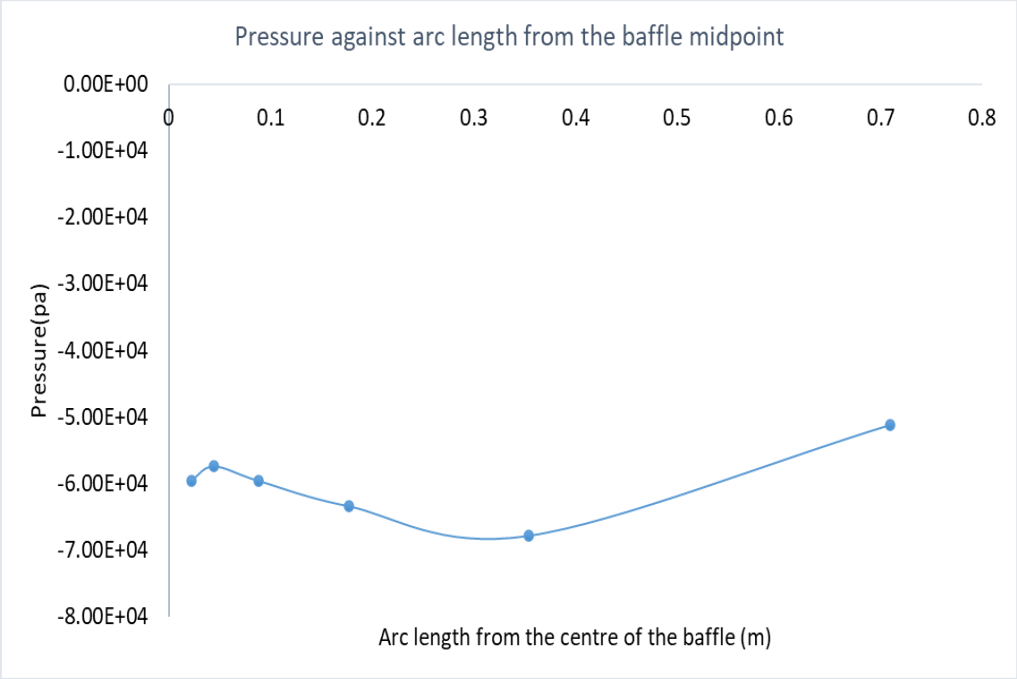

Figure 8-7 Pressure against arc length.

As can be seen from Figure 8-7, overall, the pressure does not vary a great deal, nevertheless, there was a local minimum pressure around the mid-point of B, which indicates there was a liquid sink indicating the direction of velocity is about to change.

Velocity magnitude data was also extracted from these same locations. This is given in Figure 8-8.

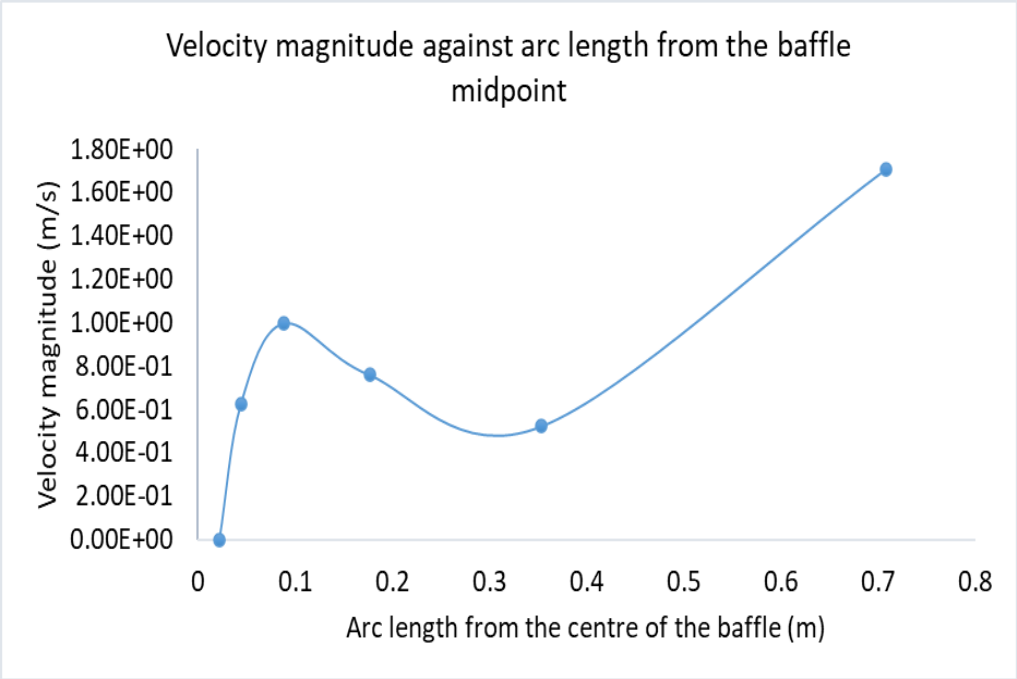

Figure 8-8 Velocity magnitude against arc length location.

As can be seen from Figure 8-8 and Figure 8-7, at the local minimum pressure position, the velocity was also local minimum. Interestingly, near the baffle mid-point, there was a local maximum that was also indicated in the pressure distribution in Figure 8-7. It is thus necessary to extract the velocity in the y direction as it will indicate a mixing of the fluid going up and down taking place.

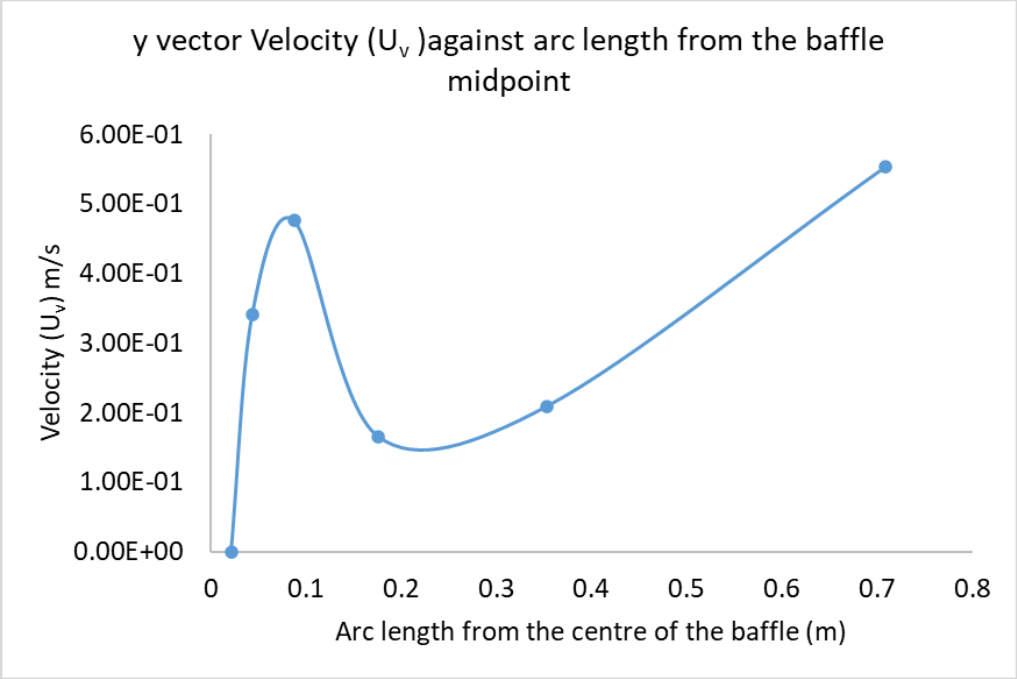

Figure 8-9 Y vector-velocity at points A-F.

As seen from Figure 8-9, as one moves further away from the baffle, the Y-direction velocity was generally larger indicating that the baffles were in fact halting the fluid going up and down thus perturbation of fluid becoming less active.

8.7.1.2 Y-axis location

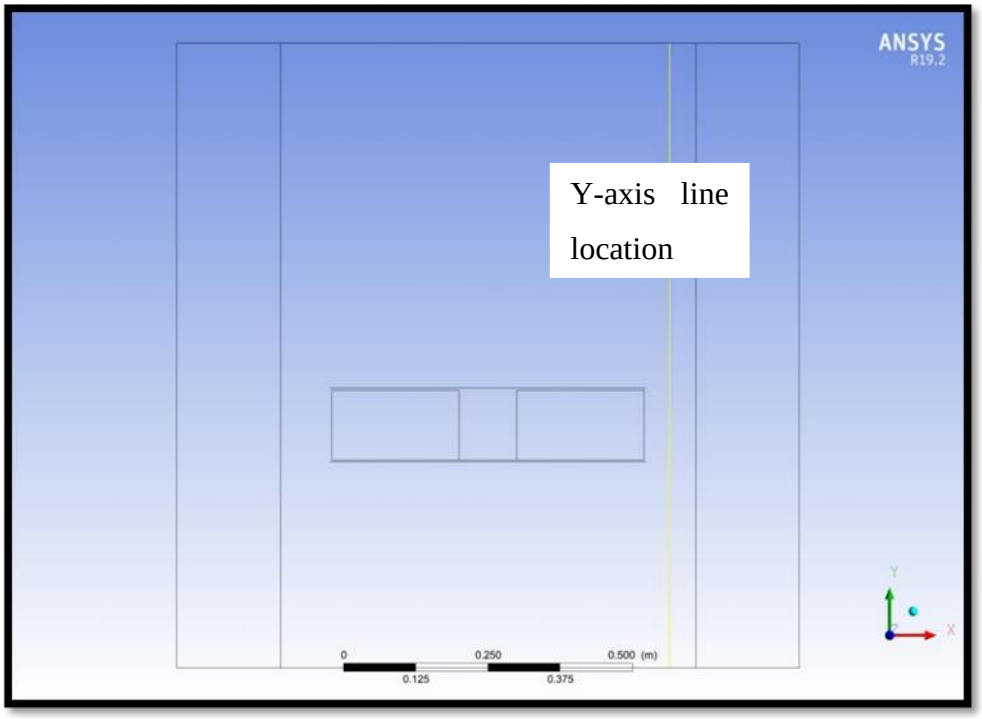

Figure 8-10 The y-axis location.

A vertical line as a point of interest was created midway between the baffle edge and the impeller edge running from the top to the base of the mixing tank (Figure 8-10). The velocity magnitude for the optimised run at this location was then extracted. For ease of discussion, this location shall be referred to as y axis location henceforth.

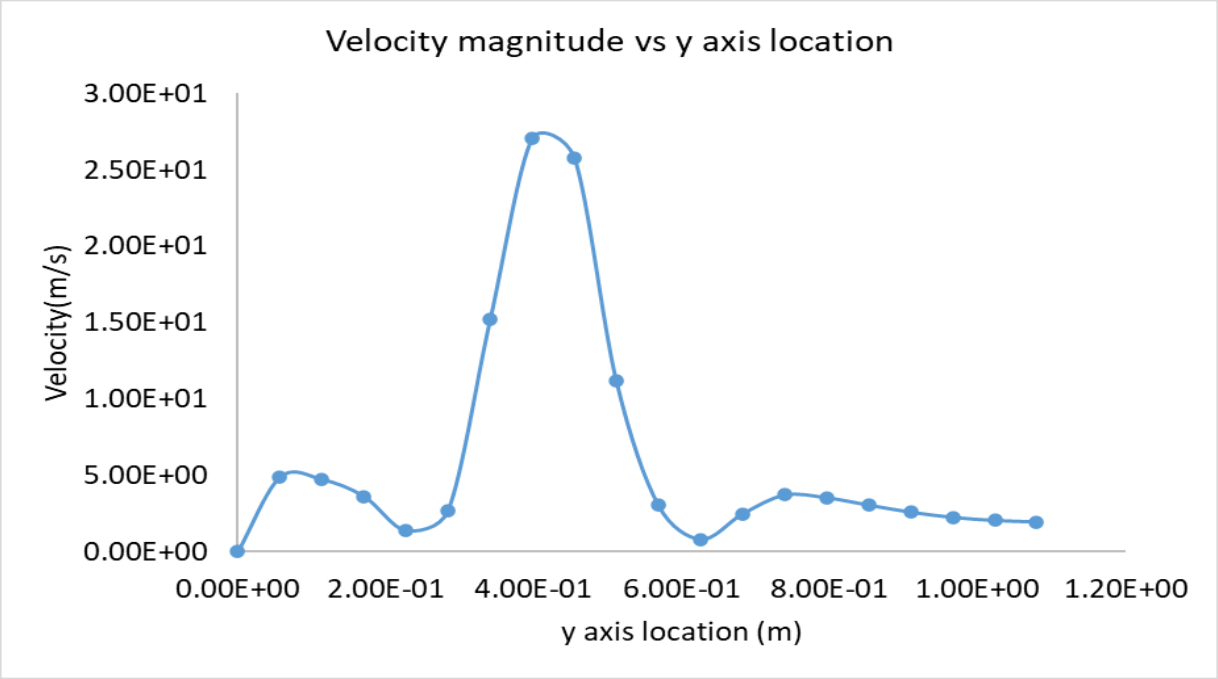

Figure 8-11 Overall velocity magnitude along the midway vertical plane.

Figure 8-11 indicates that the greatest agitation occurs in the region surrounding the impeller. This is indicated by the fluid having reached a maximum. Surrounding this maximum, the velocities below and above the impeller zone are quite symmetrically distributed, this indicates an up and down velocity distribution along the height of the mixing tank implying mixing is occurring.

Some more information can be drawn from the y vector velocity profile.

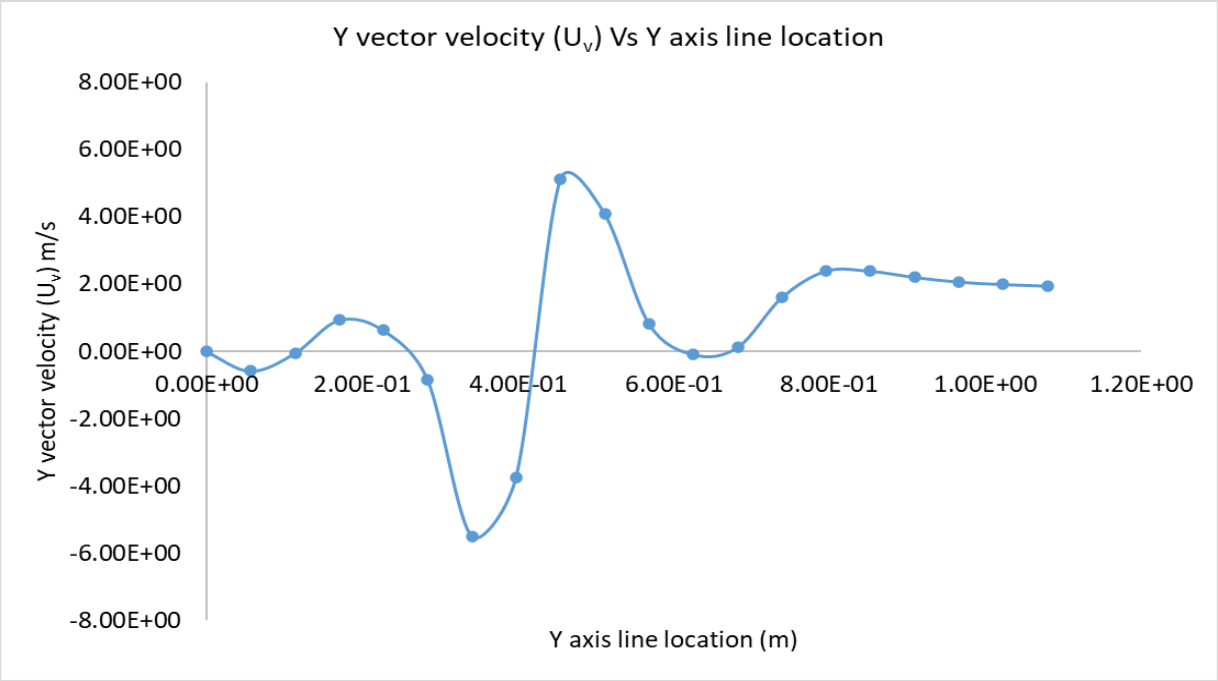

Figure 8-12 y-vector velocity along the vertical plane.

Figure 8-12 shows intensive mixing was occurring in the lower half of the vertical line as the y-velocities were changing directions. However, in the upper half of the line, the mixing is much less intensive as the velocities are almost all positive and stay at the same magnitude towards top of the tank.

It was also interesting to see the presence of two minima surrounding the maxima along the plane. This is indicative of mixing occurring extremely intensively in the area directly surrounding the impeller paddles.

8.7.2 X axis line location

Velocity data was also extracted along a line generated at half the distance between the impeller bottom and the bottom of the mixing tank. For ease of discussion this location will be referred to as x –axis location henceforth.

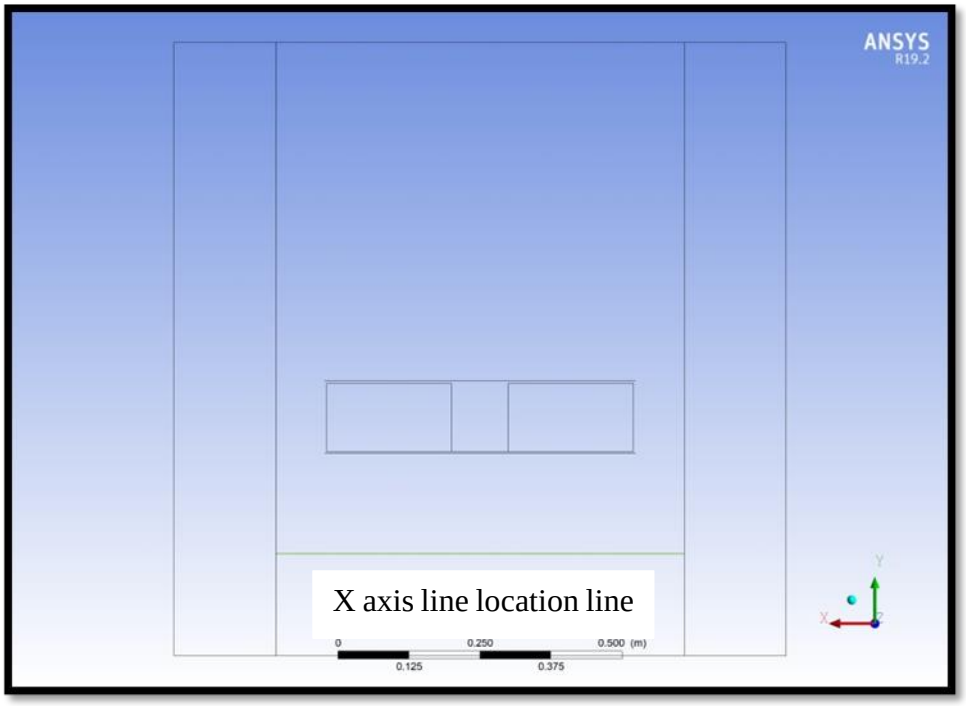

Figure 8-13 Illustration of location for analysis.

The velocity profile from this location is given in Figure 8-14 below.

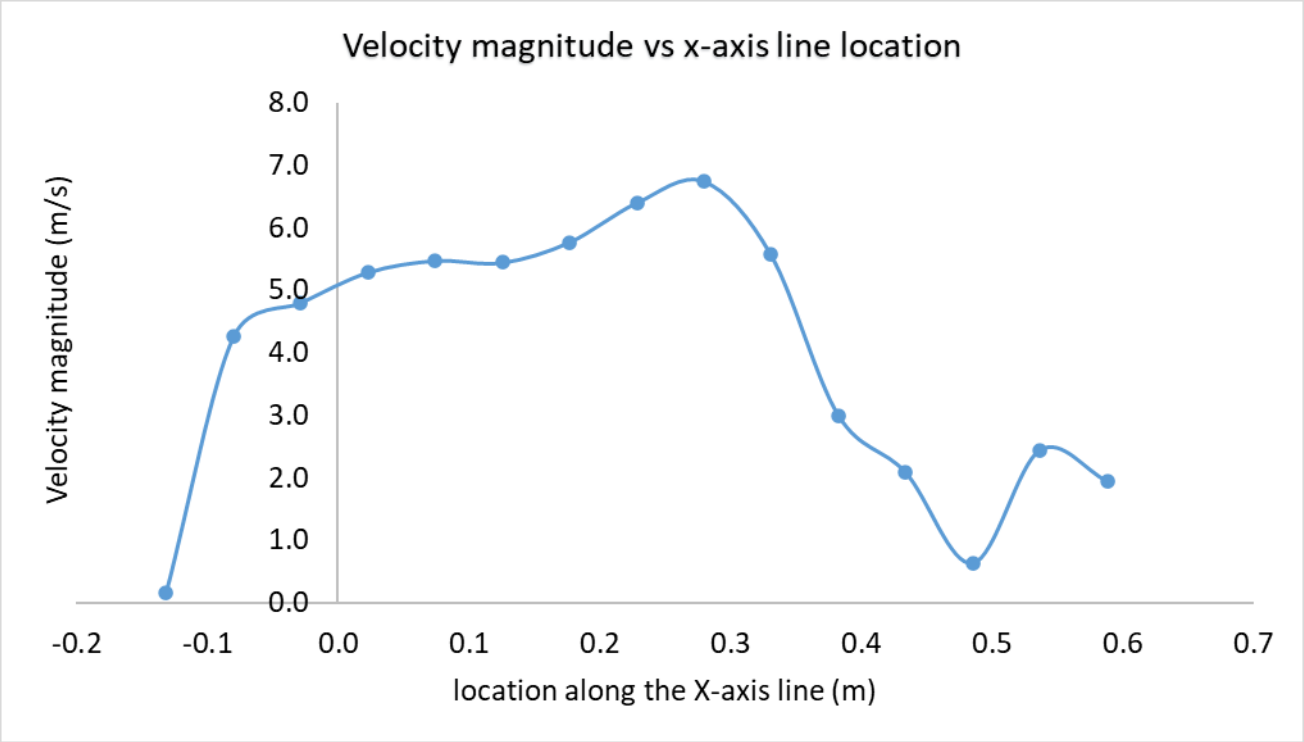

Figure 8-14 Overall velocity magnitude along the horizontal plane.

In general, the velocity magnitude observed at the x axis line location in the clearance region seems to be large and it is also interesting to see that there is a region where the fluid tends to gradually become static as seen towards the left part of the line as displayed in Figure 8-14. This may be due to the proximity to the baffle.

As for the y velocity vector the results are as shown below.

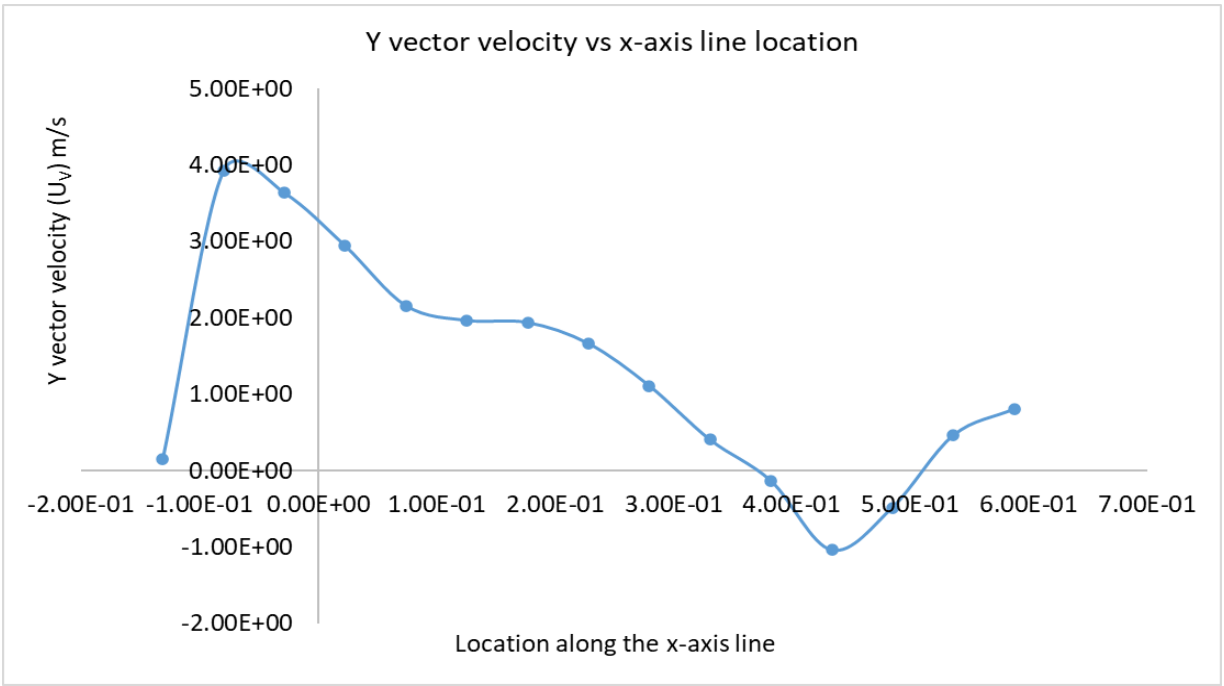

Figure 8-15 Graph of y-vector velocity along the horizontal plane.

Better mixing takes place towards the right side of the observation plane as indicated on the right side of the graph where the y-velocity crosses the horizontal axis that means the direction of the fluid moving is varying at this region. Nevertheless, on the left-hand side of the graph, there was a region where the fluid was moving up to reach its maximum velocity then gradually becoming stationary. A similar trend was observed in Figure 8-14.

8.7.3 A comparison of the optimised mixing tank with the original baffle configuration to the minimum and maximum mesh element size and absolute convergence criteria

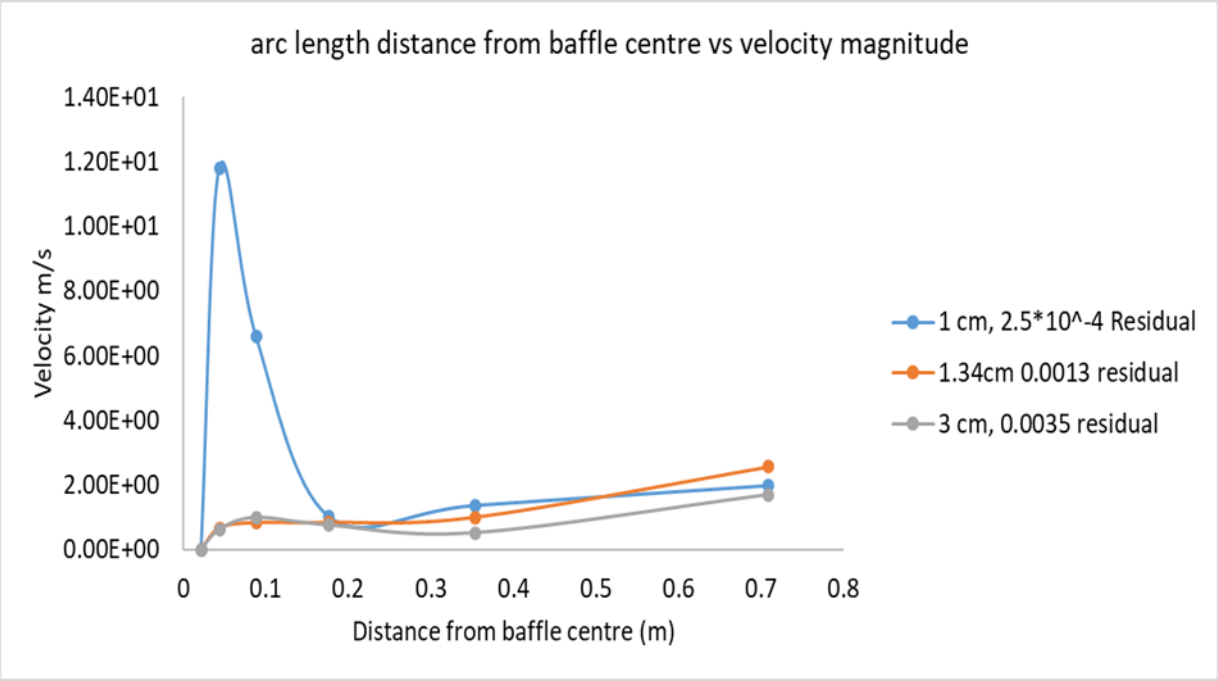

Figure 8-16 Curve of velocity magnitude vs arc length distance from the baffle centre.

The above graph represents a comparison chart between the optimised parameters of the simulation against the maximum and minimum residual and element size investigated. The difference in velocity values extracted is minimal unless the area of interest is directly adjacent to the baffle. This is observed in the range of $0 - 0.15$ m arc length distance. As such the optimised run still provides data with reasonable accuracy for a fraction of the computational time.

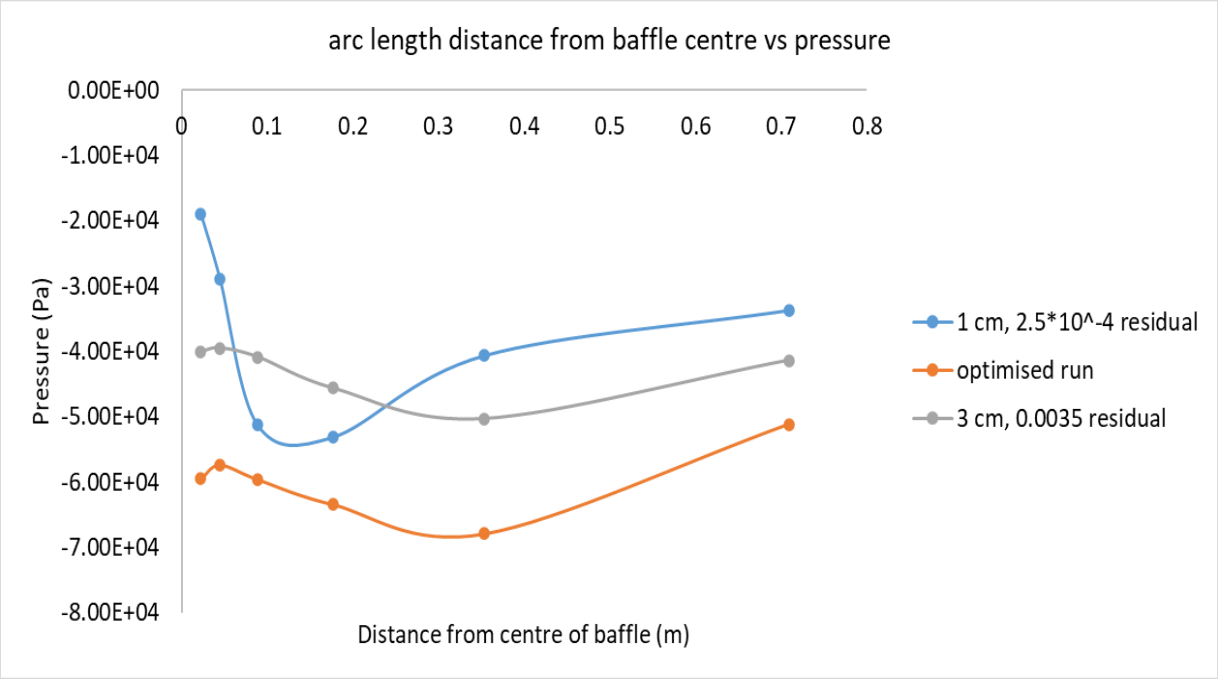

Figure 8-17 Curve of pressure vs arc length distance from the baffle centre.

The figure above follows the trend of the optimised run providing useful results with a similar amount of accuracy when compared to those of the 1 cm and 3 cm element size runs. Thus, the optimisation enables the saving of computational resources and time while maintaining accuracy.

8.8 Effect of baffle size on flow

Baffle dimensions influence the flow of fluids within a mixing tank. To examine this, various configurations of baffles were assigned to the mixing tank under consideration. For ease of description, they were each named according to the ratio of baffle thickness to baffle length.

Table 8-16 Dimension of baffles.

Baffle thickness (m)	Baffle length (m)	Ratio
0.045	0.18	1:4
0.045	0.09	1:2
0.18	0.18	1:1
0.36	0.18	2:1

8.8.1 Results at the y axis line location

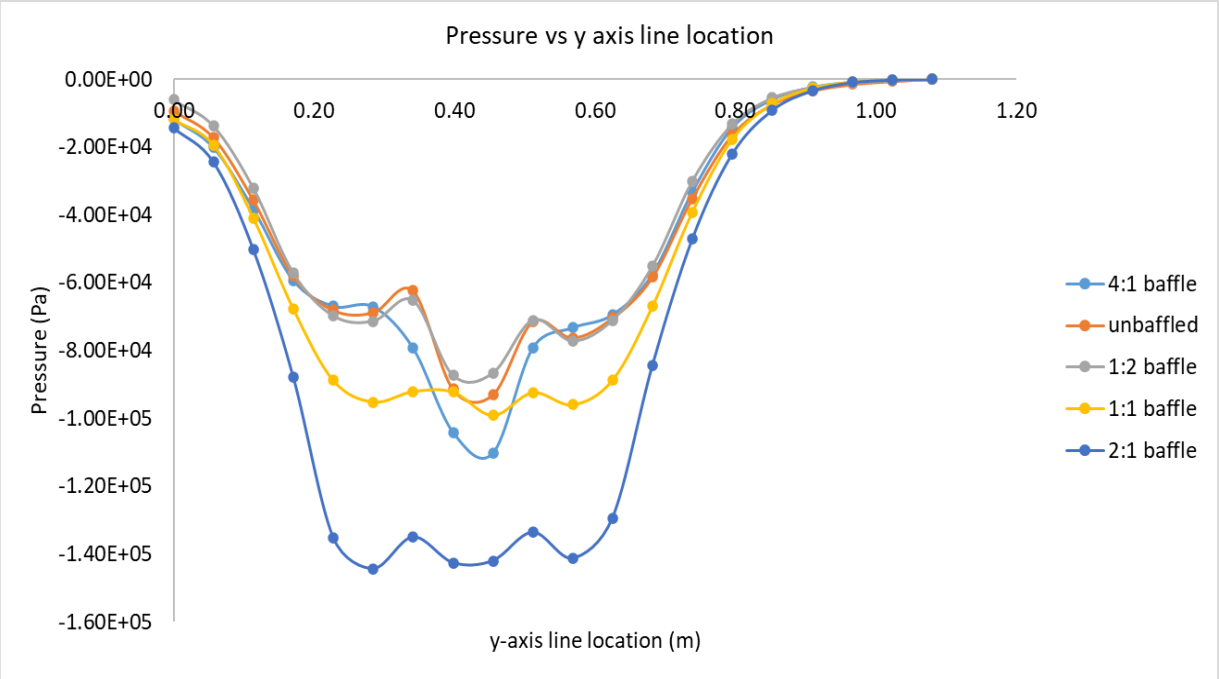

Figure 8-18 Pressure profile along the y-axis line location.

Figure 8-18 displays a pressure vs y-axis line location curve. The 2: 1 baffle provides the lowest pressure minima within the impeller zone. This is indicative of better mixing with the aid of this baffle as opposed to the other configurations.

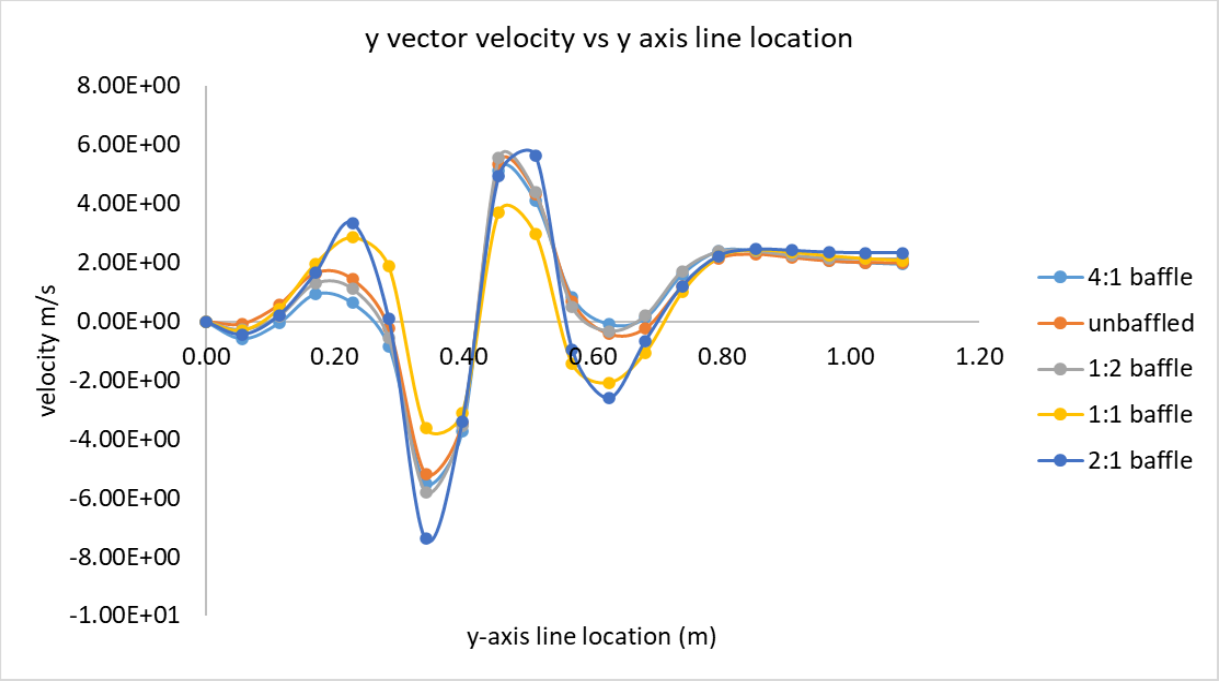

Figure 8-19 curve of y vector velocity vs y-axis line location.

From Figure 8-19, the y vector velocity along the vertical line (y axis line location) for the $2:1$ baffle provides the lowest minima of $-7.38\ \mathrm{m/s}$. This is lower than $-5.81\ \mathrm{m/s}$ for the $1:2$ configuration, $-3.62\ \mathrm{m/s}$ for the $1:1$ configuration, $-5.5\ \mathrm{m/s}$ for the $4:1$ baffle configuration and $-5.19\ \mathrm{m/s}$ for the unbaffled mixing tank. The maximum y vector velocity is similarly the highest for the $2:1$ baffle configuration with a value of $5.63\ \mathrm{m/s}$.

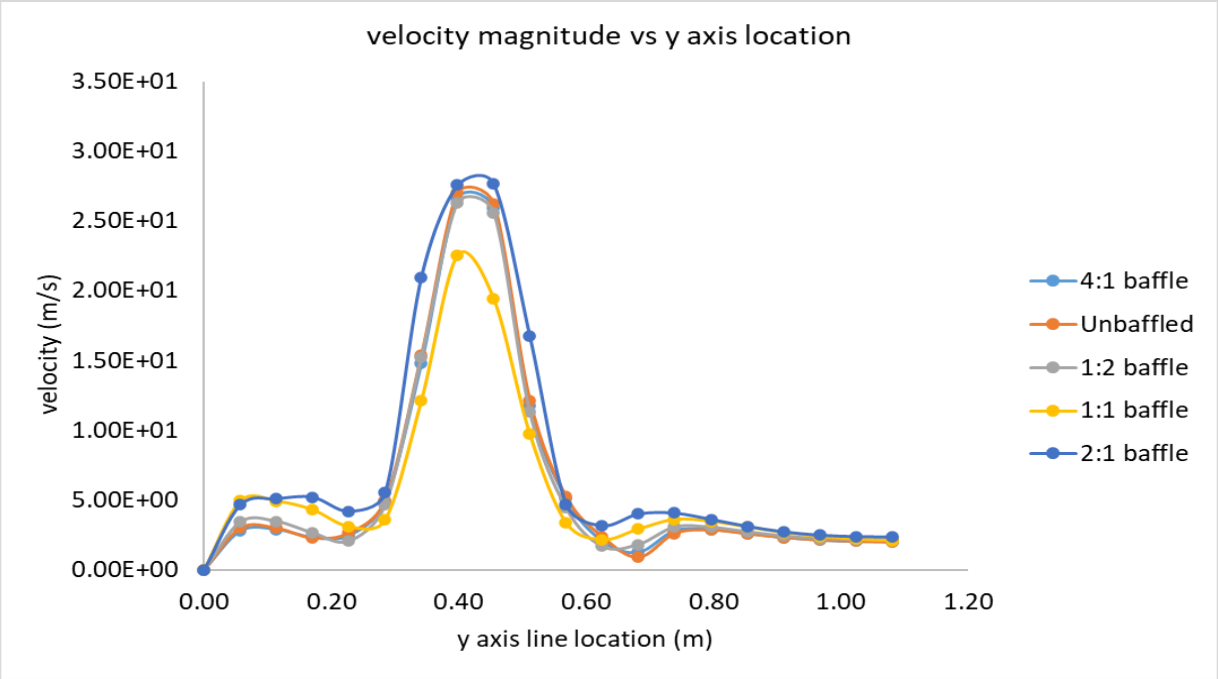

Figure 8-20 Graph of velocity magnitude along the y-axis location.

As expected, the region of maximum agitation is in the region occupied by the baffle ($y = 0.36$ m to $y = 0.48$ m). Like the y vector velocity graph in Figure 8-19, Figure 8-20 above demonstrates that the $2:1$ baffle configuration does generate the highest velocity magnitude of the 5 baffle configurations (including an unbaffled mixing tank) along the height of the stirred tank reactor. The velocity maximum was found to be $27.6\ \mathrm{m/s}$ for the 2:1 baffle configuration. This is greater than that of the 1:1 baffle at $22.6\ \mathrm{m/s}$, the 1:2 baffle at $26.3\ \mathrm{m/s}$, the unbaffled tank at $27\ \mathrm{m/s}$ and the 4:1 baffle at $26.6\ \mathrm{m/s}$. While this might seem high, it is consistent with what should be expected considering the impeller rotation speed. This promotes a very high radial speed that is the x and z velocity values. Since the velocity magnitude is the calculated as $\sqrt{{U_u}^2 + {U_v}^2 + {U_w}^2}$, a high radial velocity raises the overall velocity magnitude despite the relatively lower y velocity value.

The 2:1 baffle additionally has a moderately flatter curve, this points towards a more uniform distribution of agitation. This coupled with the greater maximum velocity magnitude provides further

evidence for the overall superiority of the 2:1 baffle configuration when compared to the other proposed baffle designs.

8.8.2 Results at the x axis line location

It needs to be noted that since the x axis line location is a line generated from baffle edge to baffle edge, it has different lengths for each baffle configuration. This can be seen in Table 12-1.

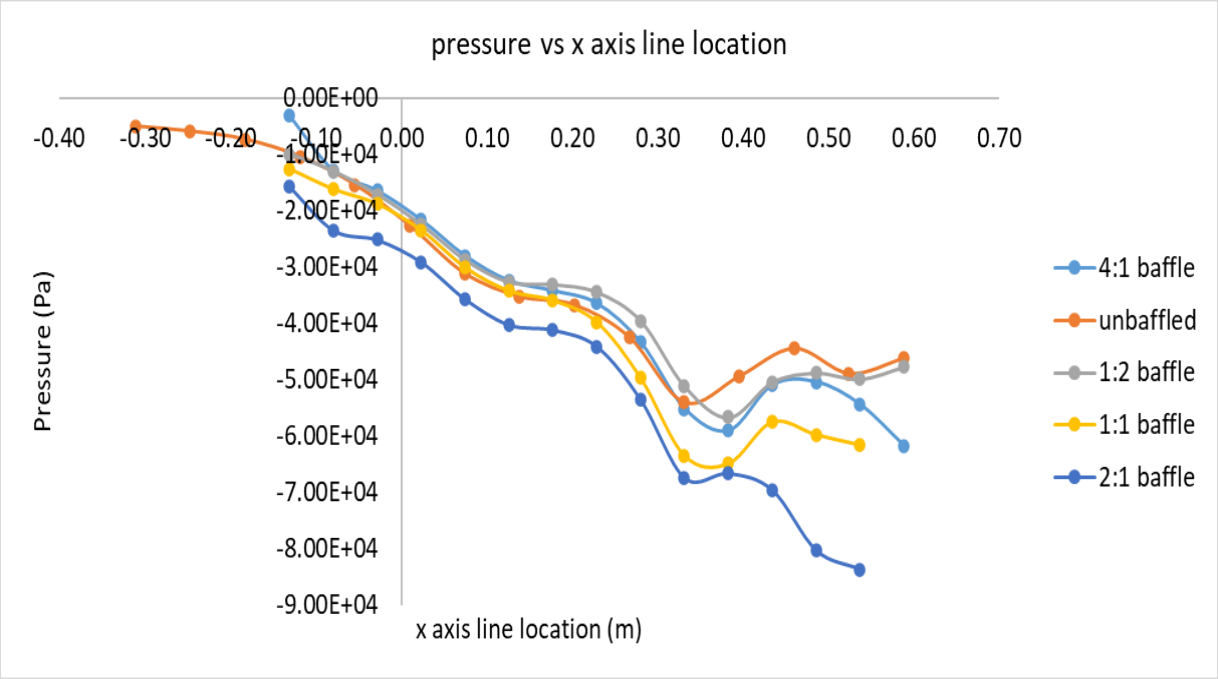

Figure 8-21 Pressure profile along the x-axis line.

The pressure located in the horizontal line location at the x axis line location within the clearance region displays a constant decrease. This means that we can expect there to be a high velocity for the moving fluid within the region in general. The pressure dip is greatest for the 2: 1 baffle further cementing its suitability among the considered baffle configurations.

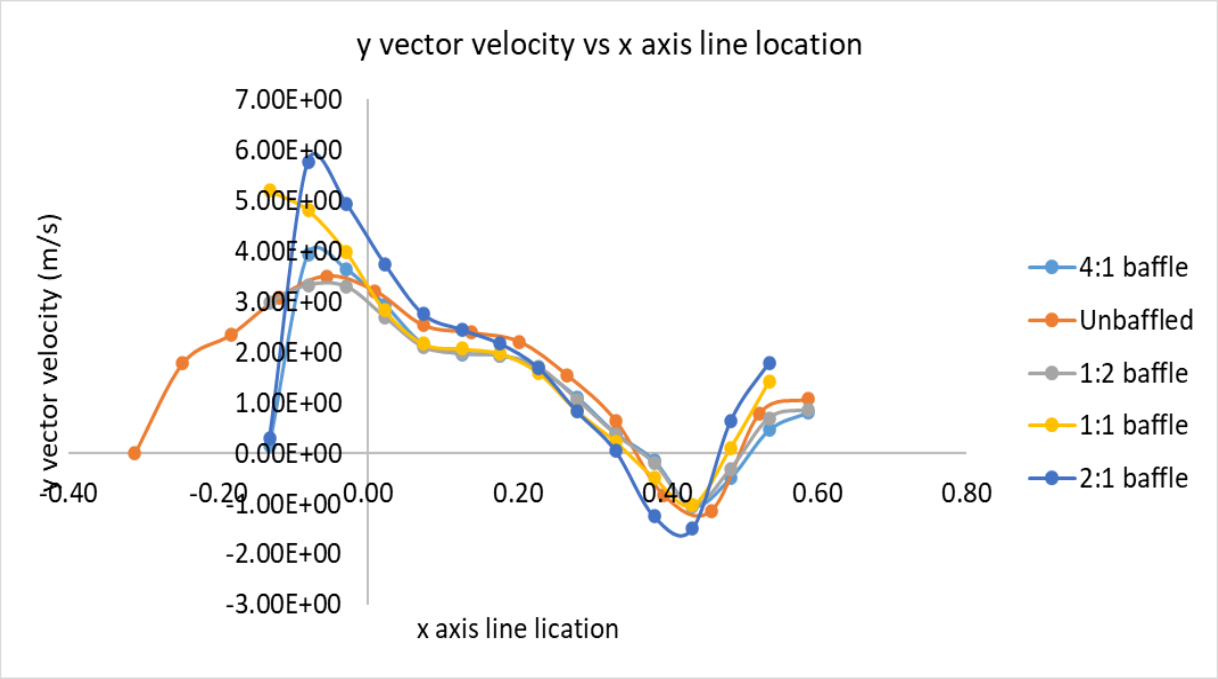

Figure 8-22 y vector velocity profile along the x axis line location.

At the location below the impeller (x axis line location) the baffle designs all produce both negative and positive y vector velocity values. This is an indicator of substantial mixing as it predicts that a lot of perturbation is being reported by the system at this location. However, from the data, the 2:1 baffle has the largest y vector maximum of $5.78\ m/s$. It also has the lowest observed minimum of $-1.5\ m/s$. This indicates that the 2:1 baffle produces the best mixing within the region below the impeller.

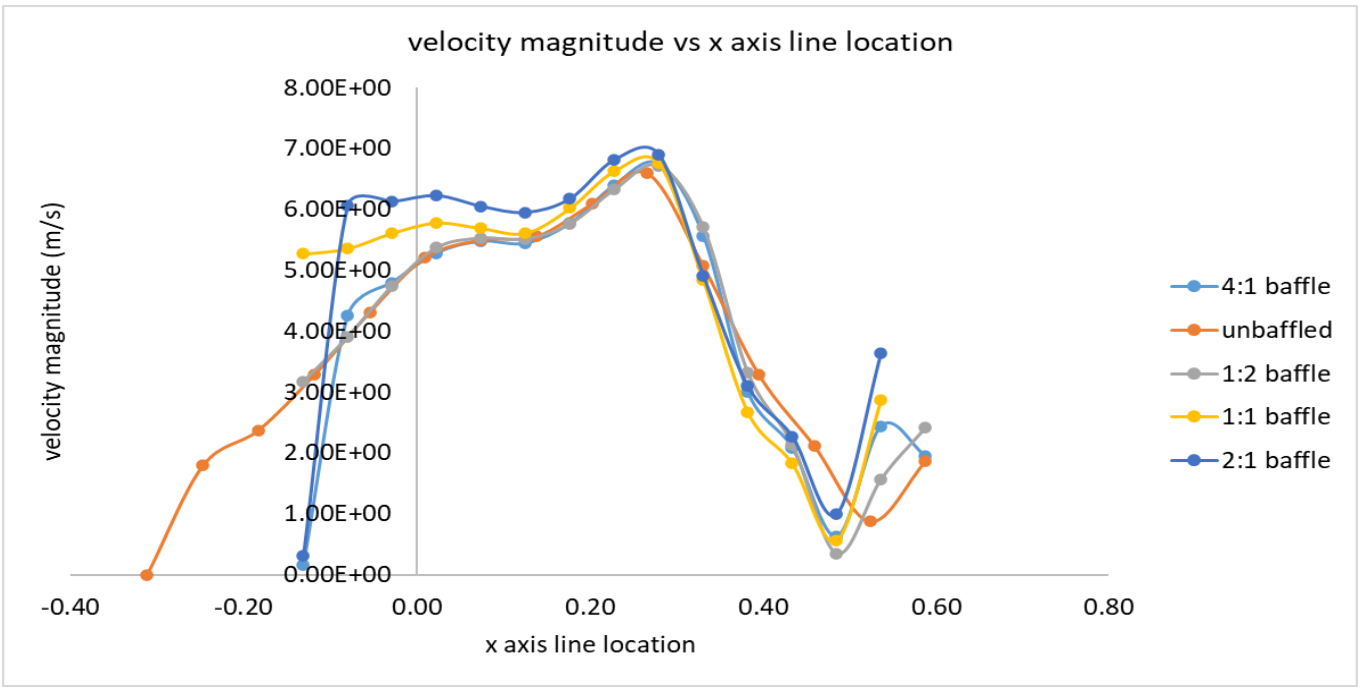

Figure 8-23 velocity profile along the x axis line location.

Similar to the y-vector velocity analysis provided prior, the 2:1 baffle produces a large velocity magnitude within the fluid (water). The maximum fluid velocity magnitude was found to be $6.91\ \mathrm{m/s}$ for the 2:1 baffle.

From this data, it was concluded that the 2:1 baffle configuration is the most suitable of the 4 baffle concepts. Moving forward, this baffle configuration will be referred to as the standard baffle setup for ease of discussion. Effect of baffle shape on fluid flow

8.9 Effect of baffle shape on fluid flow

This section provides an analysis of the effect of baffle shape on the fluid flow within an agitated stirred tank reactor. This is done by observing overlapping pressure and velocity profiles for different baffle shapes. For this study, three baffle designs were considered. At a baseline, the baffle thickness (displacement distance from the tank wall) is kept constant for each baffle shape while having each baffle occupy the same volume of the stirred tank. As concluded in the previous section, the standard baffle ($2{:}\,1$ configuration) is the most suitable baffle. Therefore, the objective is to construct baffle shapes with the same baffle thickness as that of the standard baffle.

The baffle shapes were modelled from the Gaussian error function and a normal distribution function.

Normal distribution function:

$$f(x) = \frac{1}{\sigma\sqrt{2\pi}} e^{-\frac{1}{2}\left(\frac{x-\mu}{\sigma}\right)^2} \tag{8.1}$$

with $\sigma = 0.4723$ and $\mu = 0$.

The error function baffle was modelled on the parameter $36.1\mathrm{erf}\,(z)$.

The standard error function is given as:

$$\mathrm{erf}(z) = \frac{2}{\sqrt{\pi}} \int_0^z e^{-t^2} \partial t \tag{8.2}$$

For this baffle model, the lower limit is 0.0374, upper limit is 0.374 with intervals of 0.0374.

In addition to the standard baffle design, the normal distribution function and error function baffles were modelled using the CAD software and transferred into Ansys DesignModeller. The resultant geometries can be viewed in Figure 8-24 – Figure 8-26.

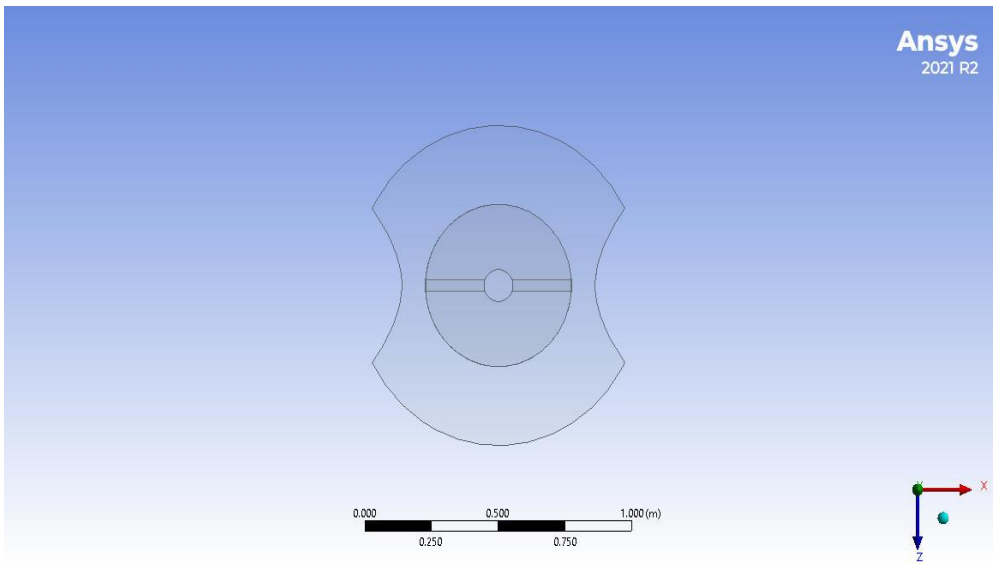

Figure 8-24 error function baffle configuration.

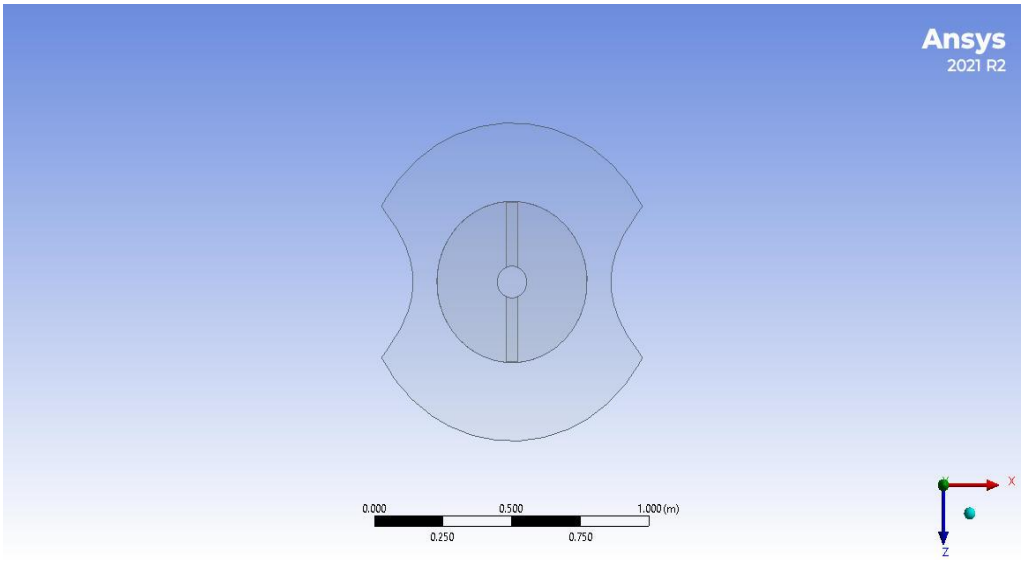

Figure 8-25 normal distribution function baffle configuration.

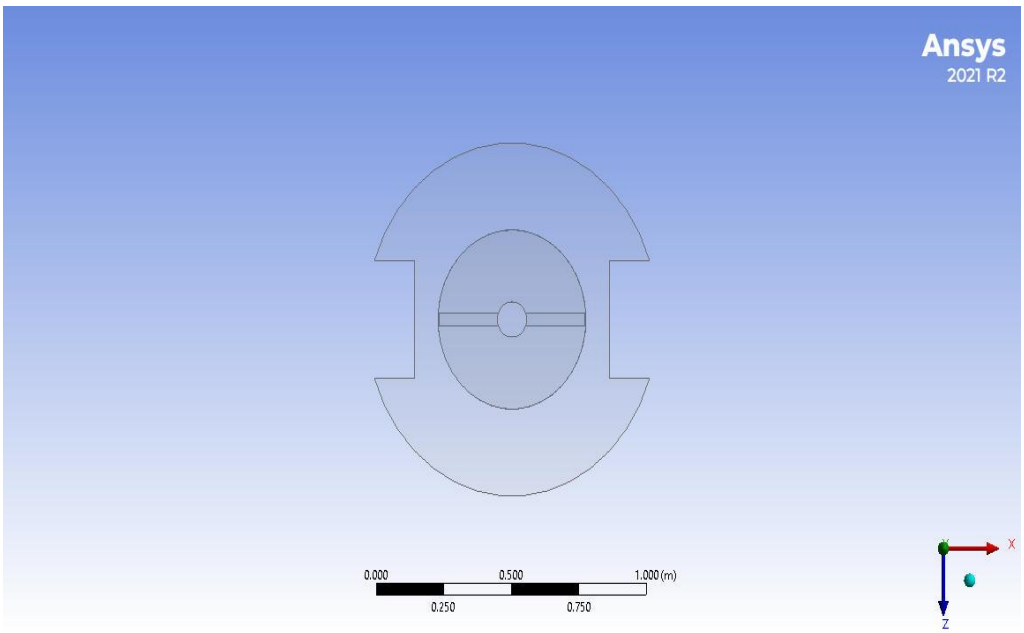

Figure 8-26 Standard baffle configuration.

8.9.1 Data analysis

Pressure profile for the location below the impeller is shown in Figure 8-27.

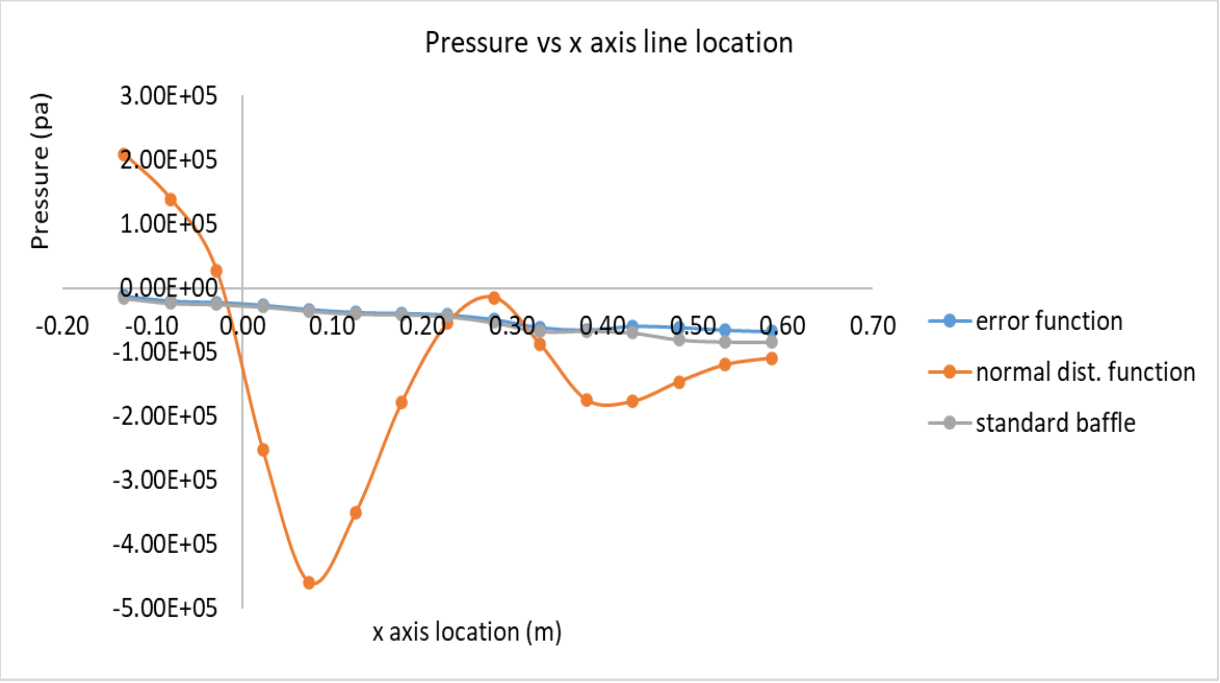

Figure 8-27 pressure profile at the x-axis line location.

The pressure profile in the defined location at the x – axis line location within the clearance region shows significant minima and maxima for the flow generated with the normal distribution baffle configuration with a minimum of −458357 Pa and a maximum of 208217.1 Pa. This is notable as it shows that there are significant velocity changes for the fluid flow within this region and is thus

indicative of better mixing when compared to that of the error function and the standard baffle configurations. The average pressure at the x axis location for the normal distribution function baffle, error function and standard baffle configurations were -115047 Pa, $-52345.8\,Pa$, and -57675.5 Pa. The lower pressure average for the normal baffle configuration further confirms the higher agitation produced by the normal distribution baffle configuration. From the average pressure values, standard baffle configuration is shown to be producing greater agitation than the error function baffle configuration.

Following on from this, horizontal planes were constructed at the x axis line location and contours were made to help visually represent the pressure distribution at this location.

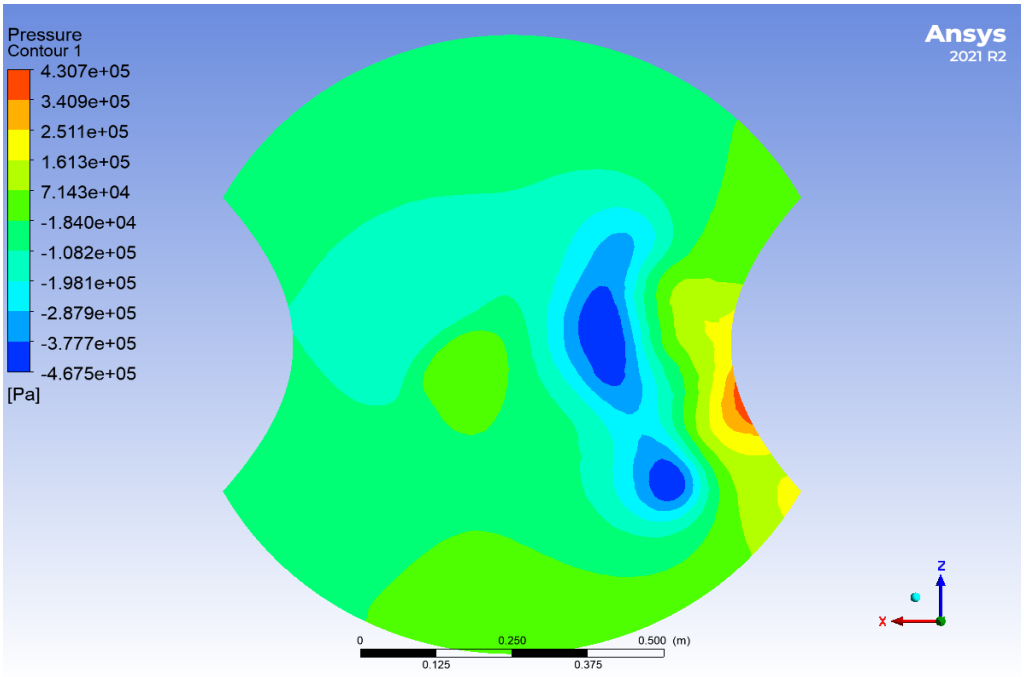

Figure 8-28 Normal distribution baffle mixing tank pressure contour at the X-axis location.

The normal distribution contour at this location displays the presence of very high and very low pressure zones indicative of the mixing taking place.

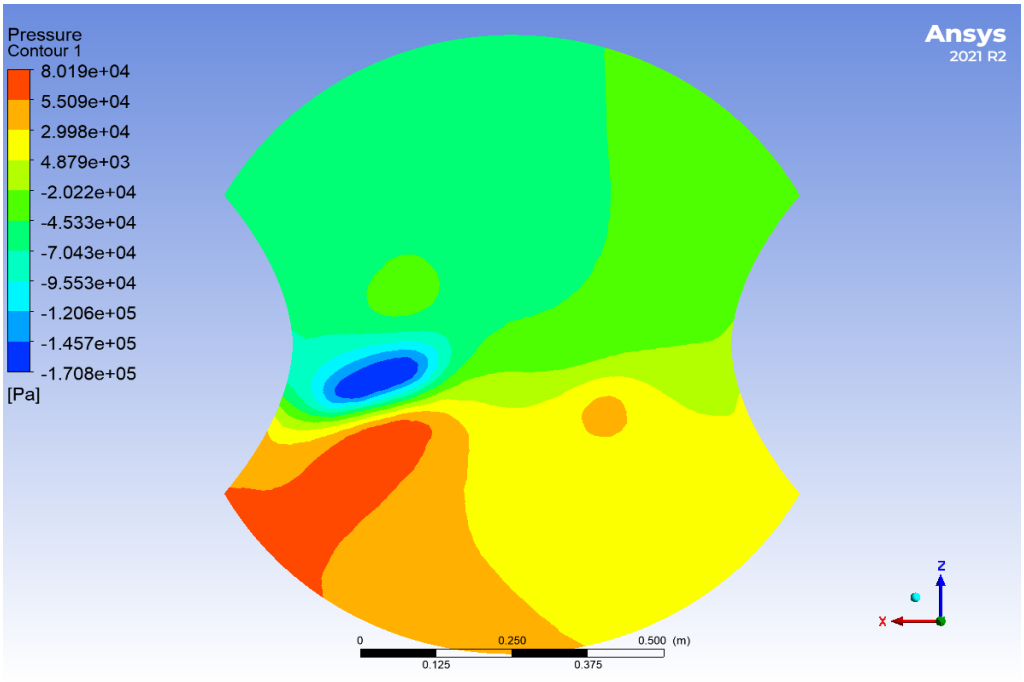

Figure 8-29 Error function baffle mixing tank pressure contour at the X-axis location.

The error function contour helps to visually represent the high and low pressures located along the plane at the x axis line location. This is indicative of intensive mixing occurring at this location.

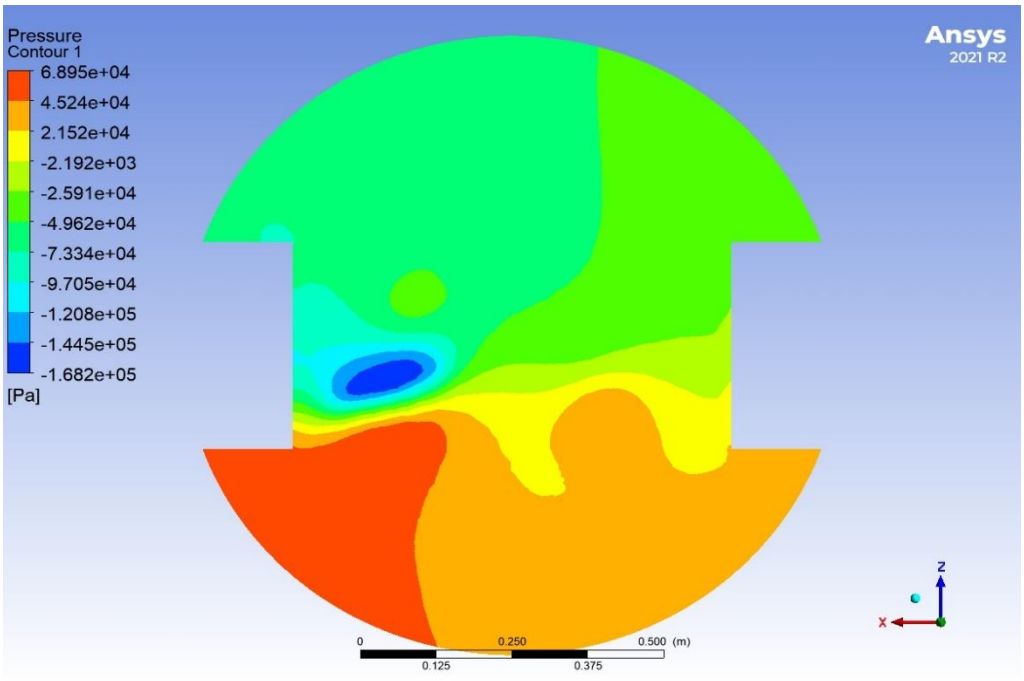

Figure 8-30 Standard baffle mixing tank pressure contour X-axis line location.

The contour in Figure 8-30 above is a visual representation of the pressure at the plane located at the x axis line location. The difference in pressures across different zones along the plane indicates fluid motion from the high pressure zones to the low pressure zones and thus mixing is occurring.

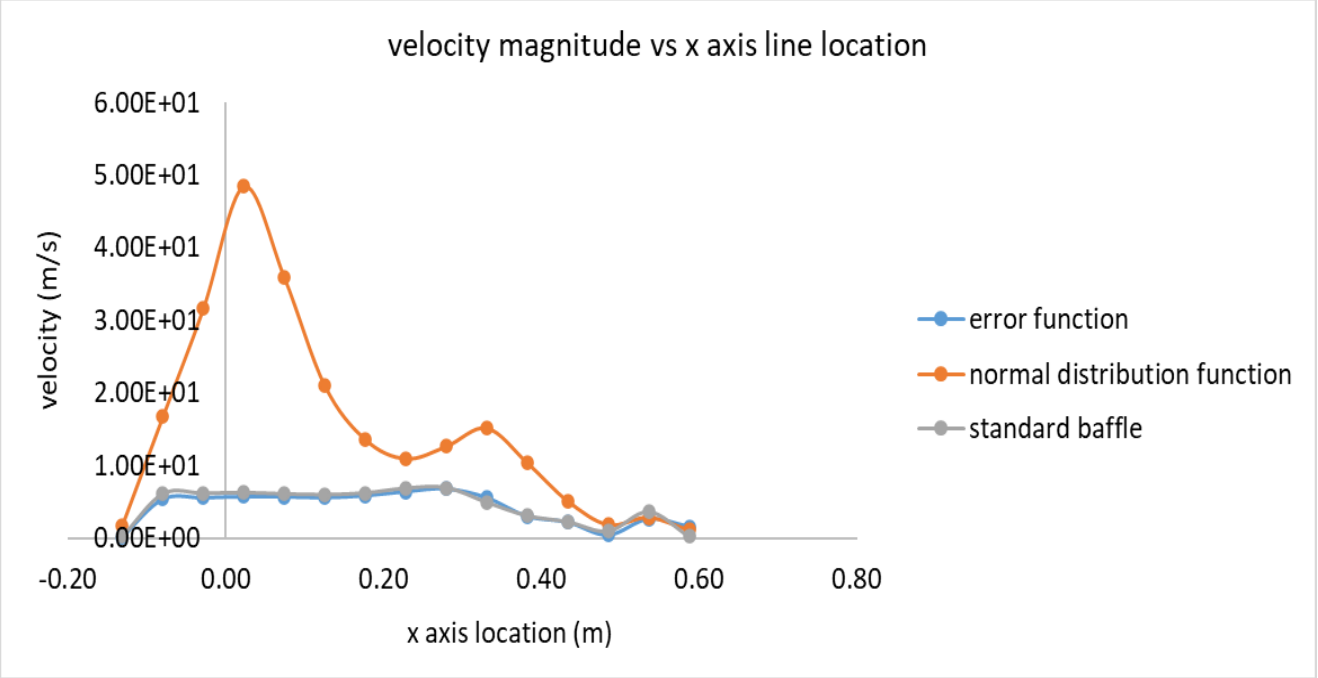

Figure 8-31 Velocity magnitude profile within the clearance region.

The velocity magnitude generated by the normal distribution baffle displays a substantially higher maximum velocity magnitude of 48.48 m/s when compared to 6.91 m/s for the standard baffle and 6.75 m/s for the error function baffle. The average velocity magnitude of the normal, error function and standard baffle configurations are 17.4568 m/s, 4.89728 m/s and 4.72896 m/s respectively. This implies that the normal distribution function baffle configuration results in the greatest agitation levels at the x axis line location. The average velocity values for the error function and standard baffle configurations are similar in value however the error function baffle configuration has a slightly higher average velocity value. This would indicate better agitation than that of the standard baffle at this region. This contradicts the pressure profile data. However, as this is a direct velocity comparison, it is reasonable to conclude that the error function baffle produces better mixing at the x axis line location.

Planes were generated at the x axis line location within each mixing tank and velocity contours were extracted. This was done to provide a visual representation of the fluid velocity within this location.

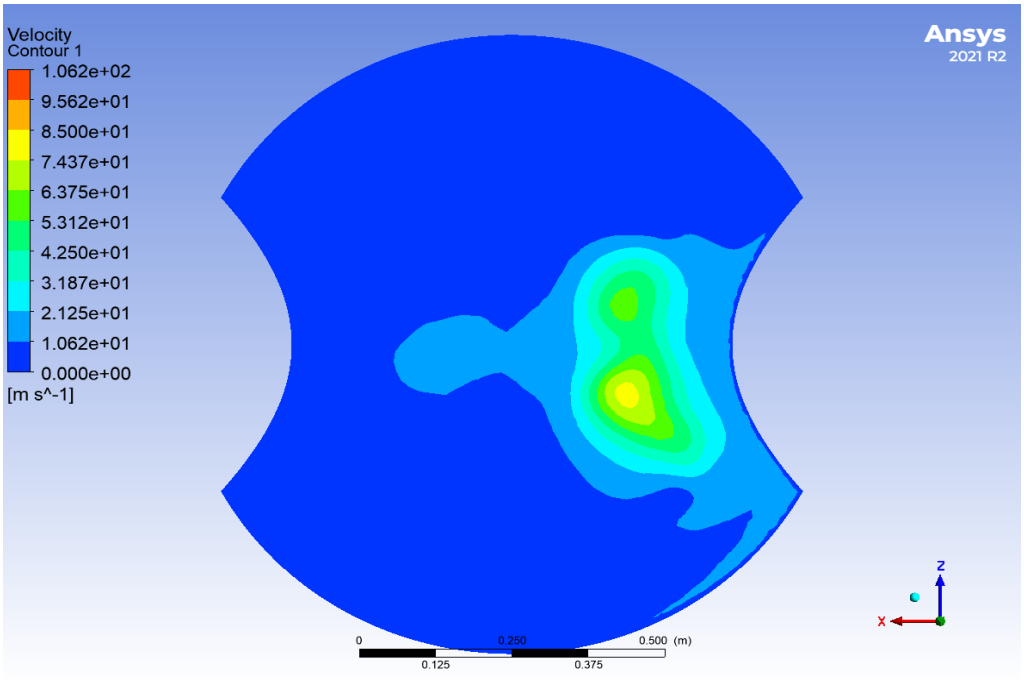

Figure 8-32 normal distribution baffle velocity contour at the X-axis line location.

The velocity contour displays a region of very high velocity magnitude followed with progressively decreasing velocity magnitudes. This is consistent with the observations made in the velocity profile displayed in Figure 8-31. However, there is overall a high velocity magnitude in this region.

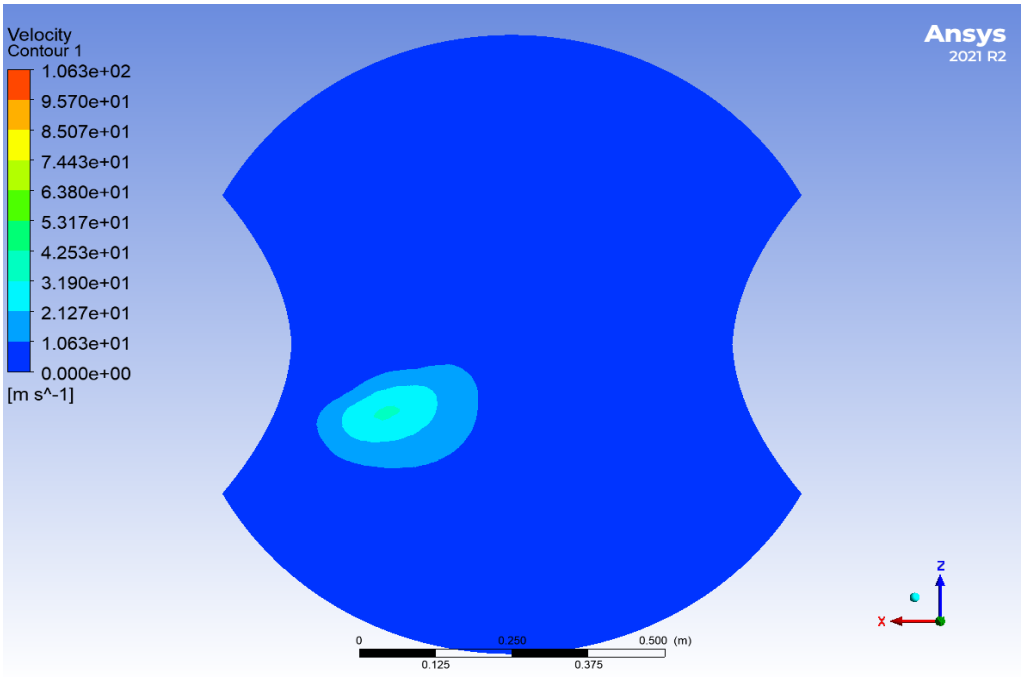

Figure 8-33 Error function baffle mixing tank velocity contour at the X-axis line location.

Like the velocity magnitude contour of the normal distribution baffle configuration, the error function baffle configuration displays a region of high velocity magnitude. However, the region of highest velocity is not as large as that of the normal distribution baffle configuration.

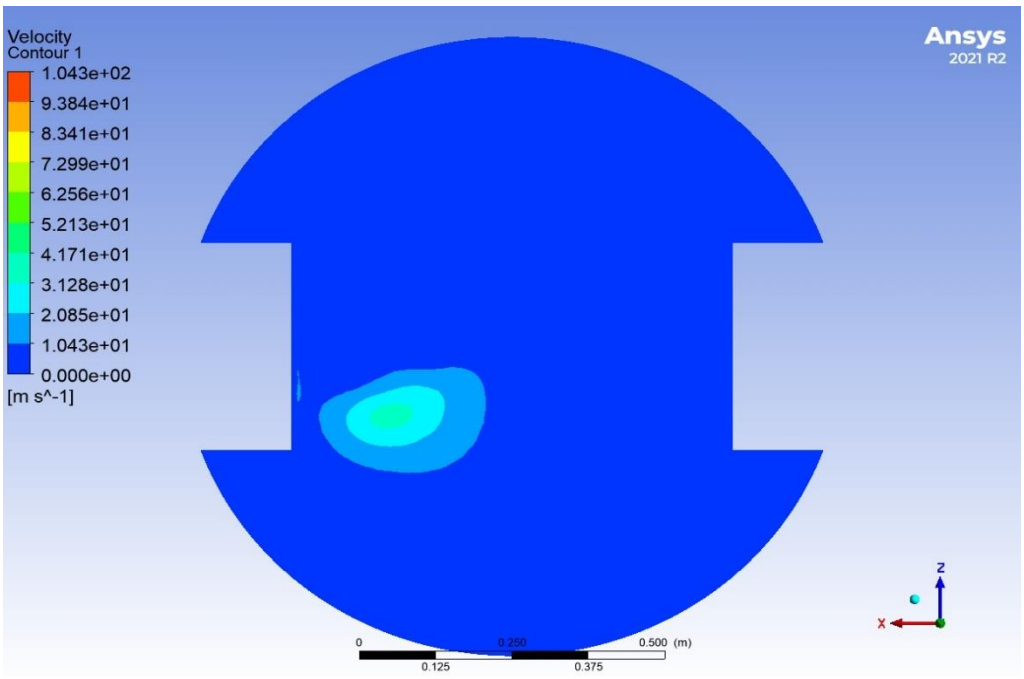

Figure 8-34 Standard baffle mixing tank velocity contour at the X-axis line location.

Like the error function baffle configuration contour, the high velocity region is smaller than that of the normal distribution function baffle configuration.

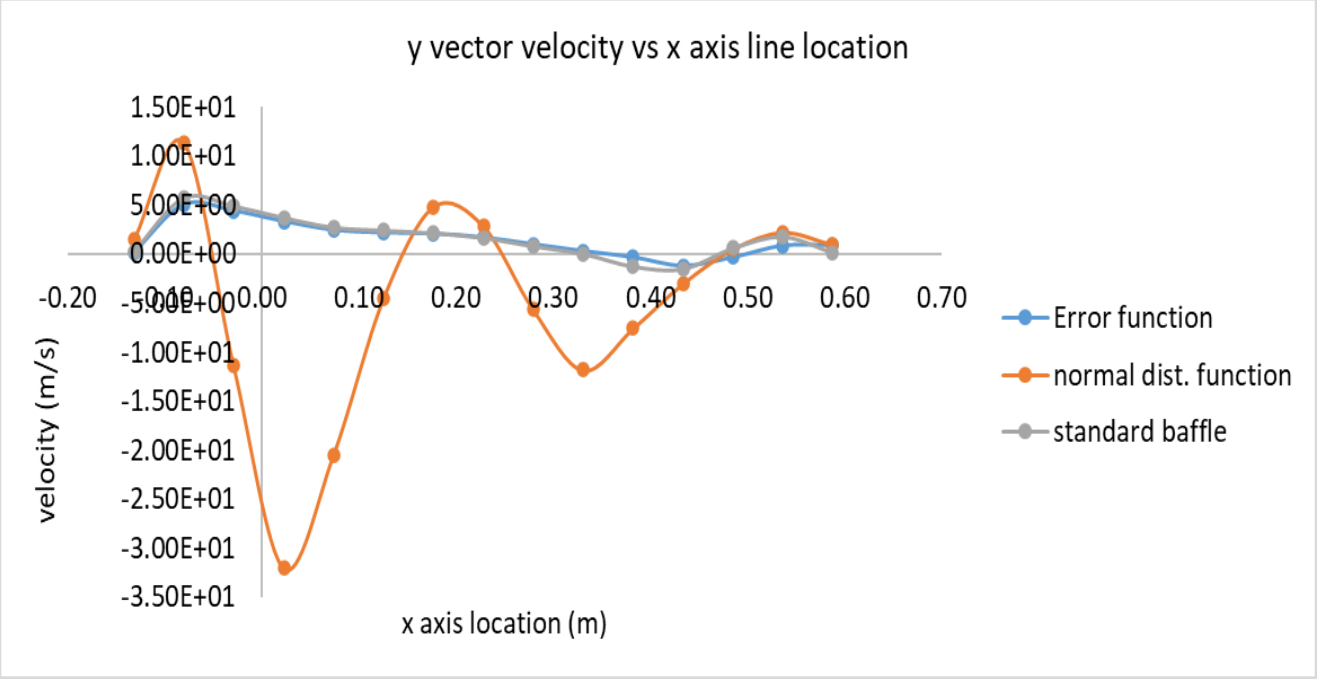

Figure 8-35 y vector velocity profile within at the x axis line location.

The y vector velocity profile for each of the three baffle configurations has negative and positive velocity values with the normal distribution function design producing the greatest maxima and minima with regards to y vector velocity values. The maximum y vector velocity was found to be $11.3702\ \mathrm{m/s}$ while the minimum for the normal distribution design was determined to be $-31.98\ \mathrm{m/s}$. When compared to the error function baffle and the standard baffle configuration at maxima of $5.05\ \mathrm{m/s}$ and $5.77\ \mathrm{m/s}$ respectively and minima of $-1.19\ \mathrm{m/s}$ and $-1.5\ \mathrm{m/s}$ respectively.

In addition to indicating direction change of fluid flow within this region for the three systems, this is a signal of better mixing within the normal distribution baffle configuration than that of the standard and error baffled stirred tanks.

Horizontal planes were generated at the x axis line location. After which, contours were created to visually represent the y velocity profiles along this plane.

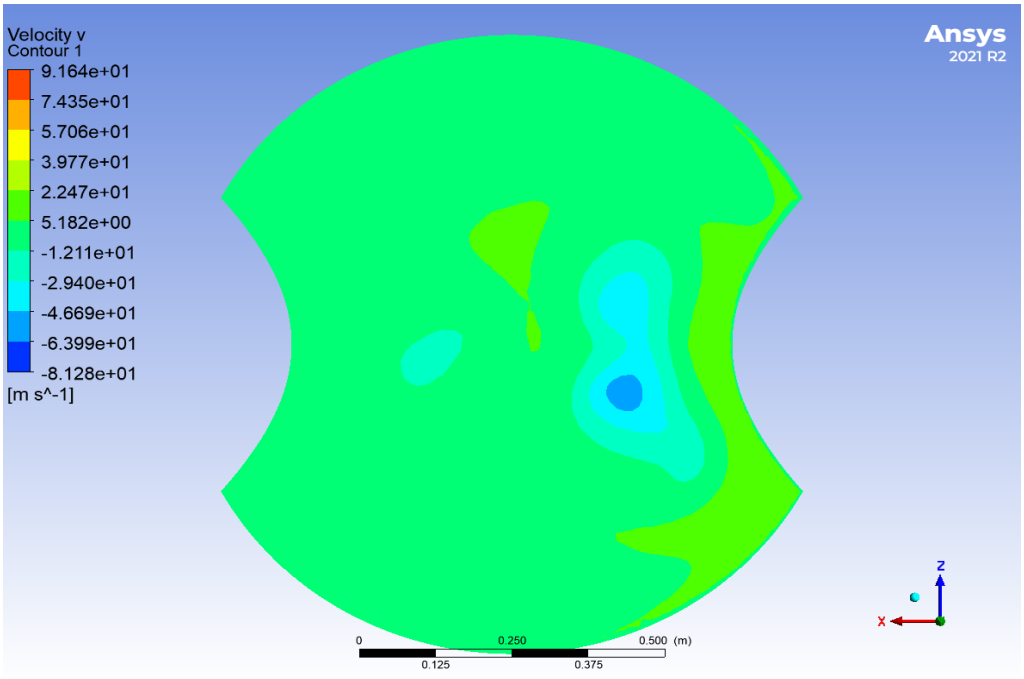

Figure 8-36 Normal distribution function baffle stirred tank Y vector velocity at the x-axis line location.

The y vector velocity contour at the x axis line location plane of the normal distribution baffle configuration mixing tank shows the large change in direction with the presence of large negative and positive y vector velocity values.

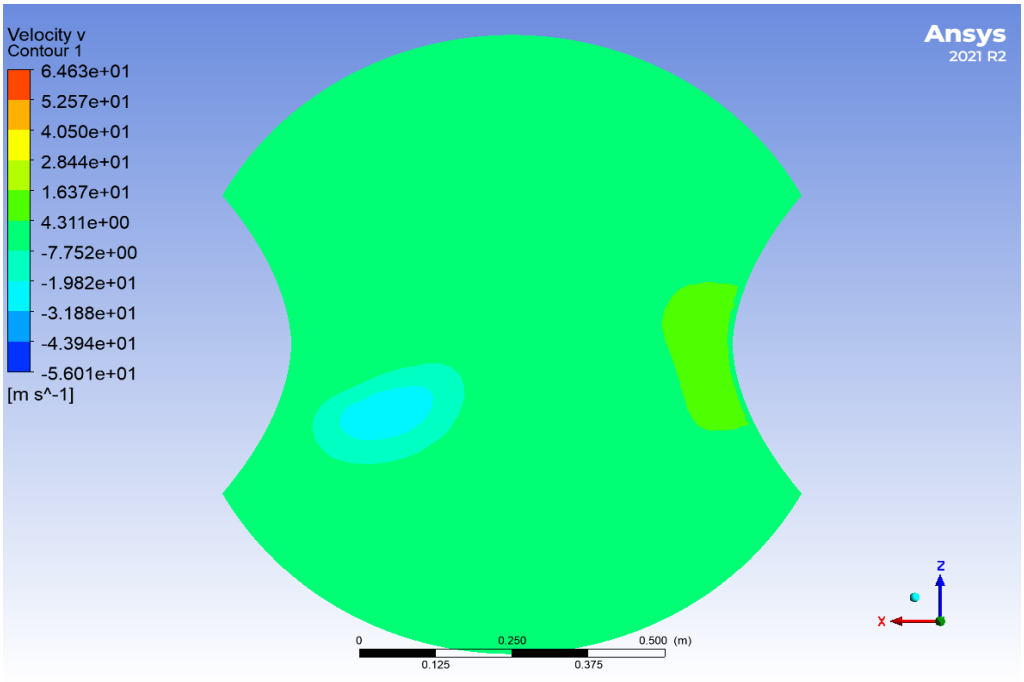

Figure 8-37 Error function baffle stirred tank Y vector velocity at the X-axis line location.

The contour displays positive and negative y-vector velocity values indicating fluid direction change and by extension, good agitation.

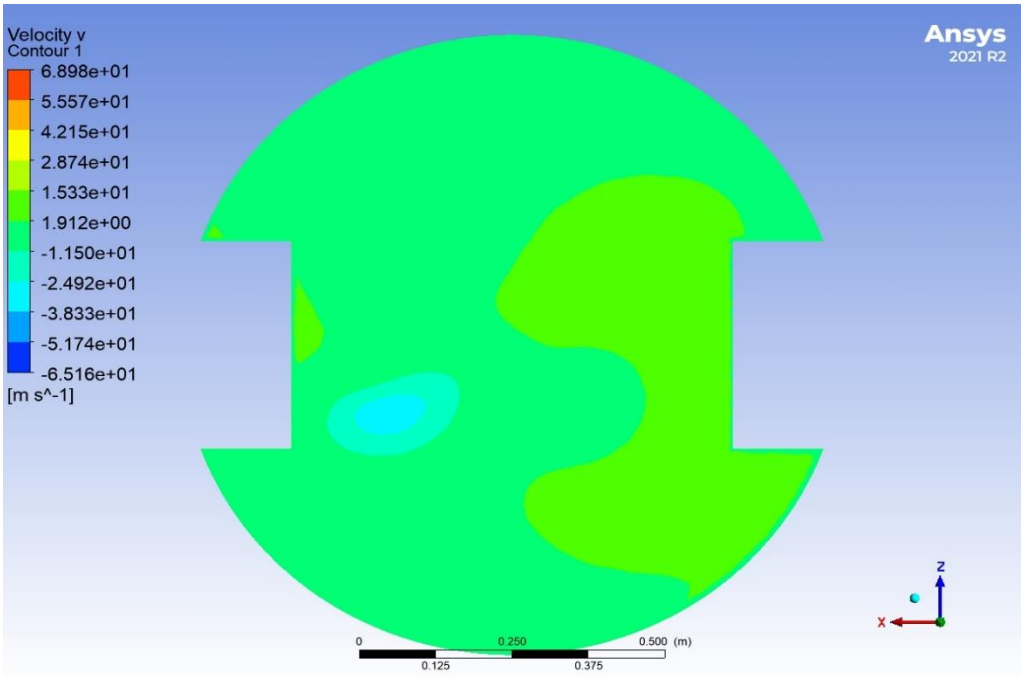

Figure 8-38 Standard baffle stirred tank Y vector velocity at the X-axis line location.

The y vector velocity contour in Figure 8-38 shows that there is direction change in fluid flow due to the presence of both positive and negative y vector velocity values.

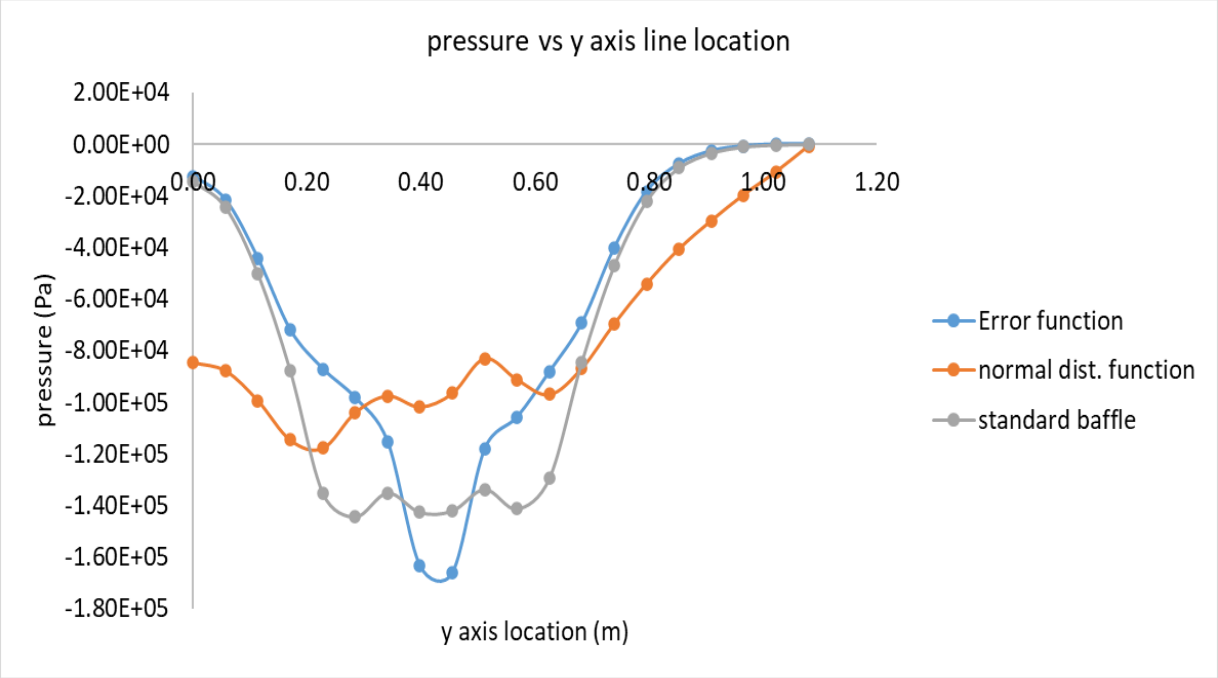

Figure 8-39 pressure profile along the y axis line location.

This location is useful in determining the consistency of mixing the further one gets from the impeller. The most ideal situation would be for there to be a more consistent pressure distribution as opposed to a large pressure dip within the impeller region. When observing Figure 8-39 above, the pressure profile for the error function baffle configuration shows a substantial drop in pressure within the region dominated by the impeller. The same can be observed for the standard baffle with the pressure change being located mainly within the impeller region. However, the normal distribution baffle displays a relatively consistent pressure distribution further away from the impeller region. This is indicative of a better flow distribution attributed to the normal distribution baffle configuration. A similar pattern can be observed for the standard baffle; however, it produces a narrower flattening of the pressure curve.

The average pressure of the normal distribution function baffle configuration mixing tank at the vertical line location is -75699.8 Pa. The average pressure at the y axis location for the error baffle configuration is -63912 Pa and at the standard baffle configuration is -72369.8 Pa. The lower average pressure of the normal distribution function baffle is indicative of better mixing at this location with the next best option being the standard baffle configuration.

A vertical plane was generated in CFD Postprocessing, and pressure contours extracted to visually represent the pressure profile.

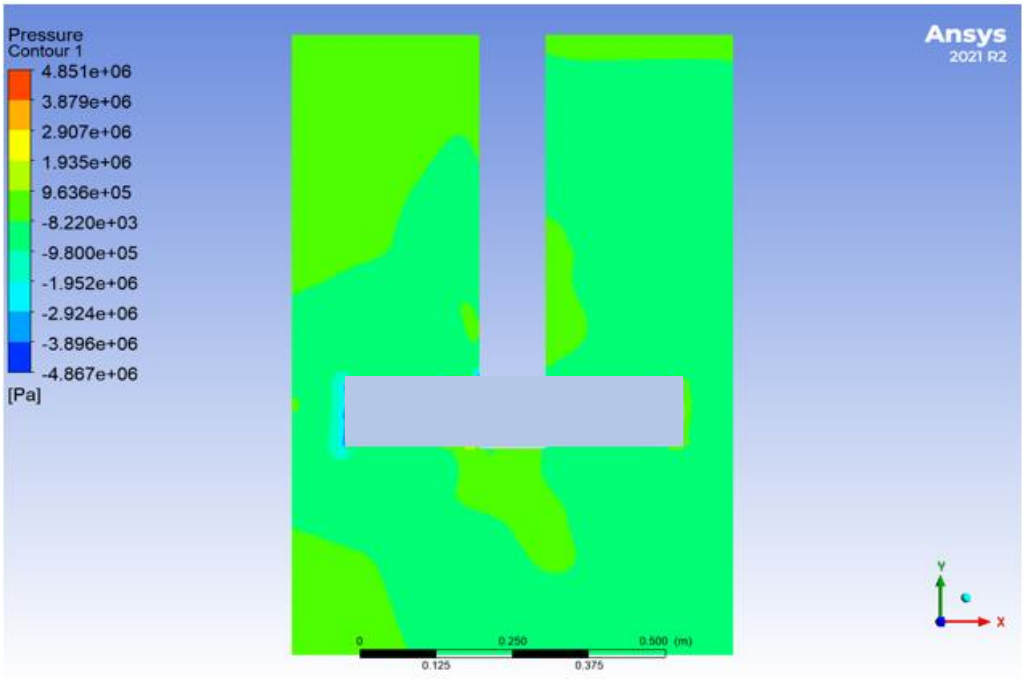

Figure 8-40 Normal distribution baffle mixing tank pressure contour.

The contour displays large negative pressure throughout the system. The largest pressure drop of approximately 9 atm is localized at the impeller zone depicting indicating a positive velocity delta and thus a region of greater mixing.

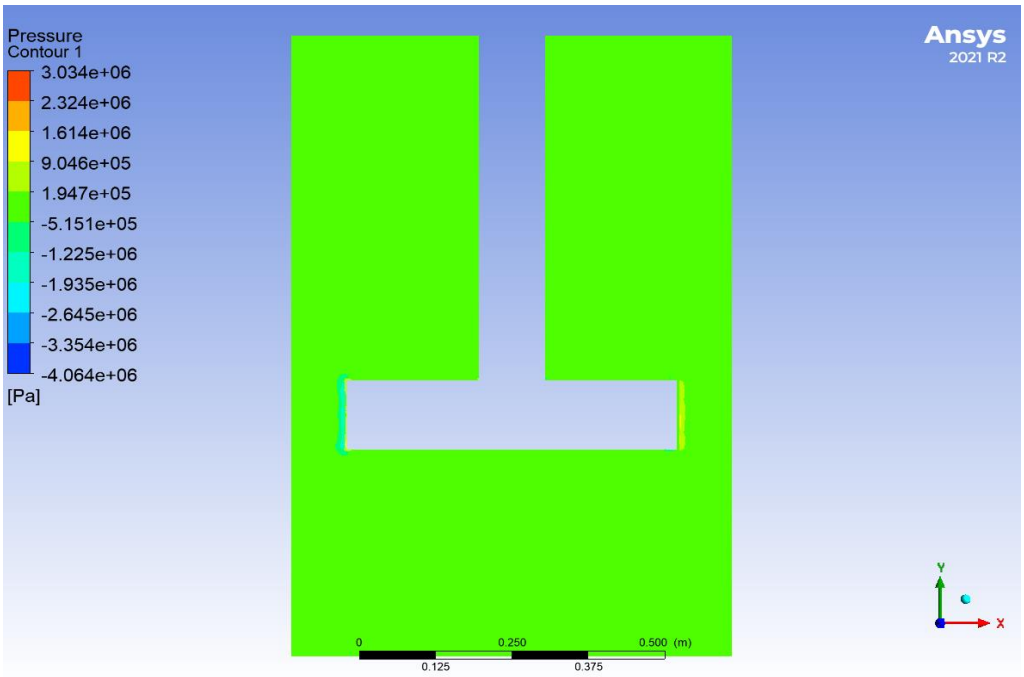

Figure 8-41 Error function baffle mixing tank pressure contour.

The pressure contour shows large negative fluid pressure within the mixing tank. This is indicative of intensive mixing in the system as it means that the fluid is moving at high velocities.

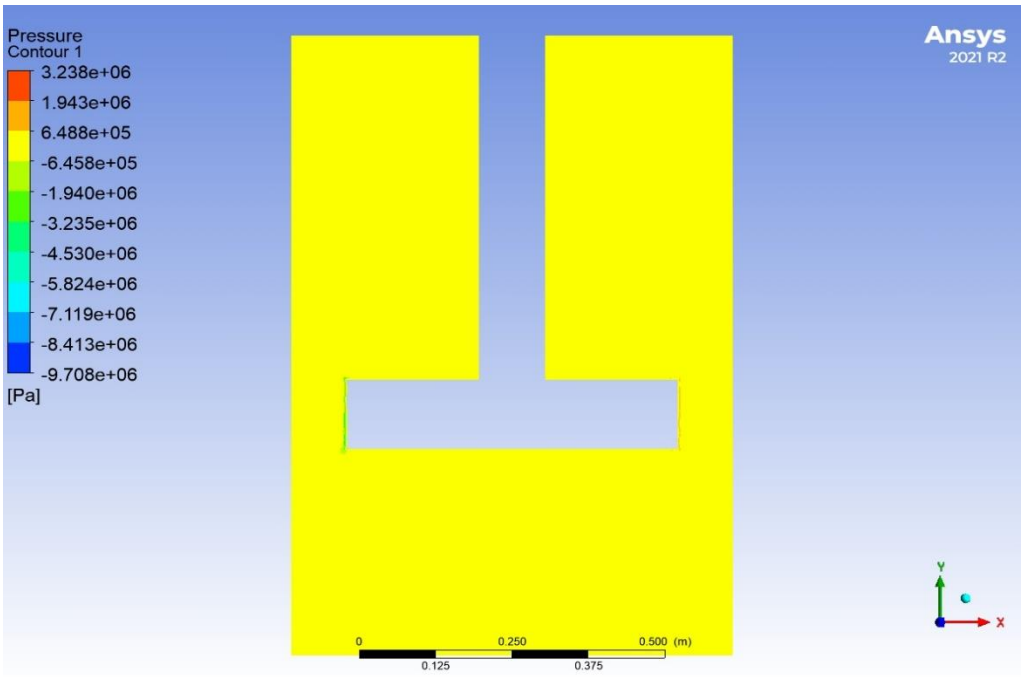

Figure 8-42 Standard baffle mixing tank pressure contour

The above contour displays the high negative pressure along the centre of the stirred tank. This is an indicator of fluid motion in this region.

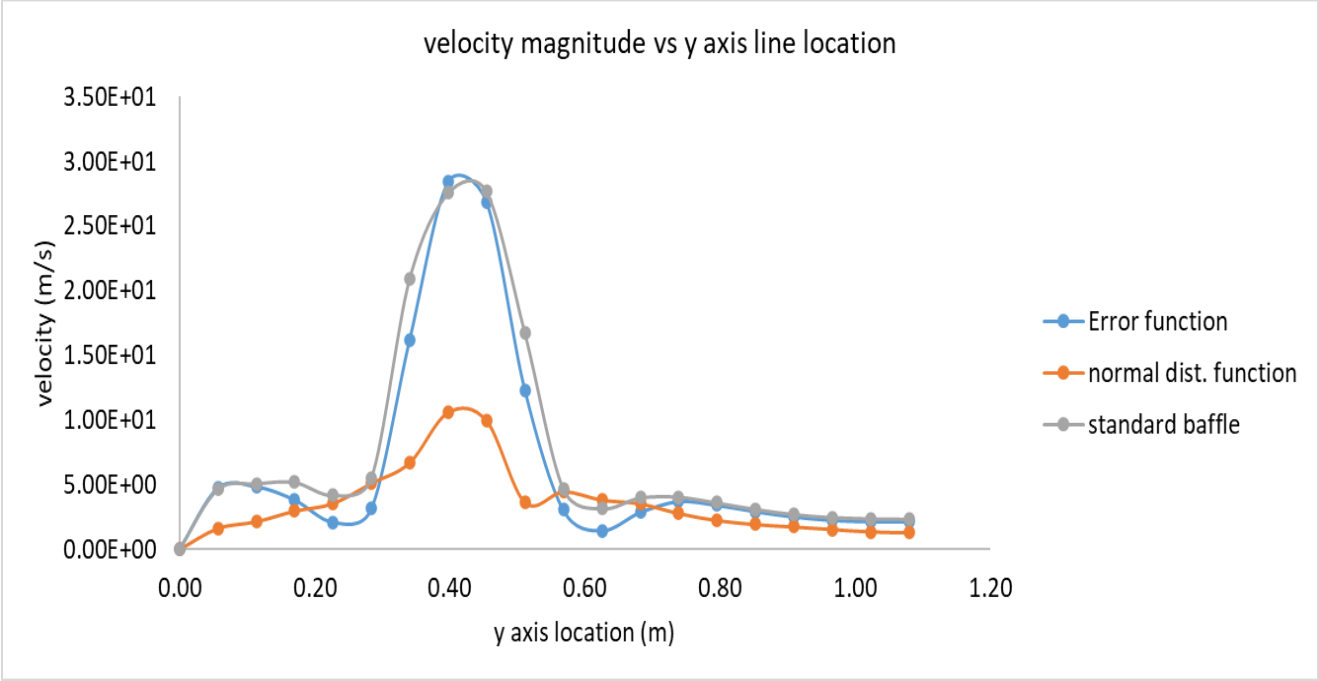

Figure 8-43 Velocity profile along the vertical line.

The curve represented within Figure 8-43 shows a similar trend of velocity magnitude peaks within the impeller region. The error function and standard baffle designs are found to produce the greatest peak velocity magnitudes $2.84\ m/s$ and $2.77\ m/s$ with the normal distribution function baffle yielding a maximum velocity of $1.06\ m/s$.

To further illustrate the velocity magnitude within the stirred tank reactors, contours were generated along the height of the stirred tank reactors. These are displayed below:

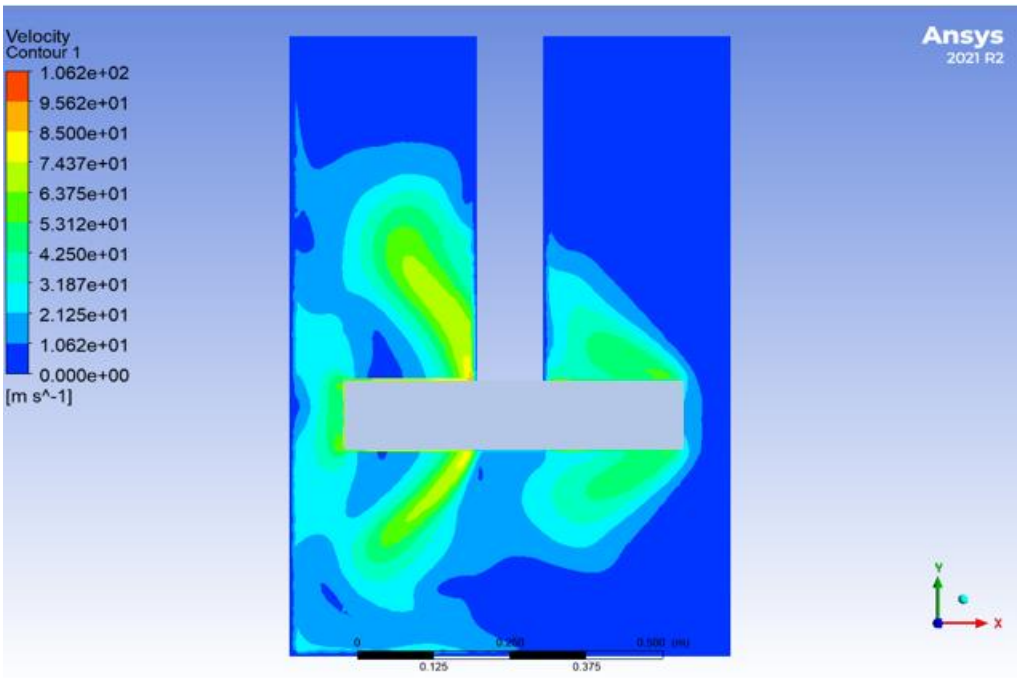

Figure 8-44 Normal distribution function baffle velocity contour.

The normal distribution function baffle velocity contour displays high velocity magnitudes throughout the plane. However, the impeller region displays the highest velocity magnitude.

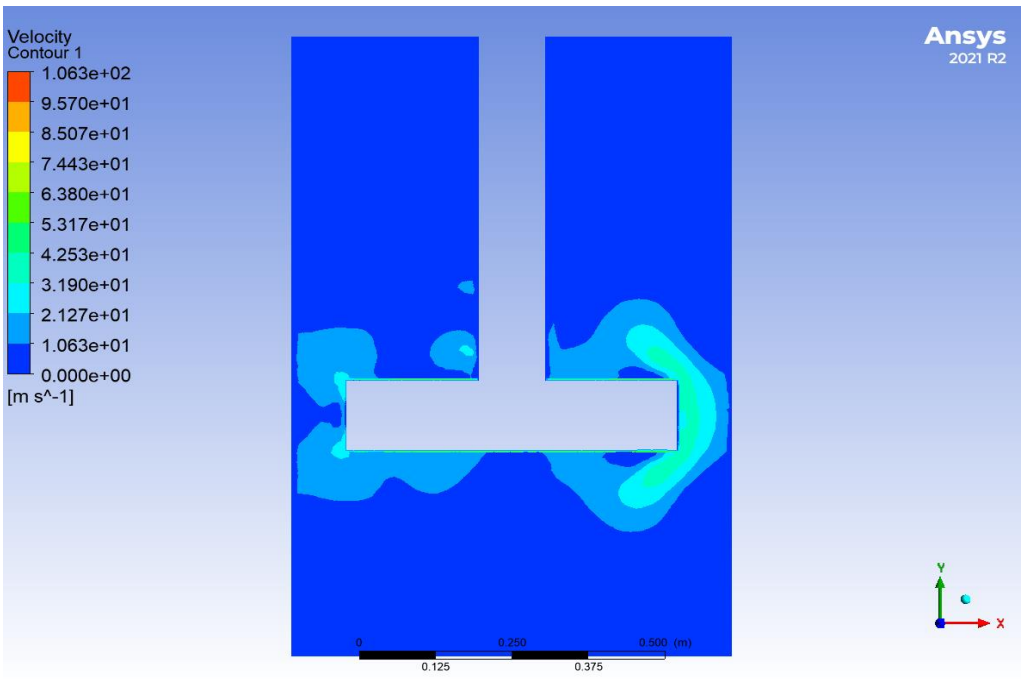

Figure 8-45 Error function baffle mixing tank velocity contour.

The baffle region displays the largest velocity magnitude. When compared to the normal distribution configuration, the error function baffle configuration velocity contour displays a lower velocity magnitude along the vertical plane.

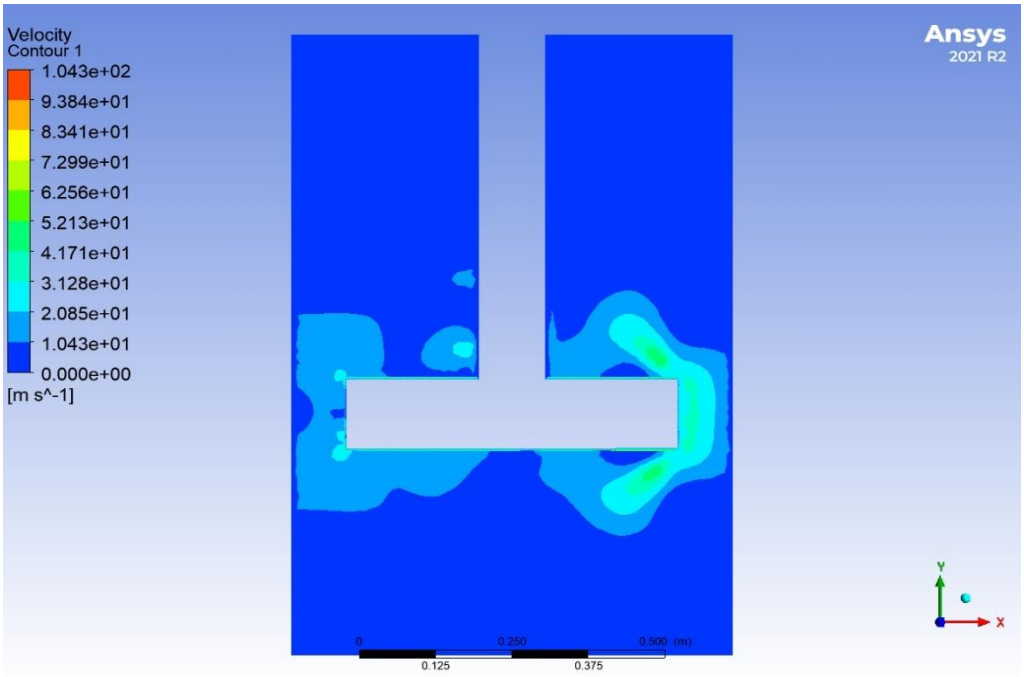

Figure 8-46 Standard baffle mixing tank velocity contour.

The standard baffle contour displays high velocity magnitude at the impeller region. However, the rest of the mixing tank displays a lower velocity magnitude overall than the in the normal distribution baffle contour in Figure 8-44.

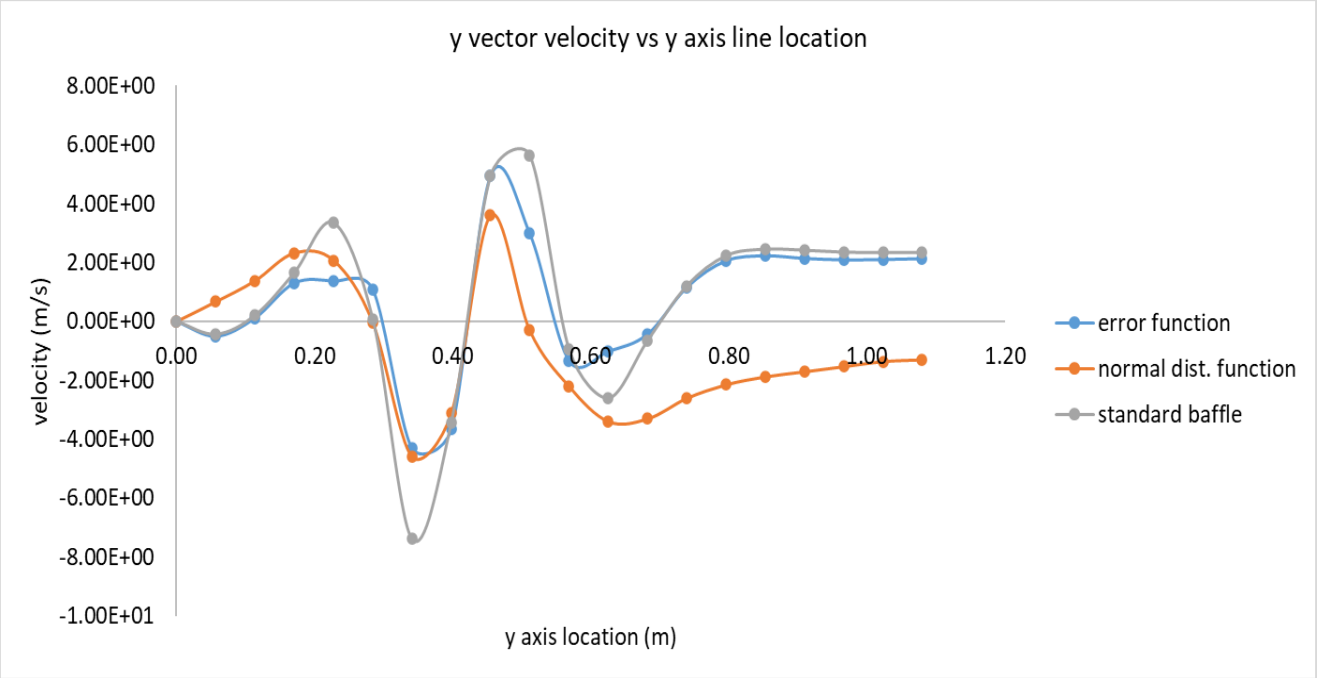

Figure 8-47 y vector velocity against x axis location.

Figure 8-47 displays negative and positive y vector velocity values. Thus, there is a high level of fluid agitation resulting in direction change within this location. This indicates good mixing at this location.

To physically represent y vector velocities in the middle of the mixing tank, vertical contours were generated at the tank centre and displayed below.

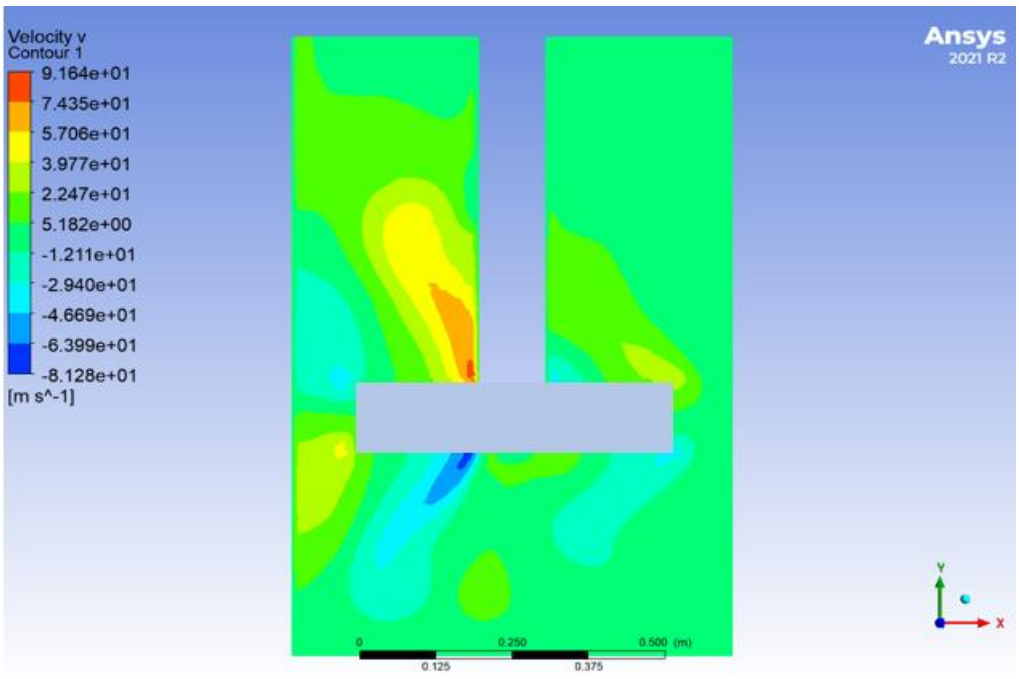

Figure 8-48 Normal distribution function baffle mixing tank Y vector velocity contour.

This shows the y vector velocity contour generated by the normal distribution function baffle configuration. It shows regions containing both positive and negative y vector velocity values. This is consistent with good agitation throughout the height of the mixing tank.

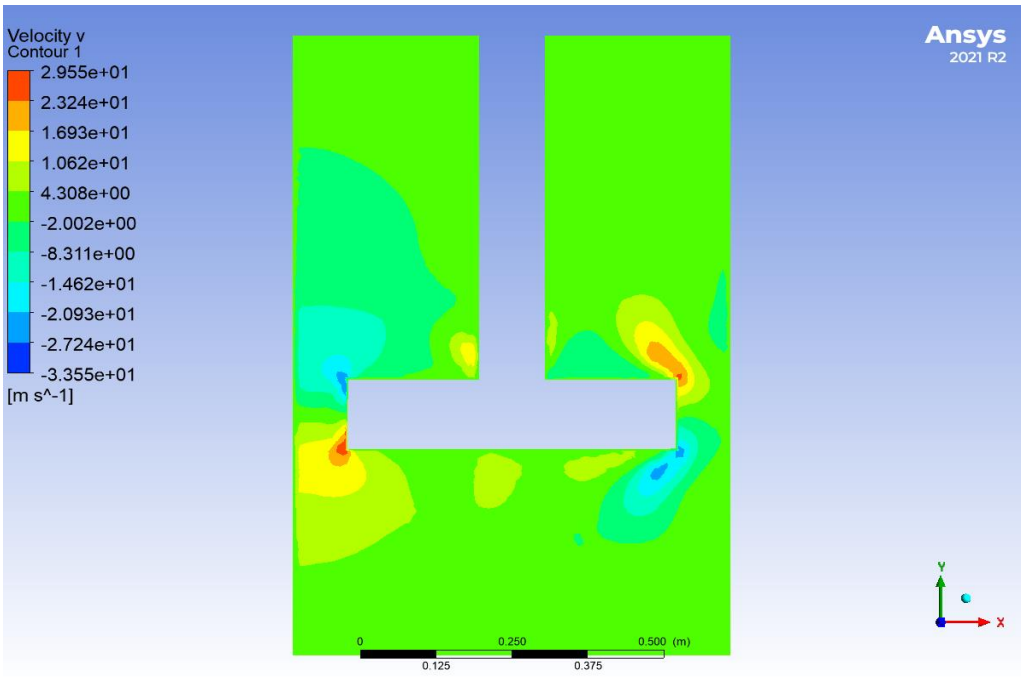

Figure 8-49 Error function baffle mixing tank Y vector velocity contour.

The contour displays a combination of positive and negative y vector velocity values. This indicates direction change in fluid movement and this is a contributing factor in fluid mixing.

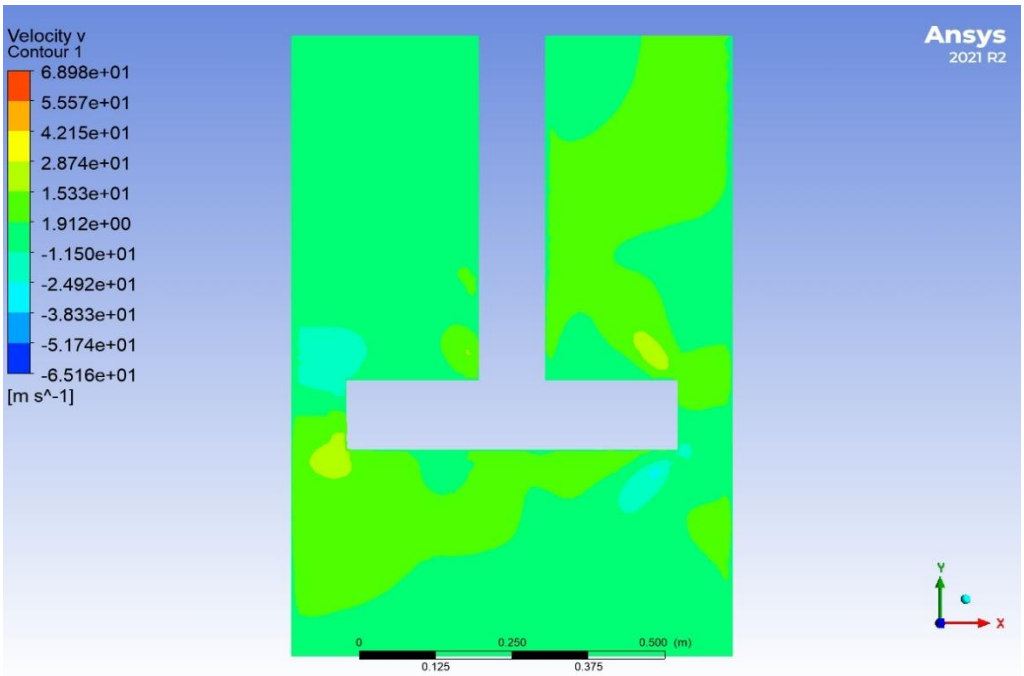

Figure 8-50 Standard baffle mixing tank Y vector velocity contour.

The y vector contour displays the presence negative and positive velocity values indicating that agitation is occurring.

From the data displayed in the pressure and velocity profiles, the normal distribution baffle is the best option for agitating the fluid (water) in the mixing tank. Thus, of the three baffle conditions, the most suitable baffle takes the form of the normal distribution curve with the standard and error function baffles producing similar profiles for velocity data. However, the pressure profiles along the x-axis line indicates that the standard baffle configuration is more suitable than the error function baffle configuration.

9 Multiphase modelling

9.1 Multiple phase models

This section of the project involves the analysis of multiphase flows within stirred tank reactors. This will consider the effect of baffle shapes on the flow dynamics within given stirred tank reactors.

To analyse multiphasic flow regimes, it is important to analyse how fluids are observed when moving through space. There are two schools of thought when it comes to observing fluid trajectories within space, Lagrangian and Eulerian.

Taking a parcel of a secondary fluid moving through a bulk fluid, the Lagrangian viewpoint supposes that a co-ordinate is placed on each parcel and any discretisation or flow analysis is performed while 'riding' on the fluid parcel. As one might surmise, this would be a very computationally expensive procedure [132, 133].

The method employed in Fluent is the Eulerian coordinate system. Within the Eulerian system, the coordinate does not move in space with the fluid. Instead, it is fixed in space and the fluid properties of each fluid parcel is studied as a function of time as it passes through these fixed spatial locations. This comes with a disadvantage in that unlike the Lagrangian formulation, the Eulerian coordinate system lacks the ability to discern material history. This is because the Eulerian system does not allow for following each individual fluid parcel as it moves through space and therefore lacks accurate historical description of the material. However, it is computationally stable and relatively inexpensive [132].

Multiphase flows are categorised by their composite materials. Namely gas-liquid or liquid-liquid flows, gas-solid flows, liquid solid flows and even the more complex three fluid flows. These can be sub-categorized. For instance, bubbly flows are a type of gas-liquid or liquid-liquid flow. The same can be said for a slug flow to describe large bubbles within the bulk fluid in a liquid-liquid or gas-liquid flow.

Table 9-1 Examples of multiphase flow regimes [134-136].

Types of multiphase flows (Two Phase)	Sub-categories
Liquid-Liquid or Gas-Liquid flows	• Slug flow • Bubbly flow • Dispersed bubble flow • Annular flow • Wedging flow • Churn Flow
Gas-Solid flows	• Fluidized beds (e.g., Fixed beds, bubbling fluidization, turbulent fluidization, and slugging fluidization)
Liquid-Solid flows	• Sediment transport • Debris flow • Hydrotransport • Slurry flow

Multiphase interactions can either be continuous-continuous (contains a distinct interphase between the two fluids) or continuous-dispersed where the dispersed phase consists of particles of fluids with

tiny diameters spread out across the continuous fluid. This dispersed phase can consist of solid particles, droplets, or gas bubbles.

This section will involve a liquid-liquid mixture of water in crude oil. Fluent provides various models for multiphase flow analysis. These are the volume of fluid model, the mixture model, and the Eulerian model. It should be noted that these models are all observed through the Eulerian co-ordinate system as described earlier.

9.1.1 VOF model

The volume of fluid model (VOF) is used when interface tracking is the main objective. The fluid interfaces must also be distinct. As such, it necessitates that the fluids are not interpenetrating. This makes it useful for observing continuous-continuous phase interactions.

This volume of fluid model does this by solving a single set of momentum equations for the entire mixture body while introducing and tracking volume fractions for each fluid throughout the entire mixture body. Consider a mixture containing fluid *p* and *q*. Fluid *q* has a volume fraction of α_q in any given cell. As a result, the volume fraction α_q is either 0 and 1 in any cell, unless it's at the interface, and is used to assign properties to the specific volume. Due to this, tracking the interface between the fluid *p* and *q* is done by solving the continuity equation for volume fraction of one of the phases thus satisfying the condition of the volume fraction only solving a single set of momentum equations for the entire body.

The physical characteristics such as ρ and μ of the mixture are also weighted according to the volume fraction within the cells.

$$x = \alpha_q x_q + (1 - \alpha_q) x_p \tag{9.1}$$

where x is the scalar variable [137].

Likewise, the continuity equation in steady state for the fluid q would be,

$$\frac{1}{\rho_q}\left[\frac{\partial}{\partial t}(\alpha_q \rho_q) + \nabla.(\alpha_q \rho_q \widetilde{U}) = S_{\alpha_q} + \sum_{p=1}^{n}(\dot{m}_{pq} - \dot{m}_{qp})\right] \tag{9.2}$$

where $\dot{m}_{pq}$ is the mass transfer from the fluid *p* to fluid *q* with $\dot{m}_{qp}$ being the mass transfer from fluid *q* to fluid *p*. $\widetilde{U}$ is the average velocity of the same phase (phase *q*) and S_{α_q} is the user defined source term.

9.1.2 Mixture model

The mixture model is a model that allows for two phases to be interpenetrating unlike the VOF multiphase model. Like the VOF model, it approaches the computation of the continuity, momentum, and energy equations for the mixture. As such it's also considered as a single fluid simulation approach.

The mass conservation equation according to the mixture model is:

$$\frac{\partial}{\partial t}(\rho_m) + \nabla . \rho_m \bar{U}_m = 0 \tag{9.3}$$

where ρ_m is the density of the mixture and $\bar{U}_m$ is the mass average velocity. The density of the mixture is calculated via the equation:

$$\rho_m = \sum_{k=1}^{n} \alpha_q \rho_q \tag{9.4}$$

where α_q is the volume fraction of phase q and ρ_q its density. The volume fraction can take any value between 0 and 1 ($0 \leq \alpha_q \leq 1$)

The mass average velocity of the mixture is:

$$\bar{U}_m = \frac{\sum_{k=1}^{n} \alpha_q \rho_q \bar{U}_q}{\rho_m} \tag{9.5}$$

The conservation of momentum is the sum of the individual momentum equations for each phase that is present in the mixture:

$$\frac{\partial}{\partial t}(\rho_m) + \nabla . \rho_m \bar{U}_m \bar{U}_m = -\nabla p + \nabla . \left(\mu_m (\nabla . \bar{U}_m + \nabla . \bar{U}^T{}_m)\right) + \rho_m g + F + \nabla . \left(\sum_{k=1}^{n} \alpha_q \rho_q \bar{U}_{dr,q} \bar{U}_{dr,q} \right) \tag{9.6}$$

where F is the body force, n is the number of phases and μ_m is the viscosity of the entire mixture with $\bar{U}_{dr,q}$ being the drift velocity of the secondary phase [116].

It’s necessary to note that the mixture model and the VOF model are both simplified versions of the full Eulerian model with the mixture model being attributed to dispersed-continuous phase interactions and the VOF model being specific to continuous-continuous phase interactions. The full Eulerian model can account for both interactions making it quite useful.

9.1.3 Eulerian multiphase model.

The mixture and VOF models are modifications of the Eulerian model. What sets this model apart from the previously discussed VOF and mixture models is that it solves continuity and momentum conservation equations for each individual phase in the system i.e., it is not a single fluid approach. For the crude-water mixture examined, the Eulerian model would solve a continuity and momentum conservation equation for the crude oil and the water.

The continuity equation of the Eulerian multiphase model is similar to the standard continuity equation and presents as:

$$\frac{\partial}{\partial t}\alpha_q\rho_q + \nabla.\left(\alpha_q\rho_q U_q\right) = \sum_{p=1}^{N}\left(\dot{m}_{pq} - \dot{m}_{qp}\right) \tag{9.7}$$

This set of continuity equations is solved for every cell within the system mesh for the CFD operation. As such it is necessary to the LHS of the standard continuity equation with the volume fraction of the desired phase. As mentioned prior, in a dispersed-continuous phase the volume fraction takes any value between 1 and 0 whereas in a continuous-continuous phase interaction, the volume fraction is either 0 or 1 (except in the interphase region). The RHS of the continuity equation is modified to account for mass transfer from one phase to another. A good example of this would be in condensation and evaporation processes.

Additionally, Fluent solves a volume fraction equation for each additional phase. For instance, in the case of the crude oil and water mixture under examination, the CFD solver would solve 1 additional volume fraction equation meaning $N-1$ volume fraction equations are solved where N represents the number of phases. A separate volume fraction model being solved for each additional phase is common practise for all three models discussed. This appears as:

$$\frac{\partial}{\partial t}\alpha_q + \nabla.\alpha_q U_q = 0 \tag{9.8}$$

Along with this, the Eulerian model also solves a separate momentum equation for each phase. These phases share a common pressure field as will be shown in the momentum equation. This is useful as

it is used in the coupling of the phases in the system under examination. The momentum equation appears as shown below:

$$\underbrace{\frac{\partial}{\partial t}\alpha_q \rho_q U_q}_{momentum\ rate\ change} + \underbrace{\nabla.\left(\alpha_q \rho_q U_q U_q\right)}_{momentum\ flux} = \underbrace{-\alpha_q \nabla p}_{pressure\ gradient} + \nabla.\tau_q + \sum_{p=1}^{N} \underbrace{\left(D_{pq} + \dot{m}_{pq} U_{pq} - \dot{m}_{qp} U_{qp}\right)}_{Source\ terms}$$

(9.9)

where τ_q is the strain rate tensor for the q[th] phase. The source terms consist of mass and momentum transfer values between phases p and q and a term D_{pq}. D_{pq} is representative of each additional force acting between each phase.

$$D_{pq} = \vec{F}_D + \vec{F}_g + \vec{F}_B + \vec{F}_L + \vec{F}_V + \vec{F}_{WL}$$

(9.10)

where $\vec{F}_g$ is the gravitational force, $\vec{F}_B$ is the buoyancy force, $\vec{F}_L$ is the lift force, $\vec{F}_{WL}$ is the wall lubrication force, $\vec{F}_V$ is the virtual mass force and $\vec{F}_D$ is the drag force. The drag force $\vec{F}_D$, has the greatest impact of all the interphase transfer forces on the flow since the density ratio between the two phases, crude oil and water, is close to 1 [138].

The drag force is expressed through the drag force coefficient:

$$\vec{F}_D = \frac{C_D Re}{24}$$

(9.11)

It should be noted that Re in this case is the particle Reynolds number and is used to restrict the value of the drag coefficient C_D as displayed in the equations below:

$$C_D = \frac{24\left(1+0.15Re^{0.687}\right)}{Re} \text{ for } Re \leq 1000$$

$$C_D = 0.44 \text{ for } Re > 1000$$

(9.12)

The Reynolds number in a dispersed-continuous phase mixture is calculated based on the velocity difference between the continuous and dispersed phases, U_p and U_q. This is expressed as:

$$Re = \frac{\rho_q |U_p - U_q| d_q}{\mu_q}$$

(9.13)

where ρ_q, d_q and μ_q are the density, droplet diameter and viscosity of the primary phase [139, 140]. The presence of the droplet diameter indicates an assumption that the droplets are perfectly spherical (no deformation).

Consider, the general form of a drag force i.e., the drag equation is $\frac{1}{2}\rho U^2 A C_D$ with A being a contact area. This means that the drag force $\vec{F}_D$ can be written as:

$$\vec{F}_D = \frac{1}{2}\rho_q C_D A_p (U_p - U_q)|U_p - U_q|$$

(9.14)

Since the predominant force within the interphase forces is the drag force:

$$D_{pq} = \frac{1}{2}\rho_q C_D A_p (U_p - U_q)|U_p - U_q|$$

(9.15)

Due to Fluent calculations being done after the meshing process and computations being done at the cell centroid, the drag force is calculated under per volume specifications. Thus, the equation is slightly altered to:

$$D_{pq} = \frac{1}{2}\rho_q C_D \frac{A_p}{V} (U_p - U_q)|U_p - U_q|$$

(9.16)

This means the two unknowns that need to be specified in fluent are the interfacial A_p and the drag coefficient (C_D) and must be specified in the model setup. In the setup for the simulation the drag coefficient was set to the classical Schiller-Naumann model[141]. This is due to its robust nature as it is viable for a wide range of drag coefficients. The Schiller-Naumann drag model is described in Eq. (*9.12*) above.

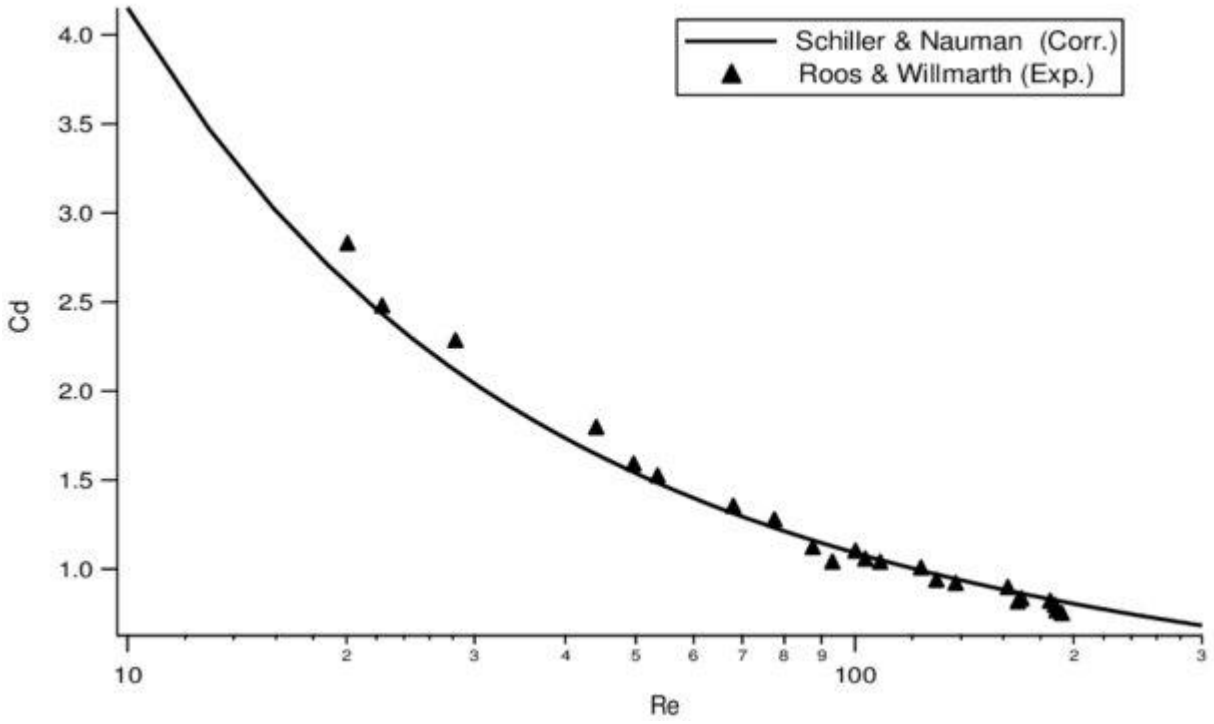

Figure 9-1 image of the schiller-naumann drag correlation [142].

The image above displays the Schiller-Naumann drag correlation as well as verification data from the experimental work done by Roos et al [143]. This was done by measuring the drag of spheres and disks set up to move rectilinearly in a glycerine-water mixture for Re values in the range of 5 to 100000.

The next unknowns to be specified are the parameters governing the interfacial area per unit cell volume or the contact area. In a CFD mesh, all cells may or may not have the same volume within the entire flow region (stirred tank reactor in this case), therefore:

$$\frac{A_p}{V} = \frac{\begin{matrix} volume\ of\ all\ the \\ spheres\ in\ the\ cell \end{matrix}}{\begin{matrix} volume\ of\ the \\ cell \end{matrix}} \times \frac{\begin{matrix} surface\ area\ of \\ all\ the\ spheres \end{matrix}}{\begin{matrix} volume\ of\ all\ the \\ spheres\ in\ the\ cell \end{matrix}}$$

$$\frac{A_p}{V} = \alpha_p \times \frac{4\pi {r_p}^2}{\frac{4}{3}\pi {r_p}^3} = \alpha_p \times \frac{\pi {d_p}^2}{\frac{\pi {d_p}^3}{6}} \tag{9.17}$$

This simplifies to:

$$\frac{A_p}{V} = \frac{6\alpha_p}{d_p}$$

(9.18)

As such your CFD solver would essentially require the provision of the diameter of the dispersed phase sphere in a dispersed-continuous phase interaction. It must be recognised that the diameter of the dispersed phase spheres might not be uniform, thus another transport equation might be used. For this project's stirred tank setup, the Sauter-Mean diameter (d_{32}) was set as the droplet diameter of the dispersed water. This is the most widely used droplet size setting. This is a useful method of predicting the droplet size diameter. It was proposed by Josef Sauter as a way of associating the particle volume to its surface area [144, 145]. In the literature it is sometimes referred to as the surface-volume mean diameter and can be represented as:

$$d_{32} = \frac{\sum_{i=1}^{n} n_i {d_i}^3}{\sum_{i=1}^{n} n_i {d_i}^2}$$

(9.19)

where n_i is the number of particulate matter and d_i is the diameter of particulate matter.

9.1.3.1 Interfacial area concentration

This is the interfacial contact area between any two phases per unit mixture volume and is an important aspect of determining how the various transport equations translate between the two phases. The distribution of dispersed phase particles can be affected by various factors such as breakage, coalescence, growth due to mass transfer, and pressure changes [116]. For a more accurate representation of all these factors, a PBM (population balance model) can be used. However, it is a very computationally expensive method. Add to this, the fact that it is at an infancy stage of its development, the decision was made not to utilize it for this simulation.

The interfacial area concentration has a transport equation that appears as:

$$\frac{\partial}{\partial t}(\rho_q \chi_p) + \nabla.(\rho_q U_q \chi_p) = \frac{1}{3}.\frac{D\rho_q}{Dt} + \frac{2}{3}.\frac{\dot{m}_q}{\alpha_q}\chi_p + \rho_q(S_{RC} + S_{WE} + S_{TI})$$

(9.20)

where χ_p is the interfacial area concentration, and S_{RC}, S_{WE} and S_{TI} are the source and sink terms from random coalitions, wake entrainment and breakage due to turbulent impacts.

There are three factors that can affect the size of dispersed particles within a multiphase system, and these are breakage, coalescence, and nucleation. However, nucleation is only considered when

modelling crystallisation for instance when modelling the growth rate or decay of stalagmites and stalactites.

The two most prevalent processes in multiphase mixing are breakage and coalescence. Breakage is the splitting up of a dispersed phase particle into two particles while coalescence is the combination of two smaller particles into one. This is caused by particle collision due to turbulent effects [146].

9.1.3.1.1 Hibiki-Ishii model

Fluent offers a few sets of models to solve the source terms. These are the Yao-Morel model, the Ishii-Kim model, and the Hibiki-Ishii model. The Yao-Morel model is more used in nucleation modelling while the Ishii-Kim model is only viable for bubbly flows (gas-liquid). The Hibiki-Ishii model was therefore employed for modelling the crude-water mixture.

The Hibiki-Ishii model for the random coalitions, wake entrainment and breakage due to turbulent impact source terms appears as:

$$S_{RC} = -\frac{1}{3\varphi}\left(\frac{\alpha_q}{\chi_p}\right)^2 f_C n_q \lambda_C \tag{9.21}$$

where φ is the kinetic energy transfer, f_c is the frequency of particle collisions, λ_c is the efficiency of coalescence from collision and n_q represents the number of particles per unit volume.

$$S_{TI} = -\frac{1}{3\varphi}\left(\frac{\alpha_q}{\chi_p}\right)^2 f_B n_e \lambda_B \tag{9.22}$$

where n_e is the number of turbulent eddies in the primary phase, f_B is the frequency of particle collisions, λ_B is the efficiency of breakage from collision.

9.1.4 Simulation setup

Upon first initializing Fluent, the options were set to double precision. This is a requirement for multiphase Eulerian modelling due to the simulation requiring solving transport equations for multiple fluids simultaneously.

After initializing, within the general setup, the simulation was set as a pressure-based solver operating in steady state. The gravitational constant was set to $-9.81\ \mathrm{m/s^2}$. The multiphase model was set to Eulerian with the formulation being set to implicit. Implicit formulations mean that to arrive at a solution, the simulation solves equations for both the current and future states of the system.

The materials within the system were then defined. For this simulation, they were water and crude oil from the Conroe, Texas. The physical properties are provided in Table 9-2.

Table 9-2 Physical characteristics of fluids at Normal Temperature and Pressure.

Fluid	Density (kg/m^3)	Viscosity (mPa s)	Interfacial Tension (mN/m)
Water	1000	1	_
Conroe Crude oil	848	3.1	20

Following this the phases were then defined. The primary phase was assigned to the crude oil with water being set as the secondary phase. Under the secondary phase (water) the IAC (interfacial area concentration) can be specified. The importance of this with regards to its effect on drag was discussed in equation (*9.16*). The diameter was set to the Sauter mean diameter and the mean and max diameters were left at the default values of a minimum diameter of 1×10^{-5} m and max diameter of 1×10^{-2} m. The breakage kernel was set to the Hibiki-Ishii model. The coalescence kernel was also set to the Hibiki-Ishii model as shown in Figure 9-2.

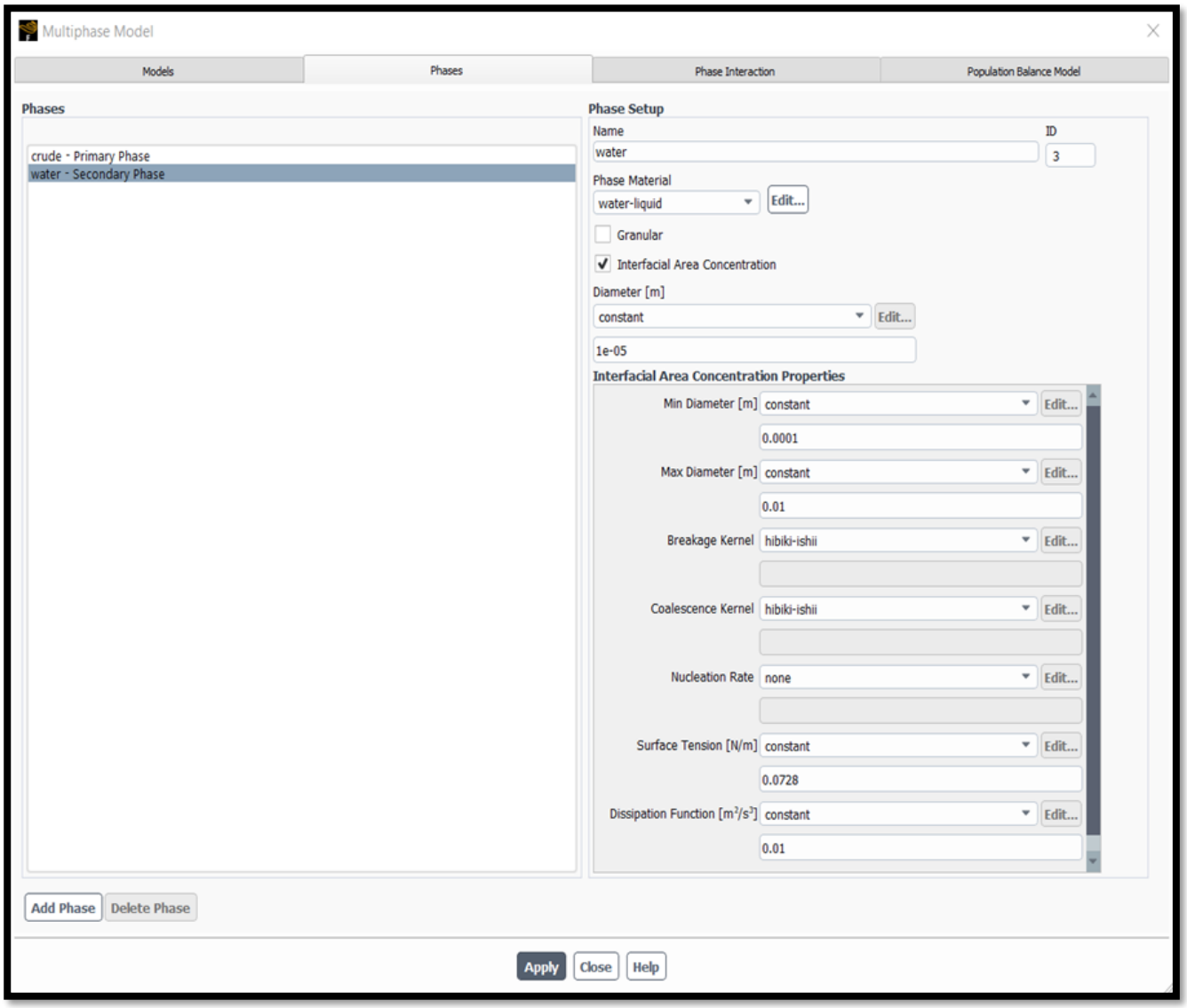

Figure 9-2 Image outlining the designations for the secondary phase in the multiphase model.

The next step involved setting up the phase interactions. Due to the prominence of the drag force within the source terms of the Eulerian momentum transport equation, the drag coefficient was the only specified force within the force setup. This was set to the Schiller-Naumann coefficient as seen in Figure 9-3.

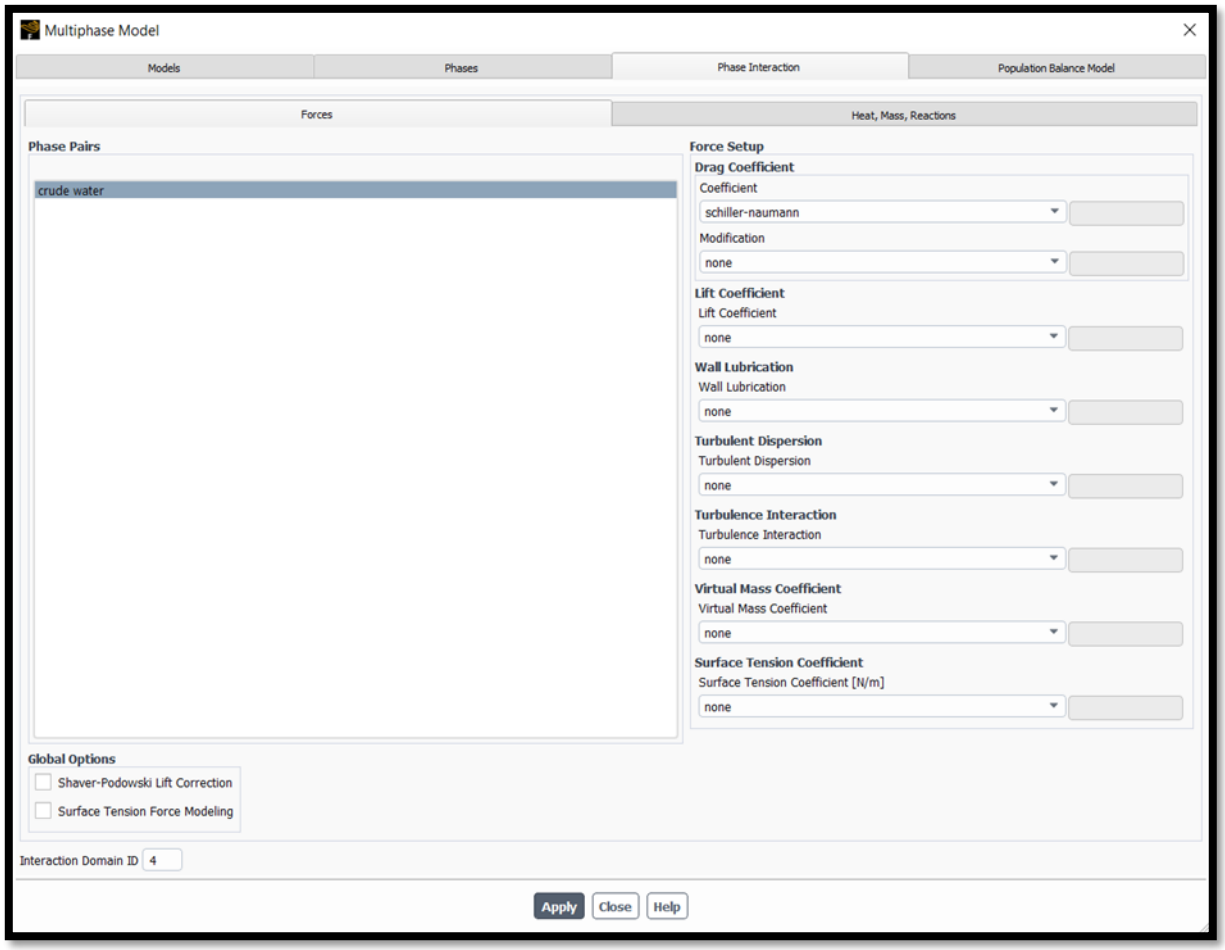

Figure 9-3 Image of the phase interaction setup.

The viscous model was set to the specifications of the single fluid flow model discussed in the single fluid flow sections.

For the solution method, the pressure-velocity coupling was set as phase-coupling SIMPLE. The absolute residual values were set to the optimized set while the iac and volume fraction residuals were set to 0.0087. This value was found to be the smallest value that yielded a stable simulation. Whenever the value was lowered, the simulation would breakdown while trying to converge. The solution was then initialized.

A volume of $9.894 \times 10^{-2} m^3$ of water was patched to the bottom of the mixing tank. The primary phase by default occupies the entire calculable volume (stirred tank reactor). Using the cell registers, 10% of this volume at the bottom of the mixing tank was set to comprise of water. The simulation was then left to run.

9.1.5 Results and analysis

9.1.5.1 Volume fraction distribution

Figure 9-4 shows the volume fraction of water along the x-axis locations.

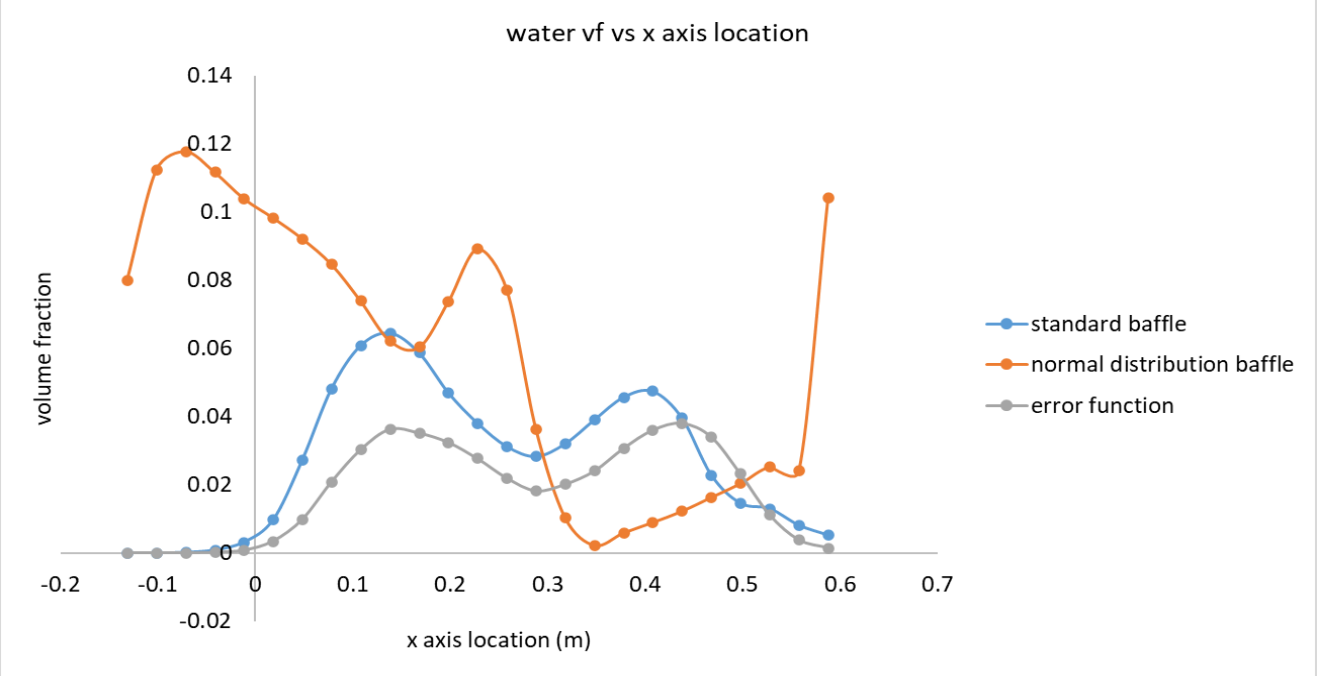

Figure 9-4 Water volume fraction profile along the x-axis line location.

At the x axis location, the volume fraction of water varies substantially for each baffle configuration. This is consistent with a region of high agitation. The normal distribution baffle has the highest volume fraction content of 0.118 and 0.089. The curve also provides a minimum water volume fraction of 0.0023 for the normal distribution configuration baffle. The maxima within the normal distribution baffle configuration are substantially higher than those of the standard and error function configurations. The maxima for the standard baffle are 0.064 and 0.047 and a minimum of 0.00523. The maxima for the error function baffle configuration are 0.038 and 0.036 and a minimum value of 0.0014. The normal distribution baffle configuration has volume fraction values in the range $0.118 \leq \alpha_w \leq 0.0023$ providing a difference of 0.1157. This volume fraction difference is greater than that of the standard baffle (0.05874) and the error function baffle (0.0366). Thus, at this location, the dispersion provided by the normal distribution baffle is the most ideal.

The x axis location average velocity for the normal distribution function configuration baffle was found to be 0.01296. This is the lowest of the three baffle configurations with the standard baffle having an average value of 0.0274556 and 0.0184 for the error function baffle. This further reinforces the fact that there is better dispersion in this location by the normal distribution baffle.

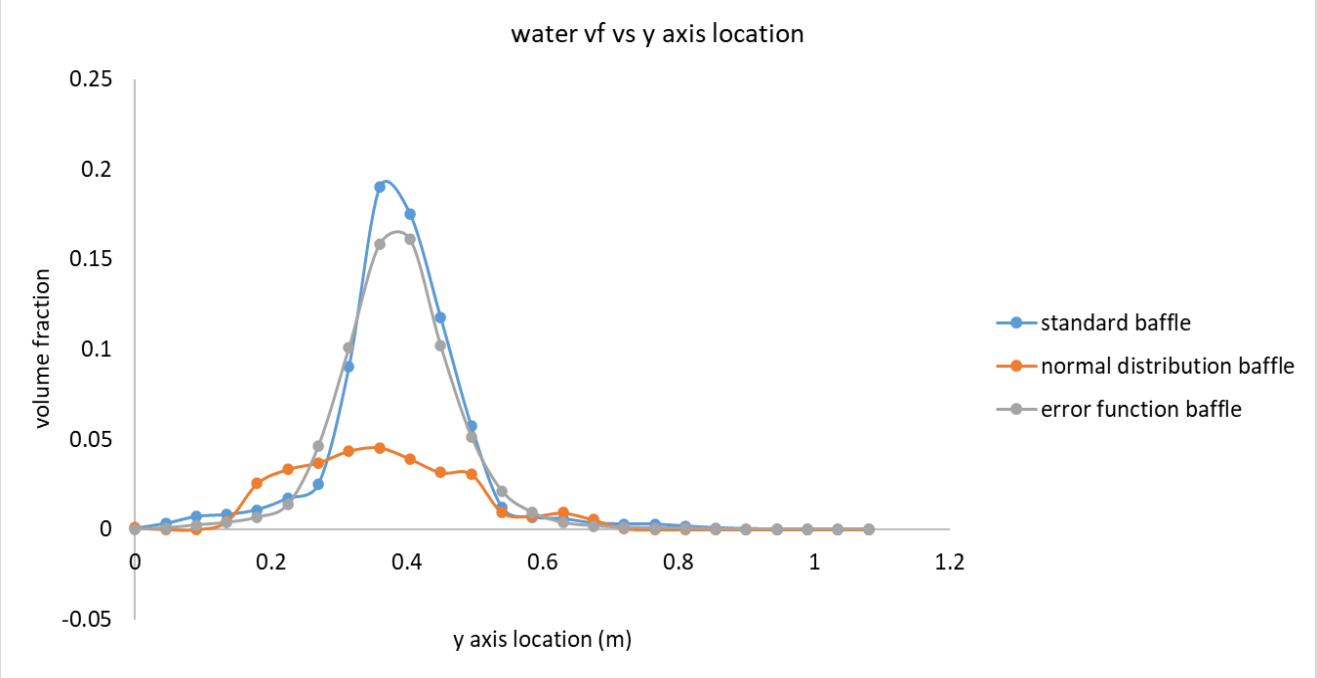

Figure 9-5 Volume fraction profile along the y-axis location.

When samples are taken along the height of the mixing tank, the volume fraction of water indicates higher concentration of water within the baffle region. This is especially apparent within the stirred tanks with the standard and error function baffles. While the water volume fraction within the normal distribution baffle configuration tank is not quite as high, it is more widely dispersed across the y axis location of the stirred tank reactor. This can be observed in the y axis range $0.18\ \text{m} - 0.495\ \text{m}$ where the water volume fraction is greater than 0.0255. For the standard and error function baffled stirred tanks, the volume fraction exceeds this within a narrower band of height measurement of $0.27\ \text{m} - 0.495\ \text{m}$. The fact that the water content in this region of the error function and standard baffled mixing tanks is that high as demonstrated by the high volume fraction values doesn't lend to there being good dispersion as it indicates that there is a lot of retention of the dispersed phase within this region. Considering, the tanks contained an initial volume of 10% water, at the bottom of the tank, having values of $15 - 20\%$ water implies that the baffles are doing a relatively poor job of disrupting the flow of the water particles thereby breaking them apart.

When looking at the average volume fractions in the y axis location, the normal distribution baffle has the smallest value of 0.012 with the standard baffle coming in at 0.029 and the error function baffle coming in at 0.0275. This indicates at a lower retention rate for dispersed water particles at this region for the normal distribution baffle.

Location planes were introduced at various sections of each mixing tank design. The planes were constructed in the Z-X axis and were generated for Y axis values equidistant to one another at $Y = 0.18\ \text{m}, 0.36\ \text{m}, 0.54\ \text{m}, 0.72\ \text{m}, \text{and}\ 0.9\ \text{m}$. Each of these planes was designated a title for ease of discussion.

Table 9-3 Naming scheme of the planes.

Y value (m)	**Title**
0.18	Frac1
0.36	Frac2
0.54	Frac3
0.72	Frac4
0.9	Frac5

9.1.5.2 Normal distribution function baffle mixing tank

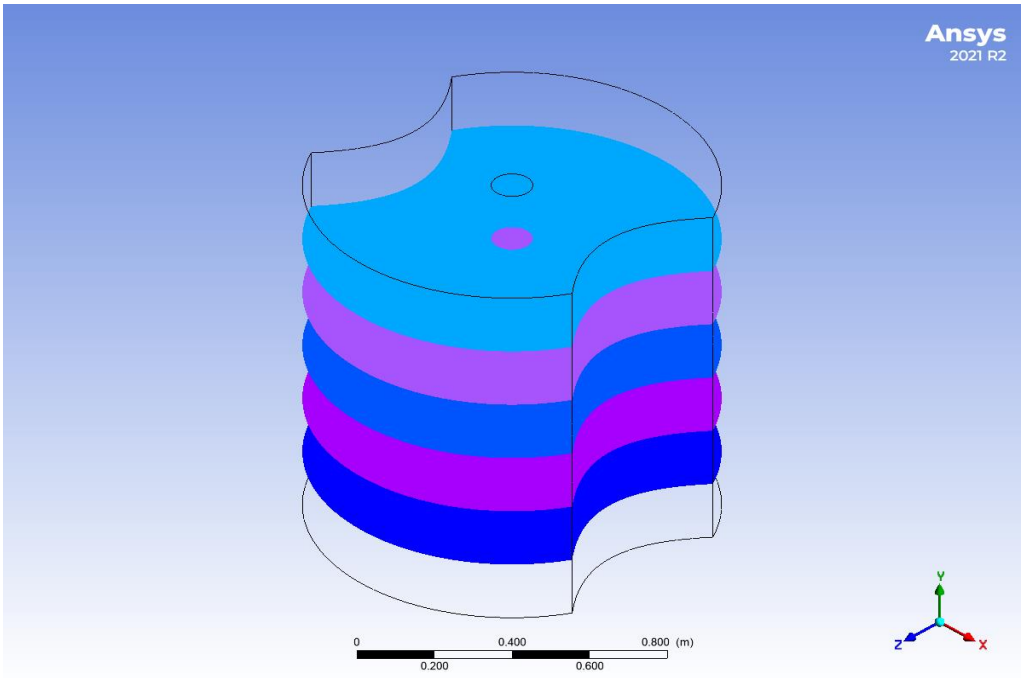

Figure 9-6 Image depicting the location of the examination planes.

Figure 9-6 above shows the 5 planes of analysis in the multiphase normal distribution function baffled stirred tank. Some useful data can be obtained from these regions. Volume fraction data was obtained on each plane. This can be visualised in the contours below:

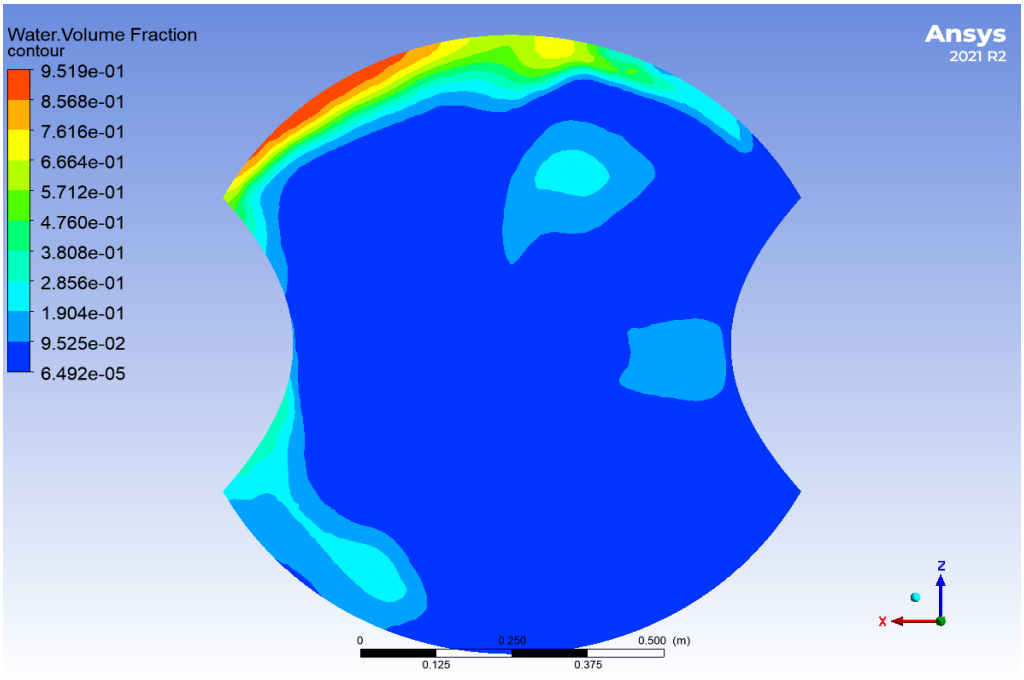

Figure 9-7 A visual representation of water volume fraction at frac1.

The contour for frac 1 indicates a high density of water around the tank wall. The average volume fraction of the dispersed phase at this location is 9.18×10^{-2}.

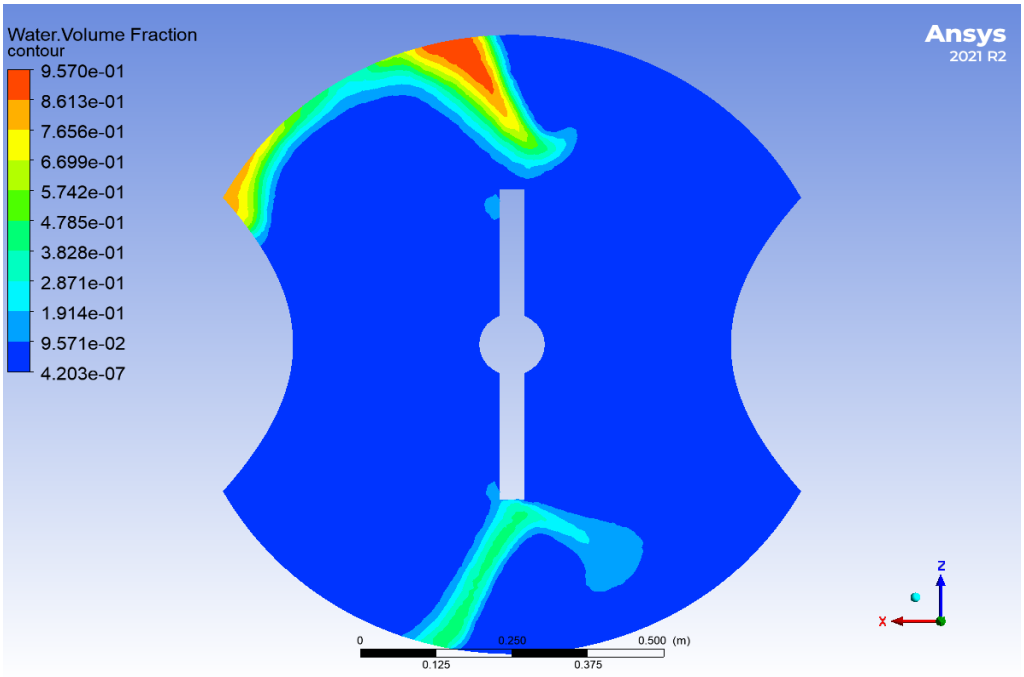

Figure 9-8 A visual representation of water volume fraction at frac2.

Similar to the frac1 contour, the frac 2 contour indicates higher water density along the tank wall with high dispersion the nearer the fluid mixture is to the impeller. The overall volume fraction of water is 6.49×10^{-2}.

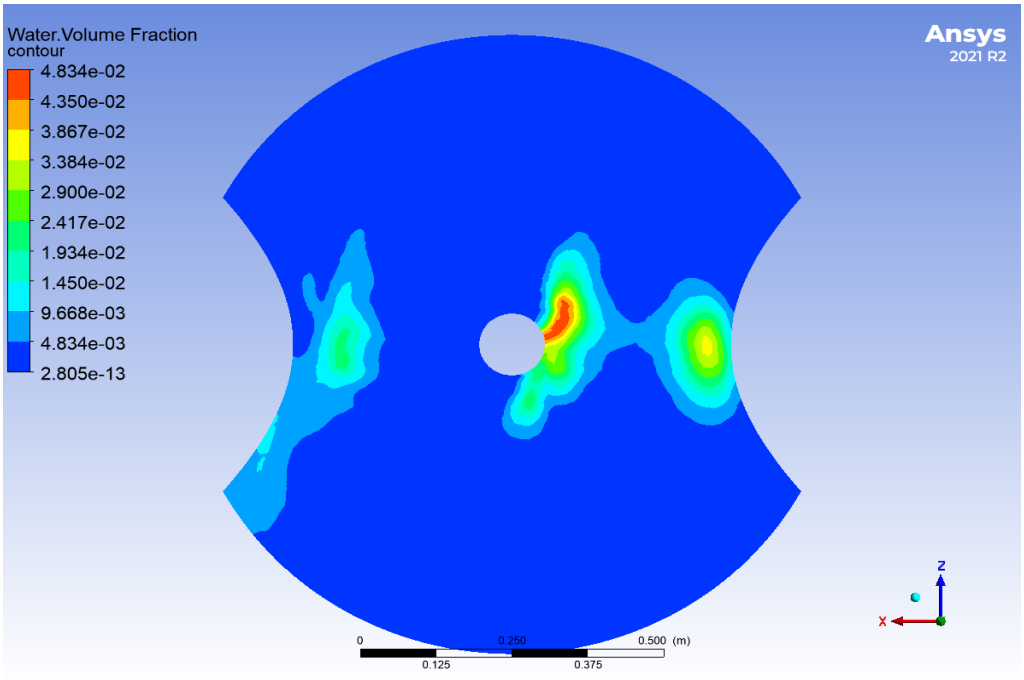

Figure 9-9 A visual representation of water volume fraction at frac3.

At frac3, a location above the impeller blades, the dispersed phase density rises towards the centre of the mixing tank. There is also a high density of water droplets near the baffle region. At this location the average volume fraction of water is 2.37×10^{-3}.

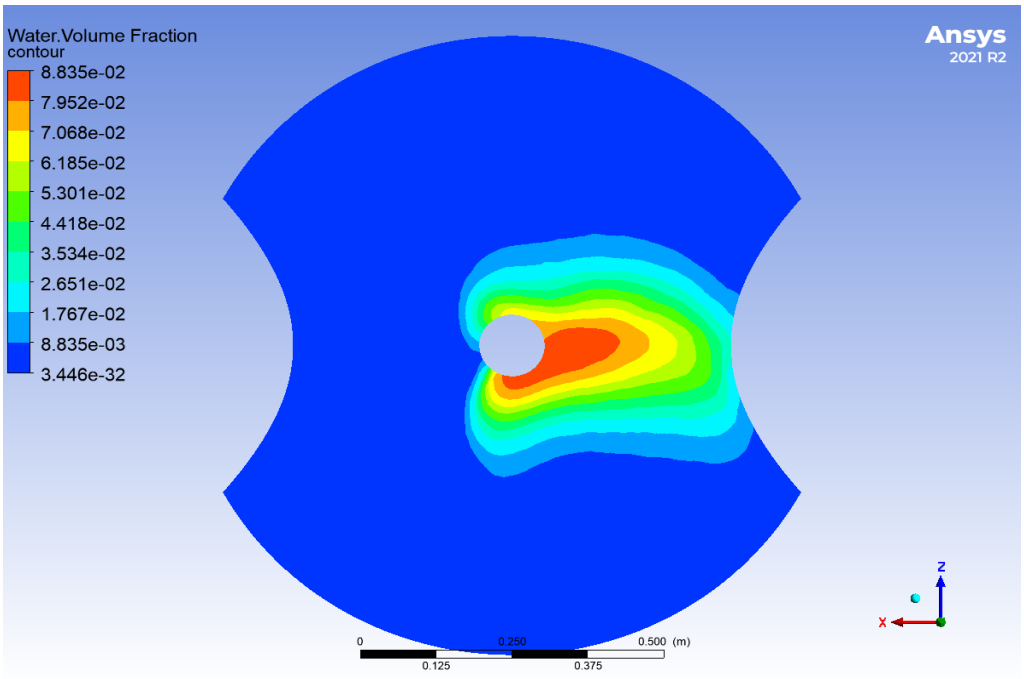

Figure 9-10 A visual representation of water volume fraction at frac4.

Similar to Figure 9-9, the density of water near the mixing tank centre is higher than at the tank wall. There is also a high water droplet density near the baffle wall. At this location, the average water volume fraction is 8.159×10^{-3}.

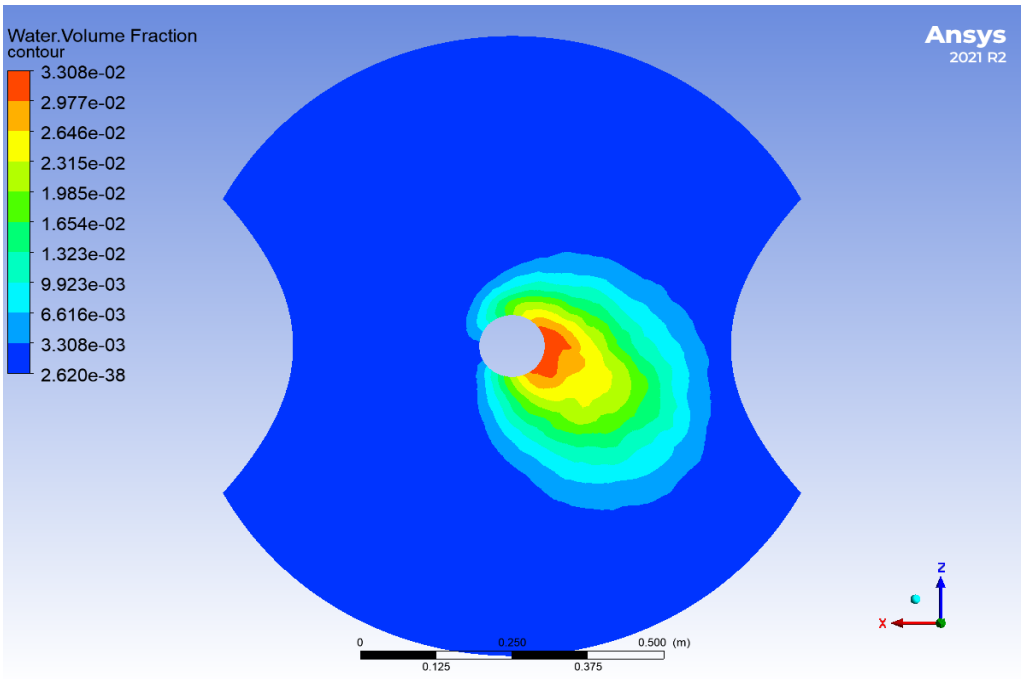

Figure 9-11 A visual representation of water volume fraction at frac5.

The frac5 contour maintains the trend of water droplet density being higher nearer the impeller shaft (mixing tank centre) with a moderate amount of water being located near the baffle wall. The average volume fraction along this plane is 2.2×10^{-3}.

Table 9-4 Table of the average water volume fraction at the different planes within the normal distribution function configuration mixing tank.

Location	**Average water volume fraction**
Frac1	9.18×10^{-2}
Frac2	6.49×10^{-2}
Frac3	2.37×10^{-3}
Frac4	8.159×10^{-3}
Frac5	2.2×10^{-3}

The relatively narrow band of average volume fraction distribution obtained at each location is indicative of good dispersion of water bubbles.

9.1.5.3 *Error function baffle mixing tank*

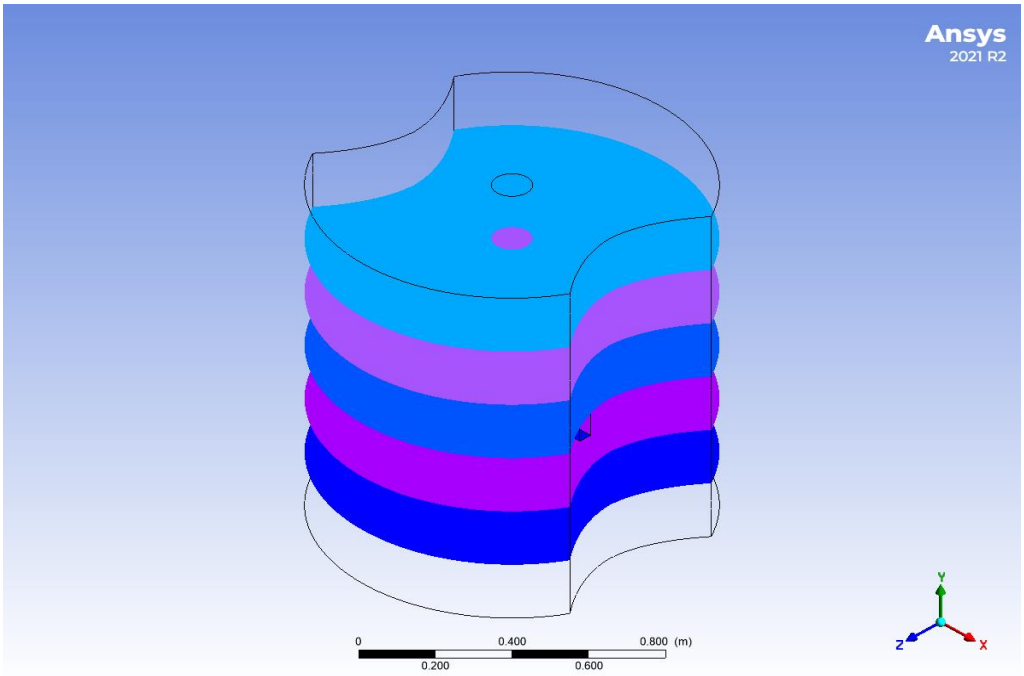

Figure 9-12 image depicting the location of the examination planes.

The water volume fraction data obtained at each plane is represented in the contours displayed below:

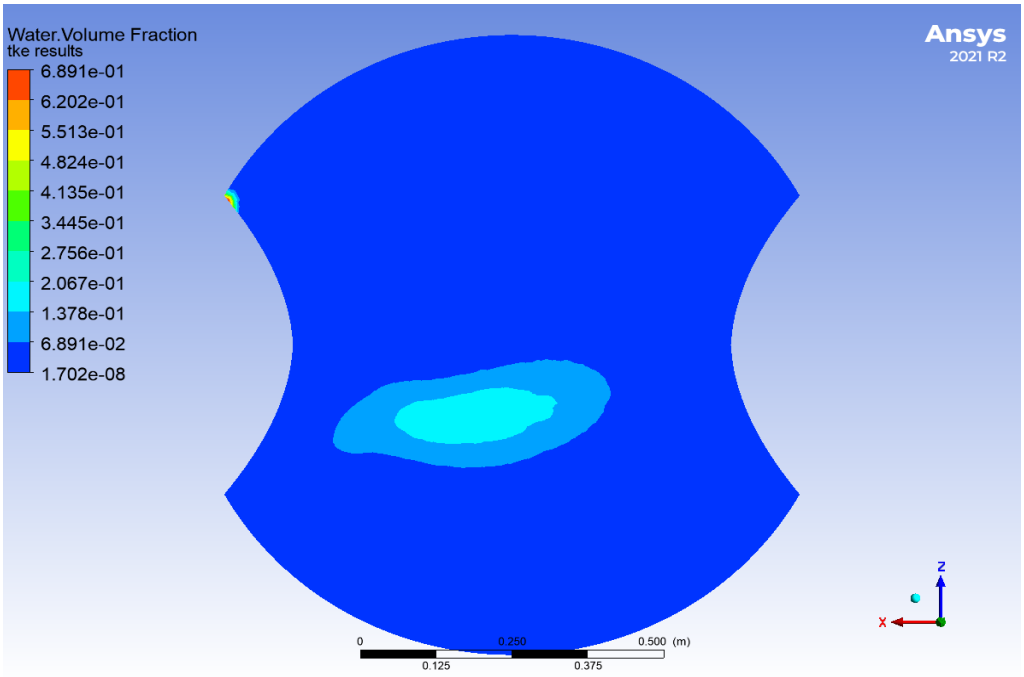

Figure 9-13 Contour of water volume fraction at frac1.

At frac1 the average volume fraction of water at this location is 1.605×10^{-2}. The contour indicates the presence of a higher density of water near the mixing tank centre. There also appears to be a region of high dispersed phase retention near the error function baffle. This indicates less efficient mixing at this location.

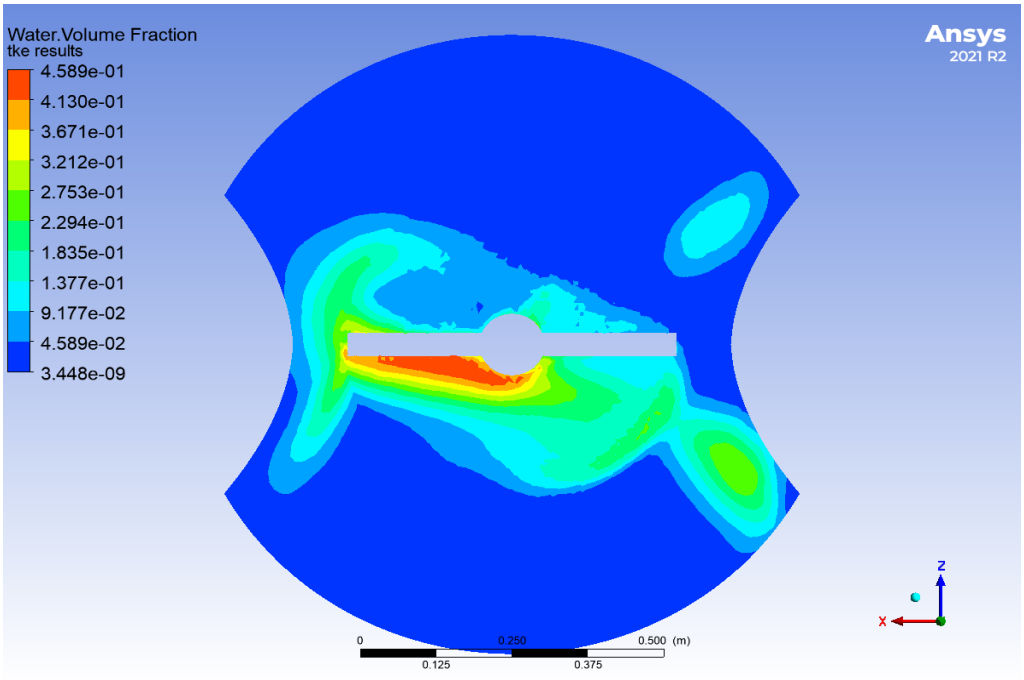

Figure 9-14 Contour of water volume fraction at frac2.

The average volume fraction of water at frac 2 relatively high at 5.115×10^{-2}. This indicates high dispersed phase retention at this location. The highest density of water droplets is located nearest to the impeller region.

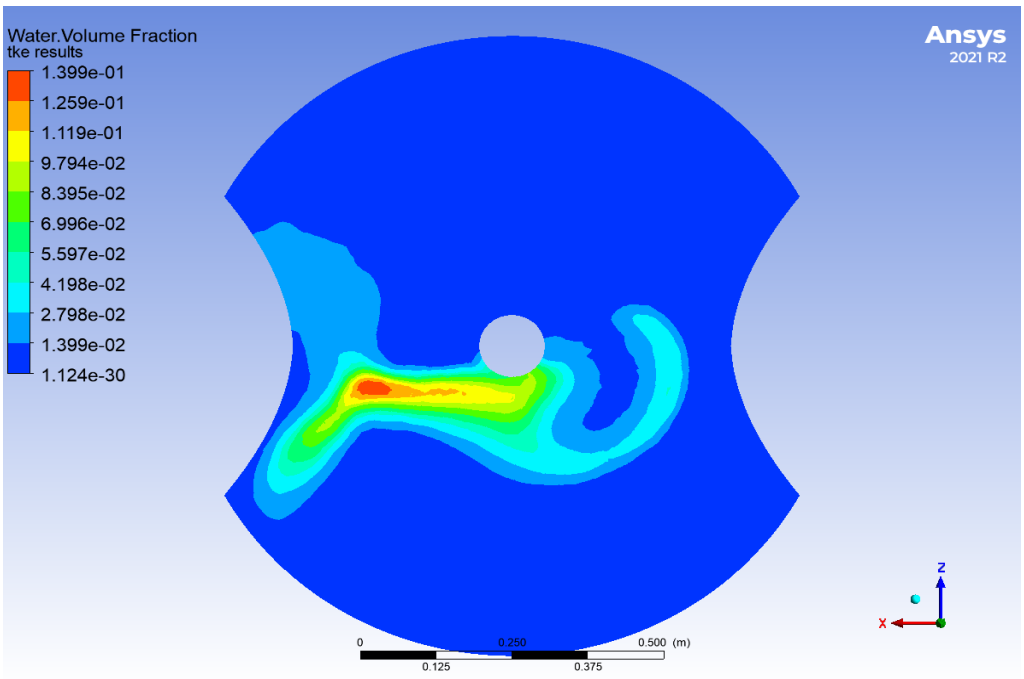

Figure 9-15 Contour of water volume fraction at frac3.

Similar to frac 2, the contour of frac 3 displays a large density of dispersed phase droplets are located closer to the centre of the mixing tank (impeller shaft). The average water volume fraction at this location is 8.889×10^{-3} which is greater than at frac2.

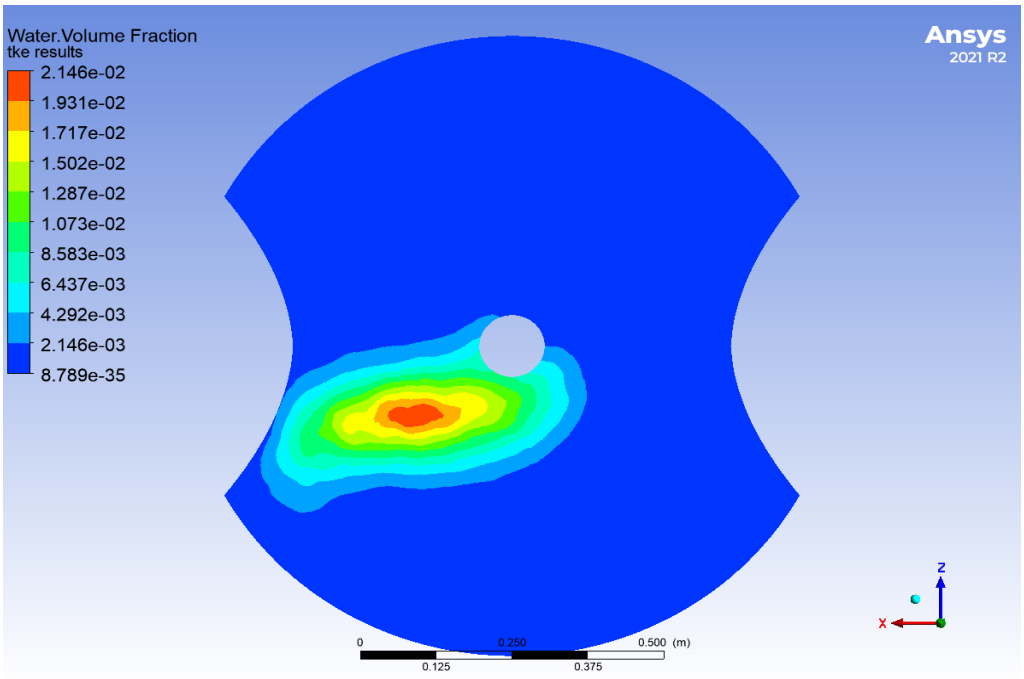

Figure 9-16 Contour of water volume fraction at frac4.

At frac4, the average water volume fraction is1.320×10^{-3}. This is a substantial decrease from frac 3 indicative of less water being distributed to this location from the bottom of the mixing tank.

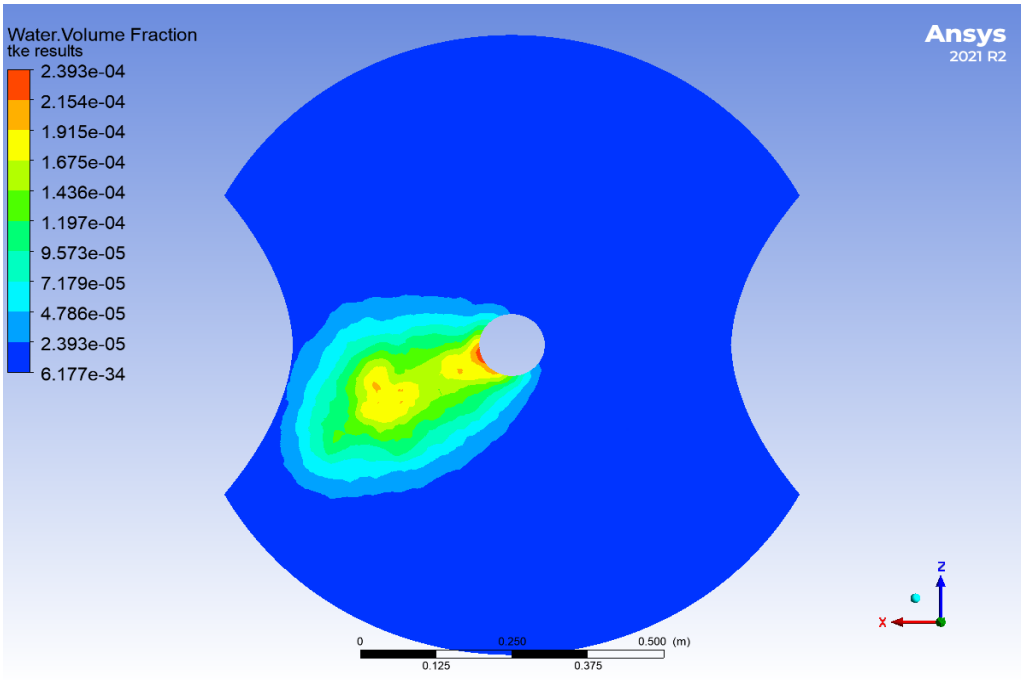

Figure 9-17 Contour of water volume fraction at frac5.

At frac5 there is a negligible amount of water standing at a volume fraction measurement of 1.308×10^{-5}. A majority of this is coalesced near the centre of the mixing tank.

Table 9-5 Table of average water volume fraction at different planes within the error function baffle configuration mixing tank.

Location	Average water volume fraction
Frac1	1.605×10^{-2}
Frac2	5.115×10^{-2}
Frac3	8.889×10^{-3}
Frac4	1.320×10^{-3}
Frac5	1.308×10^{-5}

As seen in Table *9-5*, the average water volume fraction decreases substantially at frac5. This implies that the bulk of the dispersed phase is retained below plane frac5.

9.1.5.4 Standard baffle mixing tank

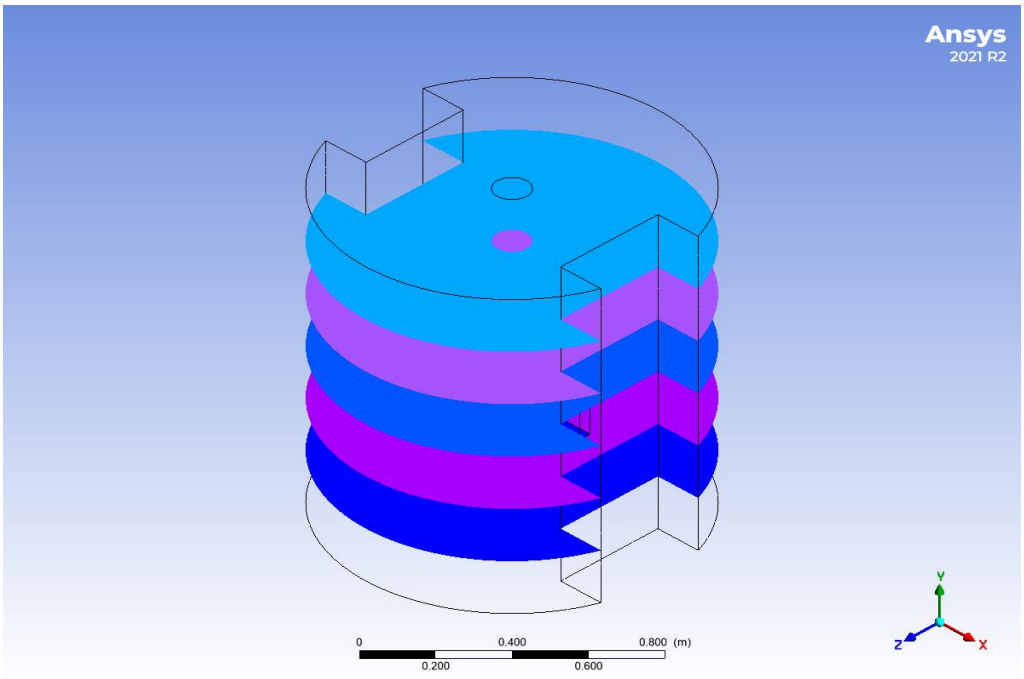

Figure 9-18 Image depicting the location of the examination planes.

The volume fraction of water at each individual plane is displayed in the contours provided below:

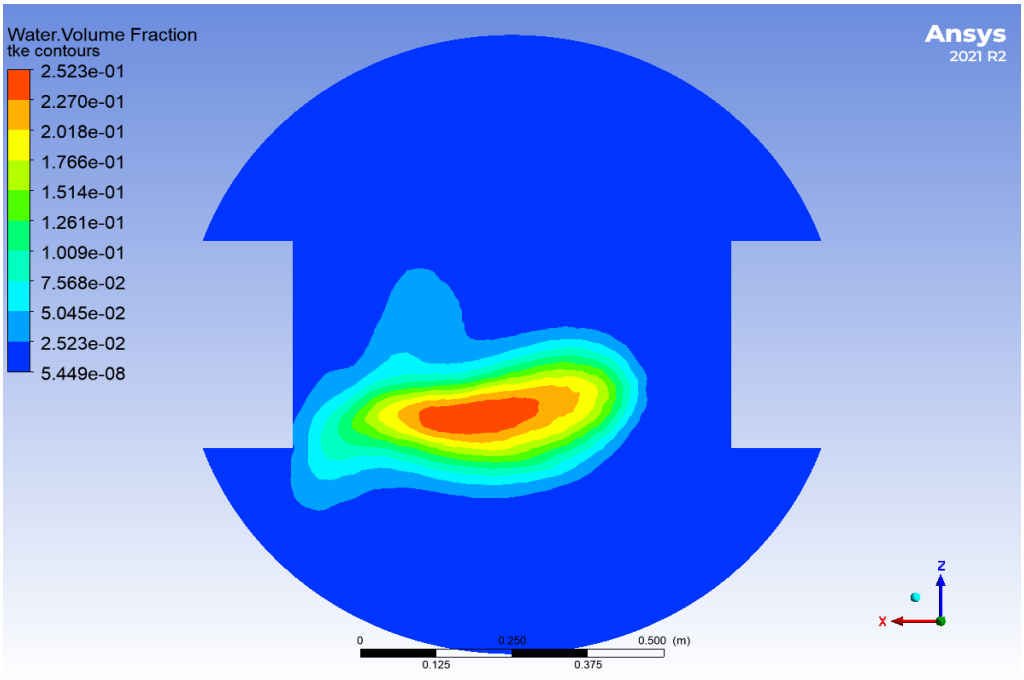

Figure 9-19 Contour of water volume fraction at frac1.

The above contour displays the water droplet distribution at frac 1. The average volume fraction at this location was found to be 2.229×10^{-2}. A large density of which was located near the centre of the mixing tank.

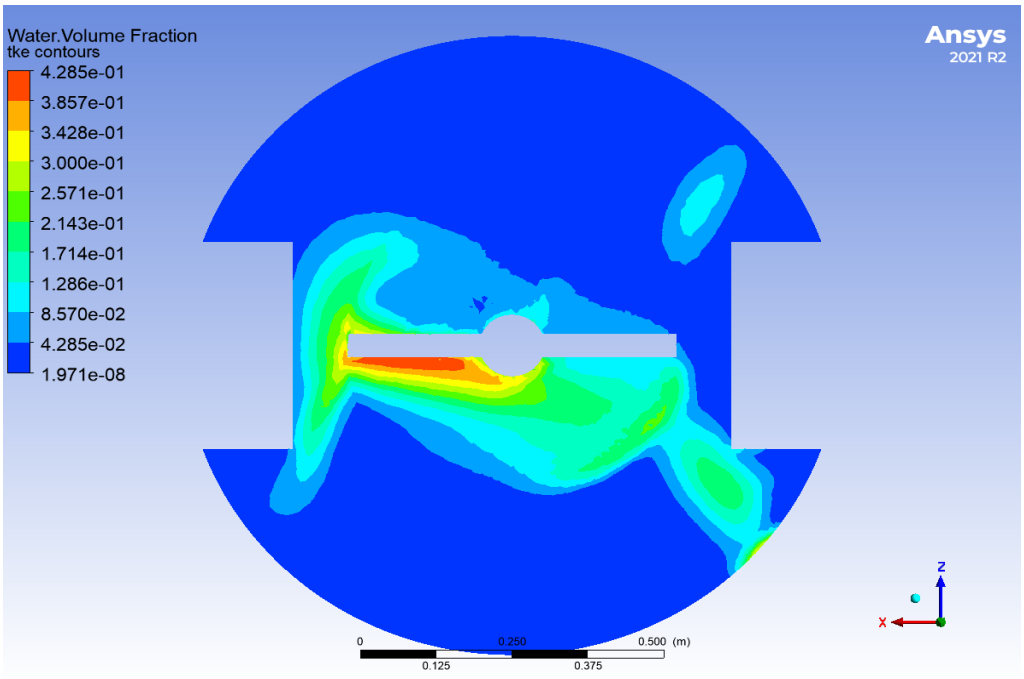

Figure 9-20 Contour of water volume fraction at frac2.

From Figure 9-20 water is observed to be more uniformly distributed across frac 2 than across frac 1. However, the density of water is much higher with a volume fraction of 4.419×10^{-2}.

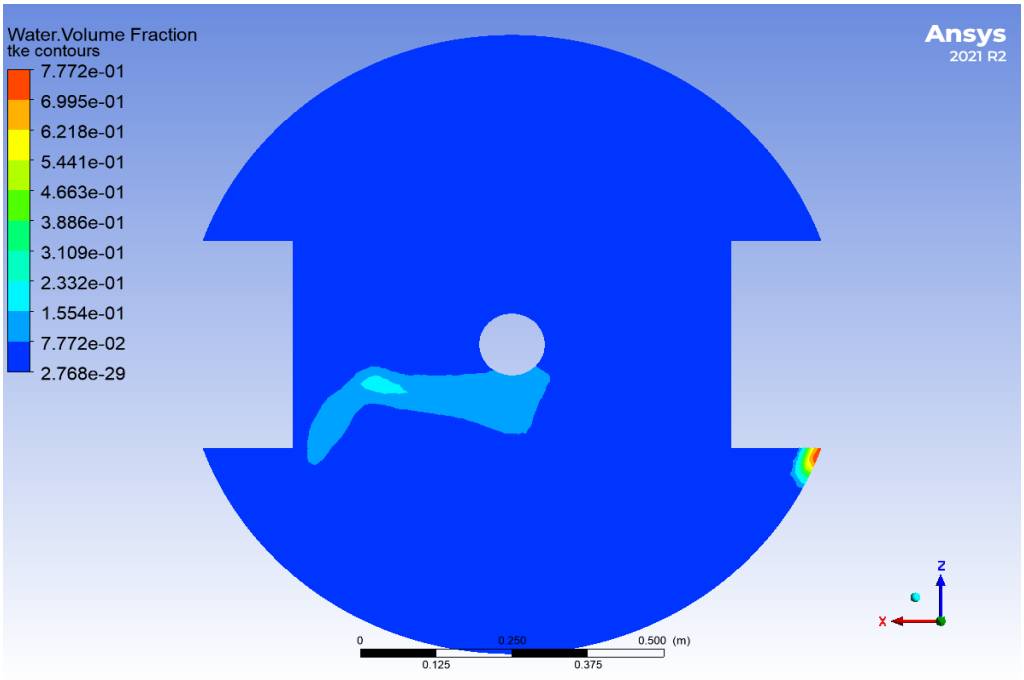

Figure 9-21 Contour of water volume fraction at frac3.

From the contour of frac3, water retention is observed at the baffle edge. This is an indicator of poor dispersal at this location. However, there is a uniform distribution of water across the plane with a volume fraction of 1.210×10^{-2}.

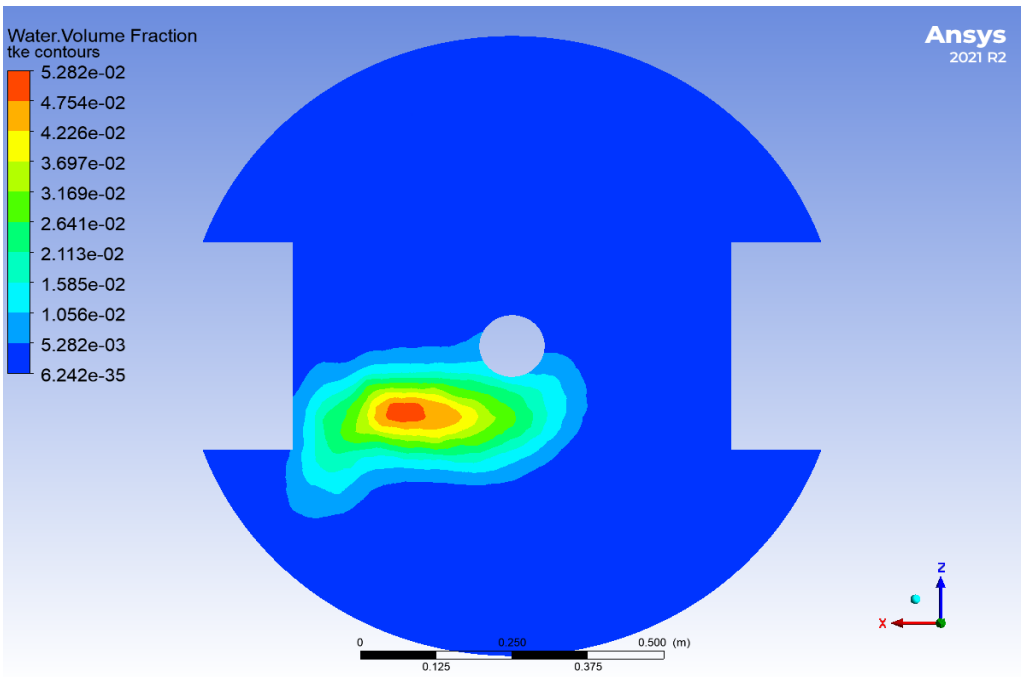

Figure 9-22 Contour of water volume fraction at frac4.

The frac4 contour shows that a majority of the dispersed phase has coalesced near centre of the mixing tank with an overall volume fraction of 2.875×10^{-3}.

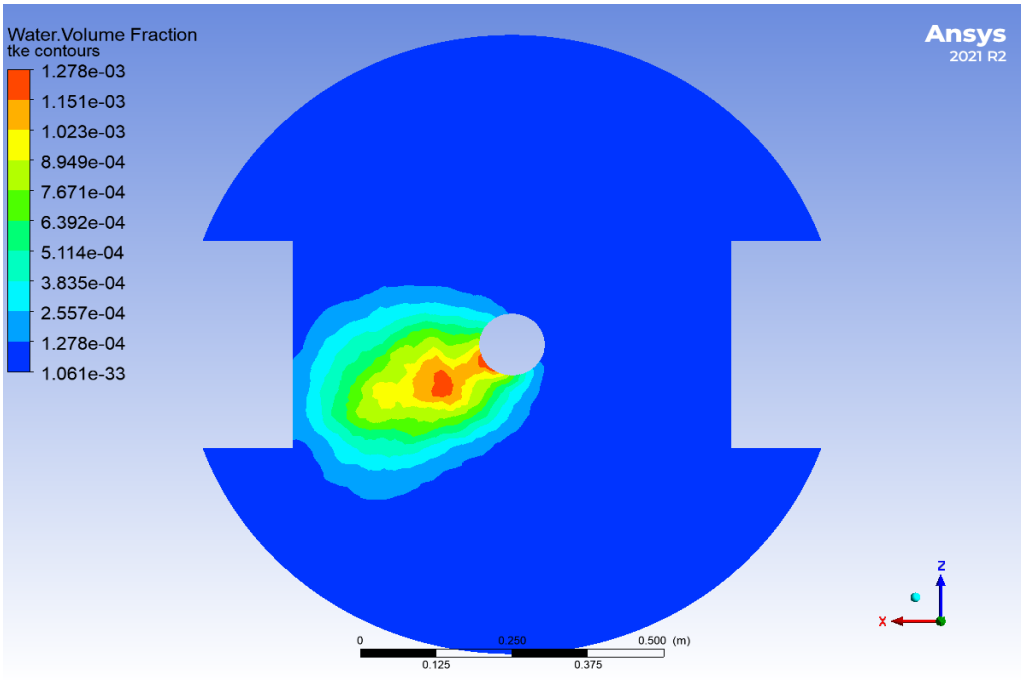

Figure 9-23 Contour of water volume fraction at frac5.

There is a substantial overall volume fraction drop with a value of 7.23×10^{-5}. Like in the contour of frac4 the water droplets are more concentrated near the mixing tank centre.

Table 9-6 Table of average water volume fraction values at different planes within the standard baffle configuration mixing tank.

Location	Average water volume fraction
Frac1	2.229×10^{-2}
Frac2	4.419×10^{-2}
Frac3	1.210×10^{-2}
Frac4	2.875×10^{-3}
Frac5	7.23×10^{-5}

From the data in Table 9-6 above, like the error function baffle configuration, the standard baffle configuration has little to no dispersed phase presence at frac5.

9.1.5.5 Water volume fraction conclusions

The dispersion of water within normal distribution baffle stirred tank reactor from frac1 to frac5 is $9.18 \times 10^{-2} \geq \alpha_w \geq 2.2 \times 10^{-3}$ with a uniform distribution of the dispersed particles especially when compared to the error function baffle configuration which produces a volume fraction distribution range of $5.115 \times 10^{-2} \geq \alpha_w \geq 1.308 \times 10^{-5}$. This lower limit value indicates a

negligible presence of the dispersed phase at this location. The same was observed for the standard baffle configuration with a water volume fraction range of $4.419 \times 10^{-2} \geq \alpha_w \geq 7.23 \times 10^{-5}$.

However, comparing frac4 average water volume fraction values for the standard baffle configuration to that of the error function baffle configuration, the standard baffle has a higher density of dispersed water than that of the error function baffle.

All this means that for the dispersal of water in Conroe crude oil, the most ideal baffle configuration of the three proposed baffles is the normal distribution baffle. The second most suitable design is the standard baffle configuration and lastly the error function baffle configuration.

10 Conclusion

Over the course of this thesis, an analysis of design practises for mixing tanks was undertaken. This involved an in-depth discussion of the incompressible fluid flow using Navier-Stokes equation and the Reynolds averaging process for solving it. The realizable $k - \varepsilon$ eddy viscosity model was used to model the initial mixing tank design and its results were used to optimise the simulation process. The development of this optimisation scheme satisfied one of the objectives that this thesis set out to achieve. A statistical method called factor analysis was used to obtain the ideal element size and absolute convergence criteria. The mesh element size criterion was determined to be 1.34 cm and the absolute convergence criteria were found to be 1.3×10^{-3}.

The goal of determining the most suitable baffle size was attained through the analysis of the various velocity and pressure profiles with the 2:1 baffle configuration was determined to be the optimal baffle dimension for agitating water in the mixing tank. An analysis of baffle shapes was also undertaken with a few proposed shapes, aside from the standard rectangle shape, normal distribution and the error functions based baffle shapes were modelled. Pressure and velocity profiles showed that the normal distribution baffle was the most suitable design for the single fluid flow mixing tank.

A substantial portion of this thesis was dedicated to analysing multiphase simulations with a particular focus on the Eulerian multiphase model. The Eularian model was used to simulate a 10% volume of water dispersed in 90% volume of Conroe crude oil. To determine the distribution patterns in the stirred tank reactors with the standard, normal distribution, and error function baffle configurations, the average water volume fraction was extracted at different locations within the mixing tank. The normal distribution baffle configuration appeared to have the highest concentration of water with a volume fraction of 2.2×10^{-3}. This was higher than 7.23×10^{-5} for the rectangle baffle and 1.308×10^{-5} for the error distribution function baffle configuration design. This served to complete the objective of a multiphase flow analysis for the mixing tank bearing different baffle shape designs.

11 Recommendations for future work

Experimental validation of the modelling of the baffles and the mixing pattern in particular the pattern for two immiscible phases was planned before COVID-19. Nonetheless, as a result of the pandemic, this was proven not possible. Nevertheless, scaled down mixing tanks can be used in conjunction with experimental techniques such as PIV (Particle image velocimetry) to verify the simulation results in particular in terms of velocity profile and volume distribution of the disperse phase (for two immiscible phase mixing case).

From the perspective of baffle design, three shapes were constructed and discussed in this thesis: rectangle, normal distribution function and error function based. Nevertheless, many other shapes are also available. It would thus be extremely useful to categorise these geometric shapes in a systematic way such as according to the length to width aspect ratio and the roundness of the top tip. This would entail not only a systematic study but also a statistical analysis of the simulation results to obtain the optimised baffle shape structure for best mixing.

This study only focuses on the structure of baffle shape, the structure of mixer was fixed to a defined shape. It would also be useful to introduce the mixer of different shapes into simulation to see how they would affect the mixing pattern in terms of velocity and pressure profiles and concentration distribution of the disperse phase (for two immiscible phase mixing case).

In immiscible phase mixing, breakage from the mixer is essentially the mechanism how the size of the disperse phase droplets got reduced. However, eventually this breakage process and the coalescence of the droplets will strike a balance so that the reduction of the droplet size becomes no longer possible under a defined mixer speed. To understand and describe this connection: mixer speed to final size of the droplets of the disperse phase, a so-called population balance approach would be useful. This will eventually establish a mathematical relationship between the power input from the mixer and the final droplet size of the disperse phase in the situation of immiscible phase mixing. Additionally, to understand the deformation of the interface between the two immiscible bulk fluids, a VOF model could be employed. This running in transient would enable the user to understand the effect of the deferring stirred tank designs on the fluid-fluid interface with respect to time. Nevertheless, this remains to be something interesting to be seen in the future. From a philosophical point of view, knowing how is done is knowing when is done!

Nomenclature

α – volume fraction (-)

ρ – density (kg/m^3)

U – velocity (m/s)

μ – dynamic viscosity (Pa s)

l_m – mixing length (m)

ε – Dissipation of turbulent kinetic energy (J/m^3)

$\dot{m}$ – mass flow rate (kg/s)

Re – Reynolds number (-)

D – diameter (m)

l_m – mixing length (m)

μ_t – turbulent viscosity (-)

v – kinematic viscosity (m^2/s)

σ – turbulent Prandtl number (-)

erf – error function

C_p – Specific heat capacity (J/(kg.K))

Abbreviations

iac – interfacial area concentration

VOF – volume of fluid

FA – Factor Analysis

PCA – Principal component analysis

Subscripts

n – number of phases

p – primary phase

q – secondary phase

References

[1] A. Busciglio, F. Grisafi, F. Scargiali, A. Brucato, Mixing dynamics in uncovered unbaffled stirred tanks, Chemical Engineering Journal, 254 (2014) 210-219.
[2] A. Fall, O. Lecoq, R. David, Characterization of Mixing in a Stirred Tank by Planar Laser Induced Fluorescence (P.L.I.F.), Chemical Engineering Research and Design, 79 (2001) 876-882.
[3] M. Basavarajappa, T. Draper, P. Toth, T.A. Ring, S. Miskovic, Numerical and experimental investigation of single phase flow characteristics in stirred tanks using Rushton turbine and flotation impeller, Minerals Engineering, 83 (2015) 156-167.
[4] C.-Y. Ge, J.-J. Wang, X.-P. Gu, L.-F. Feng, CFD simulation and PIV measurement of the flow field generated by modified pitched blade turbine impellers, Chemical Engineering Research and Design, 92 (2014) 1027-1036.
[5] K. Vaagsaether, A.V. Gaathaug, D. Bjerketvedt, PIV-measurements of reactant flow in hydrogen-air explosions, International Journal of Hydrogen Energy, 44 (2019) 8799-8806.
[6] P. Mavros, C. Xuereb, I. Fořt, J. Bertrand, Investigation by laser Doppler velocimetry of the effects of liquid flow rates and feed positions on the flow patterns induced in a stirred tank by an axial-flow impeller, Chemical Engineering Science, 57 (2002) 3939-3952.
[7] N.C. Temperley, M. Behnia, A.F. Collings, Application of computational fluid dynamics and laser Doppler velocimetry to liquid ultrasonic flow meter design, Flow Measurement and Instrumentation, 15 (2004) 155-165.
[8] Z. Chara, B. Kysela, J. Konfrst, I. Fort, Study of fluid flow in baffled vessels stirred by a Rushton standard impeller, Applied Mathematics and Computation, 272 (2016) 614-628.
[9] R. Escudié, A. Liné, Analysis of turbulence anisotropy in a mixing tank, Chemical Engineering Science, 61 (2006) 2771-2779.
[10] G. Ascanio, Mixing time in stirred vessels: A review of experimental techniques, Chinese Journal of Chemical Engineering, 23 (2015) 1065-1076.
[11] G. Ascanio, S. Foucault, P.A. Tanguy, Time-Periodic Mixing of Shear-thinning Fluids, Chemical Engineering Research and Design, 82 (2004) 1199-1203.
[12] A.K. Roy Choudhury, 6 - Chromatic adaptation and colour constancy, in: A.K. Roy Choudhury (Ed.) Principles of Colour and Appearance Measurement, Woodhead Publishing, Oxford, 2015, pp. 214-264.
[13] M.V. Sardeshpande, G. Kumar, T. Aditya, V.V. Ranade, Mixing studies in unbaffled stirred tank reactor using electrical resistance tomography, Flow Measurement and Instrumentation, 47 (2016) 110-121.
[14] H. Bashiri, E. Alizadeh, F. Bertrand, J. Chaouki, Investigation of turbulent fluid flows in stirred tanks using a non-intrusive particle tracking technique, Chemical Engineering Science, 140 (2016) 233-251.
[15] T.P. Elson, D.J. Cheesman, A.W. Nienow, X-ray studies of cavern sizes and mixing performance with fluids possessing a yield stress, Chemical Engineering Science, 41 (1986) 2555-2562.
[16] P. Bonvillani, M.P. Ferrari, E.M. Ducrós, J.A. Orejas, Theoretical and experimental study of the effects of scale-up on mixing time for a stirred-tank bioreactor, Brazilian Journal of Chemical Engineering, 23 (2006) 1-7.
[17] X. Duan, X. Feng, C. Yang, Z. Mao, CFD modeling of turbulent reacting flow in a semi-batch stirred-tank reactor, Chinese Journal of Chemical Engineering, 26 (2018) 675-683.
[18] R.V. Grandhi, C.C. Fischer, Model-Form Uncertainty Quantification for Structural Design, in: M. Beer, I.A. Kougioumtzoglou, E. Patelli, I.S.-K. Au (Eds.) Encyclopedia of Earthquake Engineering, Springer Berlin Heidelberg, Berlin, Heidelberg, 2014, pp. 1-17.

[19] C. Bartels, M. Breuer, K. Wechsler, F. Durst, Computational fluid dynamics applications on parallel-vector computers: computations of stirred vessel flows, Computers & Fluids, 31 (2002) 69-97.
[20] R. Alcamo, G. Micale, F. Grisafi, A. Brucato, M. Ciofalo, Large-eddy simulation of turbulent flow in an unbaffled stirred tank driven by a Rushton turbine, Chemical Engineering Science, 60 (2005) 2303-2316.
[21] N. Qi, H. Zhang, K. Zhang, G. Xu, Y. Yang, CFD simulation of particle suspension in a stirred tank, Particuology, 11 (2013) 317-326.
[22] C.P. Booth, J.W. Leggoe, Z.M. Aman, The Use of Computational Fluid Dynamics to Predict the Turbulent Dissipation Rate and Droplet Size in a Stirred Autoclave, Chemical Engineering Science, (2018).
[23] J. Kamieński, R. Wójtowicz, Dispersion of liquid–liquid systems in a mixer with a reciprocating agitator, Chemical Engineering and Processing: Process Intensification, 42 (2003) 1007-1017.
[24] S. Masiuk, Power consumption measurements in a liquid vessel that is mixed using a vibratory agitator, Chemical Engineering Journal, 75 (1999) 161-165.
[25] A.K. Pukkella, R. Vysyaraju, V. Tammishetti, B. Rai, S. Subramanian, Improved mixing of solid suspensions in stirred tanks with interface baffles: CFD simulation and experimental validation, Chemical Engineering Journal, 358 (2019) 621-633.
[26] A. Tamburini, A. Cipollina, G. Micale, A. Brucato, M. Ciofalo, CFD simulations of dense solid–liquid suspensions in baffled stirred tanks: Prediction of suspension curves, Chemical Engineering Journal, 178 (2011) 324-341.
[27] C. Carletti, G. Montante, C. De Blasio, A. Paglianti, Liquid mixing dynamics in slurry stirred tanks based on electrical resistance tomography, Chemical Engineering Science, 152 (2016) 478-487.
[28] I.D. Kariyama, X. Zhai, B. Wu, Influence of mixing on anaerobic digestion efficiency in stirred tank digesters: A review, Water Research, 143 (2018) 503-517.
[29] D. Ankamma Rao, P. Sivashanmugam, Experimental and CFD simulation studies on power consumption in mixing using energy saving turbine agitator, Journal of Industrial and Engineering Chemistry, 16 (2010) 157-161.
[30] A. Brucato, A. Cipollina, G. Micale, F. Scargiali, A. Tamburini, Particle suspension in top-covered unbaffled tanks, Chemical Engineering Science, 65 (2010) 3001-3008.
[31] M. Mellal, R. Benzeguir, D. Sahel, H. Ameur, Hydro-thermal shell-side performance evaluation of a shell and tube heat exchanger under different baffle arrangement and orientation, International Journal of Thermal Sciences, 121 (2017) 138-149.
[32] A.S. Ambekar, R. Sivakumar, N. Anantharaman, M. Vivekenandan, CFD simulation study of shell and tube heat exchangers with different baffle segment configurations, Applied Thermal Engineering, 108 (2016) 999-1007.
[33] C. Dong, Y. Chen, J. Wu, Comparison of heat transfer performances of helix baffled heat exchangers with different baffle configurations, Chinese Journal of Chemical Engineering, 23 (2015) 255-261.
[34] C. Dong, D. Li, Y. Zheng, G. Li, Y. Suo, Y. Chen, An efficient and low resistant circumferential overlap trisection helical baffle heat exchanger with folded baffles, Energy Conversion and Management, 113 (2016) 143-152.
[35] Z. Duan, F. Shen, X. Cao, J. Zhang, Comprehensive effects of baffle configuration on the performance of heat exchanger with helical baffles, Nuclear Engineering and Design, 300 (2016) 349-357.
[36] Z.Q. Zuo, W.B. Jiang, Y.H. Huang, Effect of baffles on pressurization and thermal stratification in cryogenic tanks under micro-gravity, Cryogenics, 96 (2018) 116-124.

[37] A. Elsayed, C. Bastien, S. Jones, J. Christensen, H. Medina, H. Kassem, Investigation of baffle configuration effect on the performance of exhaust mufflers, Case Studies in Thermal Engineering, 10 (2017) 86-94.
[38] J. Cheng, W. Guo, C. Cai, Q. Ye, J. Zhou, Alternatively permutated conic baffles generate vortex flow field to improve microalgal productivity in a raceway pond, Bioresource Technology, 249 (2018) 212-218.
[39] A. Bylak, K. Kukuła, K. Plesiński, A. Radecki-Pawlik, Effect of a baffled chute on stream habitat conditions and biological communities, Ecological Engineering, 106 (2017) 263-272.
[40] A. Busciglio, G. Caputo, F. Scargiali, Free-surface shape in unbaffled stirred vessels: Experimental study via digital image analysis, Chemical Engineering Science, 104 (2013) 868-880.
[41] R. Zadghaffari, J.S. Moghaddas, J. Revstedt, A mixing study in a double-Rushton stirred tank, Computers & Chemical Engineering, 33 (2009) 1240-1246.
[42] J. Aubin, P. Mavros, D.F. Fletcher, J. Bertrand, C. Xuereb, Effect of Axial Agitator Configuration (Up-Pumping, Down-Pumping, Reverse Rotation) on Flow Patterns Generated in Stirred Vessels, Chemical Engineering Research and Design, 79 (2001) 845-856.
[43] S. Masiuk, J. Kawecka-Typek, Mixing energy measurements in liquid vessel with pendulum agitators, Chemical Engineering and Processing: Process Intensification, 43 (2004) 91-99.
[44] J.Y. Dieulot, G. Delaplace, R. Guerin, J.P. Brienne, J.C. Leuliet, Laminar Mixing Performances of a Stirred Tank Equipped with Helical Ribbon Agitator Subjected to Steady and Unsteady Rotational Speed, Chemical Engineering Research and Design, 80 (2002) 335-344.
[45] V. Buwa, A. Dewan, A.F. Nassar, F. Durst, Fluid dynamics and mixing of single-phase flow in a stirred vessel with a grid disc impeller: Experimental and numerical investigations, Chemical Engineering Science, 61 (2006) 2815-2822.
[46] A. Dewan, V. Buwa, F. Durst, Performance Optimizations of Grid Disc Impellers for Mixing of Single-Phase Flows in a Stirred Vessel, Chemical Engineering Research and Design, 84 (2006) 691-702.
[47] T. Su, F. Yang, M. Li, K. Wu, Characterization on the hydrodynamics of a covering-plate Rushton impeller, Chinese Journal of Chemical Engineering, 26 (2018) 1392-1400.
[48] A. Khapre, B. Munshi, Data on the mixing of non-Newtonian fluids by a Rushton turbine in a cylindrical tank, Data in Brief, 8 (2016) 1416-1420.
[49] C. Guo, S. Xue, W. Li, H. Qin, J. Guo, J. Zhang, Investigation of power characteristics in a novel cup-shaped-blade mixer, Chemical Engineering and Processing - Process Intensification, 125 (2018) 150-162.
[50] T.T. Devi, B. Kumar, Mass transfer and power characteristics of stirred tank with Rushton and curved blade impeller, Engineering Science and Technology, an International Journal, 20 (2017) 730-737.
[51] F. Magelli, G. Montante, D. Pinelli, A. Paglianti, Mixing time in high aspect ratio vessels stirred with multiple impellers, Chemical Engineering Science, 101 (2013) 712-720.
[52] Z. Jaworski, W. Bujalski, N. Otomo, A.W. Nienow, CFD Study of Homogenization with Dual Rushton Turbines—Comparison with Experimental Results: Part I: Initial Studies, Chemical Engineering Research and Design, 78 (2000) 327-333.
[53] R.K. Grenville, J.J. Giacomelli, G.J. VanOmmeren, C.F. Hastings, M.J. Walters, Blending in above ground storage tanks with side-entering agitators, Chemical Engineering Research and Design, 137 (2018) 395-402.
[54] X. Wang, M. Farhat, L. Fradette, P.A. Tanguy, Analysis of Power Consumption in Multishaft Mixers, Industrial & Engineering Chemistry Research, 53 (2014) 6730-6737.
[55] D. Chapple, S.M. Kresta, A. Wall, A. Afacan, The Effect of Impeller and Tank Geometry on Power Number for a Pitched Blade Turbine, Chemical Engineering Research and Design, 80 (2002) 364-372.

[56] B.E. Rapp, Chapter 25 - Numerical Methods for Linear Systems of Equations, in: B.E. Rapp (Ed.) Microfluidics: Modelling, Mechanics and Mathematics, Elsevier, Oxford, 2017, pp. 497-535.
[57] H.H. Hu, Chapter 10 - Computational Fluid Dynamics, in: P.K. Kundu, I.M. Cohen, D.R. Dowling (Eds.) Fluid Mechanics (Fifth Edition), Academic Press, Boston, 2012, pp. 421-472.
[58] G.L. Lane, Improving the accuracy of CFD predictions of turbulence in a tank stirred by a hydrofoil impeller, Chemical Engineering Science, 169 (2017) 188-211.
[59] M. Taghavi, R. Zadghaffari, J. Moghaddas, Y. Moghaddas, Experimental and CFD investigation of power consumption in a dual Rushton turbine stirred tank, Chemical Engineering Research and Design, 89 (2011) 280-290.
[60] N. Jongpaijit, P. Bumroongsri, Computational Fluid Dynamics Modeling of Temperature Distribution in Fluidized Bed Polymerization Reactor for Polypropylene Production, Energy Procedia, 138 (2017) 901-906.
[61] S.S. Khalafvand, J.D. Voorneveld, A. Muralidharan, F.J.H. Gijsen, J.G. Bosch, T. van Walsum, A. Haak, N. de Jong, S. Kenjeres, Assessment of human left ventricle flow using statistical shape modelling and computational fluid dynamics, Journal of Biomechanics, 74 (2018) 116-125.
[62] A. Mohizin, K.E.R. Roy, D. Lee, S.K. Lee, J.K. Kim, Computational fluid dynamics of impinging microjet for a needle-free skin scar treatment system, Computers in Biology and Medicine, 101 (2018) 61-69.
[63] M. Liu, Age distribution and the degree of mixing in continuous flow stirred tank reactors, Chemical Engineering Science, 69 (2012) 382-393.
[64] X.-c. Cao, T.-a. Zhang, Q.-y. Zhao, Computational simulation of fluid dynamics in a tubular stirred reactor, Transactions of Nonferrous Metals Society of China, 19 (2009) 489-495.
[65] N. Malekjani, S.M. Jafari, Simulation of food drying processes by Computational Fluid Dynamics (CFD); recent advances and approaches, Trends in Food Science & Technology, 78 (2018) 206-223.
[66] D.S. Chandrasekharaiah, L. Debnath, CHAPTER 4 - CONTINUUM HYPOTHESIS, in: D.S. Chandrasekharaiah, L. Debnath (Eds.) Continuum Mechanics, Academic Press, San Diego, 1994, pp. 155-166.
[67] S.N. Fisher, G.R. Pickett, Chapter 3 - Quantum Turbulence in Superfluid 3He at Very Low Temperatures, in: M. Tsubota, W.P. Halperin (Eds.) Progress in Low Temperature Physics, Elsevier2009, pp. 147-194.
[68] X. Cai, H.P. Langtangen, O. Munthe, An Object-Oriented Software Framework for Building Parallel Navier-Stokes Solvers, in: D. Keyes, A. Ecer, J. Periaux, N. Satofuka, P. Fox (Eds.) Parallel Computational Fluid Dynamics 1999, North-Holland, Amsterdam, 2000, pp. 147-154.
[69] P.M. Doran, Chapter 7 - Fluid Flow, in: P.M. Doran (Ed.) Bioprocess Engineering Principles (Second Edition), Academic Press, London, 2013, pp. 201-254.
[70] P. Satya-narayana, R. Avancha, P. Mucci, R. Pletcher, Parallelization and Optimization of a Large Eddy Simulation Code using OpenMP for SGI Origin2000 Performance, in: D. Keyes, A. Ecer, J. Periaux, N. Satofuka, P. Fox (Eds.) Parallel Computational Fluid Dynamics 1999, North-Holland, Amsterdam, 2000, pp. 371-379.
[71] S. Jamshed, Chapter 4 - High Reynolds Number Flows, in: S. Jamshed (Ed.) Using HPC for Computational Fluid Dynamics, Academic Press, Oxford, 2015, pp. 81-100.
[72] E.L. Houghton, P.W. Carpenter, S.H. Collicott, D.T. Valentine, Chapter 9 - Computational Fluid Dynamics, in: E.L. Houghton, P.W. Carpenter, S.H. Collicott, D.T. Valentine (Eds.) Aerodynamics for Engineering Students (Seventh Edition), Butterworth-Heinemann2017, pp. 575-589.
[73] N. Uddin, S.O. Neumann, B. Weigand, LES simulations of an impinging jet: On the origin of the second peak in the Nusselt number distribution, International Journal of Heat and Mass Transfer, 57 (2013) 356-368.
[74] J. Min, Z. Gao, Large Eddy Simulations of Mixing Time in a Stirred Tank, Chinese Journal of Chemical Engineering, 14 (2006) 1-7.

[75] D. Mohotti, K. Wijesooriya, D. Dias-da-Costa, Comparison of Reynolds Averaging Navier-Stokes (RANS) turbulent models in predicting wind pressure on tall buildings, Journal of Building Engineering, 21 (2019) 1-17.
[76] A.K. Seshadri, Statistics of spatial averages and optimal averaging in the presence of missing data, Spatial Statistics, 25 (2018) 1-21.
[77] G. Iaccarino, A. Ooi, P.A. Durbin, M. Behnia, Reynolds averaged simulation of unsteady separated flow, International Journal of Heat and Fluid Flow, 24 (2003) 147-156.
[78] G. Besagni, F. Inzoli, Computational fluid-dynamics modeling of supersonic ejectors: Screening of turbulence modeling approaches, Applied Thermal Engineering, 117 (2017) 122-144.
[79] J.-L. Wu, R. Sun, S. Laizet, H. Xiao, Representation of stress tensor perturbations with application in machine-learning-assisted turbulence modeling, Computer Methods in Applied Mechanics and Engineering, 346 (2019) 707-726.
[80] N. Geneva, N. Zabaras, Quantifying model form uncertainty in Reynolds-averaged turbulence models with Bayesian deep neural networks, Journal of Computational Physics, 383 (2019) 125-147.
[81] J. Derksen, Assessment of Large Eddy Simulations for Agitated Flows, Chemical Engineering Research and Design, 79 (2001) 824-830.
[82] O. Darrigol, Joseph Boussinesq's legacy in fluid mechanics, Comptes Rendus Mécanique, 345 (2017) 427-445.
[83] A.J. Hutchinson, D.P. Mason, Revised Prandtl mixing length model applied to the two-dimensional turbulent classical wake, International Journal of Non-Linear Mechanics, 77 (2015) 162-171.
[84] M. Eckert, Ludwig Prandtl and the growth of fluid mechanics in Germany, Comptes Rendus Mécanique, 345 (2017) 467-476.
[85] B.E. Rapp, Chapter 9 - Fluids, in: B.E. Rapp (Ed.) Microfluidics: Modelling, Mechanics and Mathematics, Elsevier, Oxford, 2017, pp. 243-263.
[86] C.E. Colosqui, A.A. Oberai, Generalized Smagorinsky model in physical space, Computers & Fluids, 37 (2008) 207-217.
[87] T. Ohta, M. Miyashita, DNS and LES with an extended Smagorinsky model for wall turbulence in non-Newtonian viscous fluids, Journal of Non-Newtonian Fluid Mechanics, 206 (2014) 29-39.
[88] W. Layton, Energy dissipation in the Smagorinsky model of turbulence, Applied Mathematics Letters, 59 (2016) 56-59.
[89] D. Shi, M. Li, Z. Li, A nonconforming finite element method for the stationary Smagorinsky model, Applied Mathematics and Computation, 353 (2019) 308-319.
[90] U.C. Goldberg, S.V. Ramakrishnan, A POINTWISE VERSION OF BALDWIN-BARTH TURBULENCE MODEL, International Journal of Computational Fluid Dynamics, 1 (1993) 321-338.
[91] F.R. Menter, Performance of popular turbulence model for attached and separated adverse pressure gradient flows, AIAA Journal, 30 (1992) 2066-2072.
[92] P. Spalart, S. Allmaras, A one-equation turbulence model for aerodynamic flows, 30th Aerospace Sciences Meeting and Exhibit, American Institute of Aeronautics and Astronautics1992.
[93] B. Baldwin, T. Barth, A one-equation turbulence transport model for high Reynolds number wall-bounded flows, 29th Aerospace Sciences Meeting, American Institute of Aeronautics and Astronautics1991.
[94] R. Bali, N. Gupta, Study of non-Newtonian fluid by K–L model through a non-symmetrical stenosed narrow artery, Applied Mathematics and Computation, 320 (2018) 358-370.
[95] Y. Yang, Discussion of “An improved k –ω turbulence model for the simulations of the wind turbine wakes in a neutral atmospheric boundary layer flow” by Ioannis Bouras, Lin Ma, Derek Ingham & Mohamed Pourkashanian, Journal of Wind Engineering and Industrial Aerodynamics, 184 (2019) 458-459.

[96] K. Nakajima, R. Ooka, H. Kikumoto, Evaluation of k-ε Reynolds stress modeling in an idealized urban canyon using LES, Journal of Wind Engineering and Industrial Aerodynamics, 175 (2018) 213-228.
[97] Z. Khan, J.B. Joshi, Comparison of k–ε, RSM and LES models for the prediction of flow pattern in jet loop reactor, Chemical Engineering Science, 127 (2015) 323-333.
[98] Z. Jaworski, B. Zakrzewska, Modelling of the Turbulent Wall Jet Generated by a Pitched Blade Turbine Impeller: The Effect of Turbulence Model, Chemical Engineering Research and Design, 80 (2002) 846-854.
[99] K. Nanan, C. Thianpong, M. Pimsarn, V. Chuwattanakul, S. Eiamsa-ard, Flow and thermal mechanisms in a heat exchanger tube inserted with twisted cross-baffle turbulators, Applied Thermal Engineering, 114 (2017) 130-147.
[100] V.X. Mendoza-Escamilla, A. Alonzo-García, H.R. Mollinedo, I. González-Neria, J. Antonio Yáñez-Varela, S.A. Martinez-Delgadillo, Assessment of k–ε models using tetrahedral grids to describe the turbulent flow field of a PBT impeller and validation through the PIV technique, Chinese Journal of Chemical Engineering, 26 (2018) 942-956.
[101] M. Coroneo, G. Montante, A. Paglianti, F. Magelli, CFD prediction of fluid flow and mixing in stirred tanks: Numerical issues about the RANS simulations, Computers & Chemical Engineering, 35 (2011) 1959-1968.
[102] F. Billard, D. Laurence, A robust k−ε−$\overline{v2}$/k elliptic blending turbulence model applied to near-wall, separated and buoyant flows, International Journal of Heat and Fluid Flow, 33 (2012) 45-58.
[103] S. Jee, K. Shariff, Detached-eddy simulation based on the v2-f model, International Journal of Heat and Fluid Flow, 46 (2014) 84-101.
[104] F. Waschkowski, Y. Zhao, R. Sandberg, J. Klewicki, Multi-objective CFD-driven development of coupled turbulence closure models, Journal of Computational Physics, 452 (2022) 110922.
[105] J.R. Herring, Subgrid Scale Modeling — An Introduction and Overview, in: F. Durst, B.E. Launder, F.W. Schmidt, J.H. Whitelaw (Eds.) Turbulent Shear Flows I, Springer Berlin Heidelberg, Berlin, Heidelberg, 1979, pp. 347-352.
[106] G.A. Gerolymos, I. Vallet, COMPUTATION OF 3-D AEROSPACE CONFIGURATIONS USING A WALL-NORMAL-FREE REYNOLDS-STRESS MODEL, in: W. Rodi, N. Fueyo (Eds.) Engineering Turbulence Modelling and Experiments 5, Elsevier Science Ltd, Oxford, 2002, pp. 371-382.
[107] J. Smagorinsky, GENERAL CIRCULATION EXPERIMENTS WITH THE PRIMITIVE EQUATIONS: I. THE BASIC EXPERIMENT, Monthly Weather Review, 91 (1963) 99-164.
[108] C. Bogey, C. Bailly, Large eddy simulations of round free jets using explicit filtering with/without dynamic Smagorinsky model, International Journal of Heat and Fluid Flow, 27 (2006) 603-610.
[109] R.B. Bird, W.E. Stewart, E.N. Lightfoot, Transport Phenomena, Wiley2006.
[110] J. Tu, G.-H. Yeoh, C. Liu, Chapter 3 - Governing Equations for CFD: Fundamentals, in: J. Tu, G.-H. Yeoh, C. Liu (Eds.) Computational Fluid Dynamics (Third Edition), Butterworth-Heinemann2018, pp. 65-124.
[111] G.H. Yeoh, J. Tu, Chapter 2 - Governing Equations and Boundary Conditions, in: G.H. Yeoh, J. Tu (Eds.) Computational Techniques for Multiphase Flows, Butterworth-Heinemann, Oxford, 2010, pp. 21-94.
[112] L. Prandtl, Applications of modern hydrodynamics to aeronautics, US Government Printing Office1925.
[113] E.R. Van Driest, On Turbulent Flow Near a Wall, Journal of the Aeronautical Sciences, 23 (1956) 1007-1011.
[114] T. Cebeci, 4 - General Behavior of Turbulent Boundary Layers, in: T. Cebeci (Ed.) Analysis of Turbulent Flows, Elsevier, Oxford, 2004, pp. 81-140.

[115] P.-A. Krogstad, Modification of the van Driest damping function to include the effects of surface roughness, AIAA Journal, 29 (1991) 888-894.
[116] Ansys, ANSYS Fluent Theory Guide, ANSYS Fluent Theory Guide, (2013) 1-780.
[117] B.E. Launder, B.I. Sharma, Application of the energy-dissipation model of turbulence to the calculation of flow near a spinning disc, Letters in Heat and Mass Transfer, 1 (1974) 131-137.
[118] M.M. Rahman, N. Tanaka, S. Yokobori, S. Hirai, Three Dimensional Numerical Analysis of Two Phase Flow Separation Using Swirling Fluidics, Energy and Power Engineering, 5 (2013) 301-306.
[119] W.C. Reynolds, Fundamentals of Turbulence for Turbulence Modeling and Simulation, 1987.
[120] B. Zhang, C. Liang, A simple, efficient, and high-order accurate curved sliding-mesh interface approach to spectral difference method on coupled rotating and stationary domains, Journal of Computational Physics, 295 (2015) 147-160.
[121] P.A.S.F. Silva, P. Tsoutsanis, A.F. Antoniadis, Simple multiple reference frame for high-order solution of hovering rotors with and without ground effect, Aerospace Science and Technology, 111 (2021) 106518.
[122] B.E. Rapp, Chapter 31 - Finite Volume Method, in: B.E. Rapp (Ed.) Microfluidics: Modelling, Mechanics and Mathematics, Elsevier, Oxford, 2017, pp. 633-654.
[123] F.E. Harris, Chapter 7 - Vector Analysis, in: F.E. Harris (Ed.) Mathematics for Physical Science and Engineering, Academic Press, Boston, 2014, pp. 229-292.
[124] 10 - Vector Field Theory, in: A. Jeffrey, D. Zwillinger, I.S. Gradshteyn, I.M. Ryzhik (Eds.) Table of Integrals, Series, and Products (Seventh Edition), Academic Press, Boston, 2007, pp. 1049-1058.
[125] A.F.M. Alkarkhi, W.A.A. Alqaraghuli, Chapter 9 - Factor Analysis, in: A.F.M. Alkarkhi, W.A.A. Alqaraghuli (Eds.) Easy Statistics for Food Science with R, Academic Press2019, pp. 143-159.
[126] N. Martín-Calvo, M.Á. Martínez-González, Dietary Patterns, in: P. Ferranti, E.M. Berry, J.R. Anderson (Eds.) Encyclopedia of Food Security and Sustainability, Elsevier, Oxford, 2019, pp. 283-291.
[127] L. Liu, Application of ultrasound spectroscopy for nanoparticle sizing in high concentration suspensions: A factor analysis on the effects of concentration and frequency, Chemical Engineering Science, 64 (2009) 5036-5042.
[128] E.M.a.B. Marshall, A, In Handbook of Industrial Mixing, In Handbook of Industrial Mixing2004, pp. 247-343.
[129] C.-Y. Xu, Z. Sun, Y.-T. Zhang, J.-H. Sun, Improvement of the scale-adaptive simulation technique based on a compensated strategy, European Journal of Mechanics - B/Fluids, 81 (2020) 1-14.
[130] D. Lopes, R. Agujetas, H. Puga, J. Teixeira, R. Lima, J.P. Alejo, C. Ferrera, Analysis of finite element and finite volume methods for fluid-structure interaction simulation of blood flow in a real stenosed artery, International Journal of Mechanical Sciences, 207 (2021) 106650.
[131] M. Tripathi, S.K. Singal, Allocation of weights using factor analysis for development of a novel water quality index, Ecotoxicology and Environmental Safety, 183 (2019) 109510.
[132] A.M.S. Hamouda, M.S. Risby, 4 - Modeling ballistic impáct, in: A. Bhatnagar (Ed.) Lightweight Ballistic Composites, Woodhead Publishing2006, pp. 101-126.
[133] A. Tamrakar, D.R. Devarampally, R. Ramachandran, Chapter 7 - Advanced multiphase hybrid model development of fluidized bed wet granulation processes, in: R. Singh, Z. Yuan (Eds.) Computer Aided Chemical Engineering, Elsevier2018, pp. 159-187.
[134] R. Verma, S. Ghosh, Two-Phase Flow in Miniature Geometries: Comparison of Gas-Liquid and Liquid-Liquid Flows, 6 (2019) 5-16.
[135] H.T. Bi, J.R. Grace, Flow regime diagrams for gas-solid fluidization and upward transport, International Journal of Multiphase Flow, 21 (1995) 1229-1236.
[136] F. Xie, W. Zhao, D. Wan, Numerical simulations of liquid-solid flows with free surface by coupling IMPS and DEM, Applied Ocean Research, 114 (2021) 102771.

[137] Z. Mei, X. Cheng, Modeling of interfacial area for single deformed bubble based on VOF method, Nuclear Engineering and Design, 395 (2022) 111864.
[138] D. Drew, R. Lahey, In Particulate Two-Phase Flow,'1993, Butternorth-Heinemann, Boston, 506-566.
[139] S.K. Naeeni, L. Pakzad, Droplet size distribution and mixing hydrodynamics in a liquid–liquid stirred tank by CFD modeling, International Journal of Multiphase Flow, 120 (2019) 103100.
[140] G.A. Olatunde, O.O. Fasina, Influence of drag equations on computational fluid dynamic modeling of fluidization behavior of loblolly pine wood grinds, Renewable Energy, 139 (2019) 651-660.
[141] X. Guan, X. Li, N. Yang, M. Liu, CFD simulation of gas-liquid flow in stirred tanks: Effect of drag models, Chemical Engineering Journal, 386 (2020) 121554.
[142] A. Kaufmann, Towards eulerian-eulerian large eddy simulation of reactive two-phase flows, (2004).
[143] F.W. ROOS, W.W. WILLMARTH, Some experimental results on sphere and disk drag, AIAA Journal, 9 (1971) 285-291.
[144] A.W. Pacek, C.C. Man, A.W. Nienow, On the Sauter mean diameter and size distributions in turbulent liquid/liquid dispersions in a stirred vessel, Chemical Engineering Science, 53 (1998) 2005-2011.
[145] P. Kowalczuk, J. Drzymala, Physical Meaning of the Sauter Mean Diameter of Spherical Particulate Matter, Particulate Science and Technology, 34 (2015) 645-647.
[146] X. Cao, K. Yang, H. Wang, J. Bian, Gas–liquid–hydrate flow characteristics in vertical pipe considering bubble and particle coalescence and breakage, Chemical Engineering Science, 252 (2022) 117249.

12 Appendix

Table 12-1 length of the x axis line location lines

Baffle configuration	Length of x axis line location (m)
4:1	0.9
unbaffled	1.08
1:2	0.99
1:1	0.9
2:1	0.9
Normal distribution baffle	0.9
Error function baffle	0.9

Appendix A – The code used to calculate the optimised simulation settings.

```
In[1]:= << DPA`

In[2]:= dir = SetDirectory["/Users/landeliu/Desktop/PhD Weekly reports/Nico"]

Out[2]= /Users/landeliu/Desktop/PhD Weekly reports/Nico

In[7]:= file = FileNameJoin[{dir, "GridSizeConvergingTime.txt"}]

Out[7]= /Users/landeliu/Desktop/PhD Weekly reports/Nico/GridSizeConvergingTime.txt

In[8]:= raw = Import[file, "Table"]

Out[8]= {{0.0005, 0.00075, 0.001, 0.0015, 0.002, 0.0025, 0.003, 0.0035},
         {1, 4009.17, 3815.49, 3332.88, 2343.07, 2254.09, 2380.21, 1600.58, 1489.74},
         {1.25, 2055.7, 1510.61, 1856.43, 1456.68, 783.825, 770.234, 790.572, 670.421},
         {1.5, 1637.47, 784.307, 631.29, 624.48, 492.391, 388.819, 384.398, 373.212},
         {1.75, 3250.82, 523.871, 394.349, 355.33, 319.098, 276.807, 190.109, 182.114}}

In[9]:= residuals = raw[[1]]

Out[9]= {0.0005, 0.00075, 0.001, 0.0015, 0.002, 0.0025, 0.003, 0.0035}

In[10]:= gridsizes = Transpose[Drop[raw, 1]][[1]]

Out[10]= {1, 1.25, 1.5, 1.75}

In[11]:= data = Transpose[Drop[Transpose[Drop[raw, 1]], 1]]

Out[11]= {{4009.17, 3815.49, 3332.88, 2343.07, 2254.09, 2380.21, 1600.58, 1489.74},
          {2055.7, 1510.61, 1856.43, 1456.68, 783.825, 770.234, 790.572, 670.421},
          {1637.47, 784.307, 631.29, 624.48, 492.391, 388.819, 384.398, 373.212},
          {3250.82, 523.871, 394.349, 355.33, 319.098, 276.807, 190.109, 182.114}}

In[12]:= dataset = {gridsizes, residuals, data, {{}, {}, {}, {}, {}, {}}}

Out[12]= {{1, 1.25, 1.5, 1.75},
          {0.0005, 0.00075, 0.001, 0.0015, 0.002, 0.0025, 0.003, 0.0035},
          {{4009.17, 3815.49, 3332.88, 2343.07, 2254.09, 2380.21, 1600.58, 1489.74},
           {2055.7, 1510.61, 1856.43, 1456.68, 783.825, 770.234, 790.572, 670.421},
           {1637.47, 784.307, 631.29, 624.48, 492.391, 388.819, 384.398, 373.212},
           {3250.82, 523.871, 394.349, 355.33, 319.098, 276.807, 190.109, 182.114}},
          {{}, {}, {}, {}, {}, {}}}

In[13]:= {cst, evs, coms, facs, scos, res} = FactorAnalysis[dataset, ExtractedFactors → 2]
```

```
ExtractedFactors has been assigned a value
  larger than 1, EigenValueLimit option will not take any effect.

Datasets evolution at top level is: {1., 1.25, 1.5, 1.75}.
```

Out[13]=
```
{{1., 1.25, 1.5, 1.75},
 {{1, 7.30451, 0.919738, 0.919738}, {2, 0.637438, 0.0802622, 1.}},
 {0.996158, 0.997425, 0.985568, 0.984458, 0.987543, 0.992914, 0.999908, 0.997976},
 {{-0.298367, -0.910673, -0.951085, -0.967941, -0.891557, -0.884517,
   -0.953292, -0.942574}, {-0.952437, -0.41, -0.284614, -0.218057,
   -0.43894, -0.45885, -0.301899, -0.330954}}, {{1.45582, 3.80193},
  {-0.969728, -0.498311}, {-0.751143, -1.81648}, {0.265047, -1.48713}},
 {{0., -0.00314512, 0.00744586, 0.00772694, -0.00691781, -0.00521723,
   0.000595407, -0.00278824}, {-0.00314512, 2.22045×10^-16, -0.00609599,
   -0.00632611, 0.00566367, 0.00427139, -0.000487465, 0.00228276},
  {0.00744586, -0.00609599, 0., 0.0149767, -0.0134084, -0.0101123,
   0.00115404, -0.00540429}, {0.00772694, -0.00632611, 0.0149767,
   4.44089×10^-16, -0.0139145, -0.010494, 0.00119761, -0.0056083},
  {-0.00691781, 0.00566367, -0.0134084, -0.0139145, 0., 0.0093951,
   -0.0010722, 0.00502102}, {-0.00521723, 0.00427139, -0.0101123,
   -0.010494, 0.0093951, -3.33067×10^-16, -0.000808625, 0.00378672},
  {0.000595407, -0.000487465, 0.00115404, 0.00119761, -0.0010722,
   -0.000808625, 0., -0.000432153}, {-0.00278824, 0.00228276, -0.00540429,
   -0.0056083, 0.00502102, 0.00378672, -0.000432153, -2.22045×10^-16}}}
```

In[14]:=
```
evs
```

Out[14]=
```
{{1, 7.30451, 0.919738, 0.919738}, {2, 0.637438, 0.0802622, 1.}}
```

In[15]:=
```
facs
```

Out[15]=
```
{{-0.298367, -0.910673, -0.951085, -0.967941,
  -0.891557, -0.884517, -0.953292, -0.942574}, {-0.952437, -0.41,
  -0.284614, -0.218057, -0.43894, -0.45885, -0.301899, -0.330954}}
```

In[16]:=
```
ListPlot[Transpose[{residuals, facs[[1]]}]]
```

Out[16]=

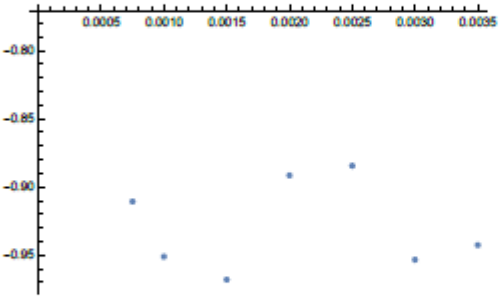

In[17]:=
```
BarChart[facs[[1]]]
```

Out[17]=

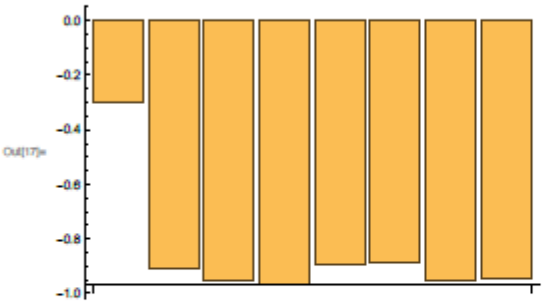

In[18]:=
```
BarChart[facs[[2]]]
```

Out[18]=

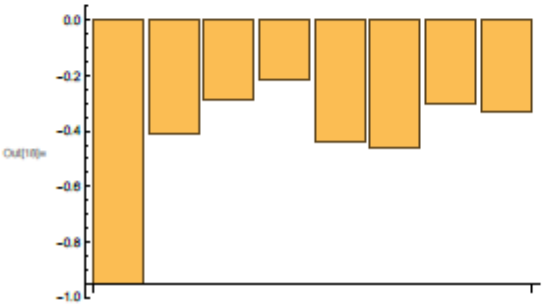

In[19]:=
```
facsplot = ListPlot[Transpose[facs], AxesOrigin → {-1, 0}, PlotRange → All]
```

Out[19]=

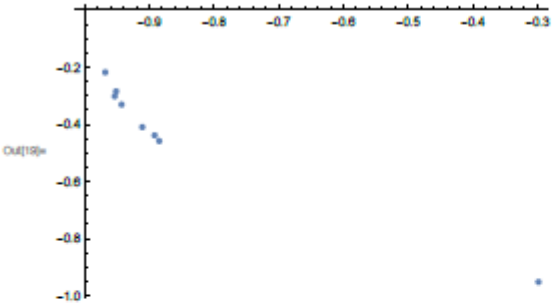

In[20]:=
```
scos
```

Out[20]=
```
{{1.45582, 3.80193}, {-0.969728, -0.498311},
 {-0.751143, -1.81648}, {0.265047, -1.48713}}
```

In[21]:=
```
ListPlot[scos, PlotStyle → PointSize[0.03]]
```

Out[21]=

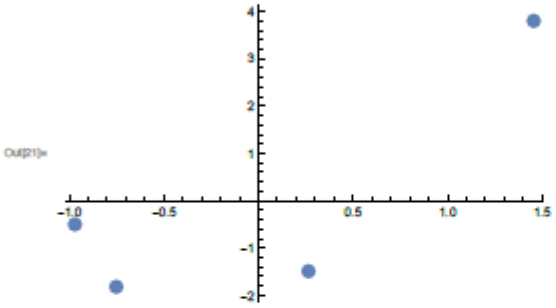

In[24]:=
```
scostrans = Transpose[scos]
```

Out[24]=
```
{{1.45582, -0.969728, -0.751143, 0.265047},
 {3.80193, -0.498311, -1.81648, -1.48713}}
```

In[25]:=
```
GsizeScoFl = Transpose[{gridsizes, scostrans[[1]]}]
```

Out[25]=
```
{{1, 1.45582}, {1.25, -0.969728}, {1.5, -0.751143}, {1.75, 0.265047}}
```

In[28]:=
```
GsizeScoFlp = ListPlot[GsizeScoFl, PlotStyle → PointSize[0.03]]
```

Out[28]=

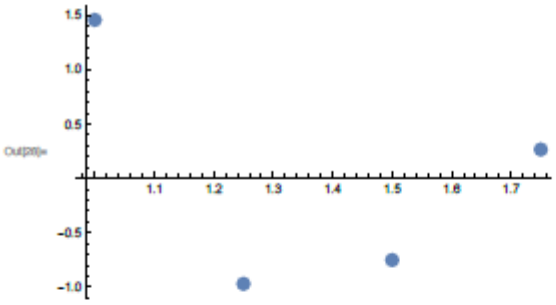

In[39]:=
```
GsizeScoFlfit = NonlinearModelFit[GsizeScoFl,
    a x^4 + b x^3 + c x^2 + d x + f, {a, b, c, d, f}, x] // Normal
```

Out[39]=
$$48.1677 - 68.3089\,x + 5.13124\,x^2 + 24.492\,x^3 - 8.03425\,x^4$$

```
In[46]:= GsizeScoFlfitp = Plot[GsizeScoFlfit, {x, 1, 1.75}]
```

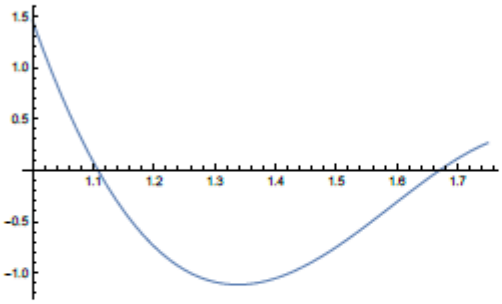


```
In[47]:= Show[GsizeScoFlfitp, GsizeScoFlp]
```

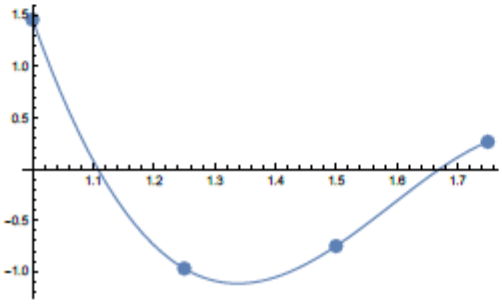


```
In[48]:= Solve[D[GsizeScoFlfit, {x, 1}] == 0, x]
Out[48]= {{x → -0.872372}, {x → 1.33826}, {x → 1.82045}}
```

This gives you with grid size = 1.34, the convergence time could be minimised.

```
In[50]:= data2 = Drop[Transpose[Drop[raw, 1]], 1]
Out[50]= {{4009.17, 2055.7, 1637.47, 3250.82}, {3815.49, 1510.61, 784.307, 523.871},
  {3332.88, 1856.43, 631.29, 394.349}, {2343.07, 1456.68, 624.48, 355.33},
  {2254.09, 783.825, 492.391, 319.098}, {2380.21, 770.234, 388.819, 276.807},
  {1600.58, 790.572, 384.398, 190.109}, {1489.74, 670.421, 373.212, 182.114}}

In[52]:= dataset2 = {residuals, gridsizes, data2, {}}
Out[52]= {{0.0005, 0.00075, 0.001, 0.0015, 0.002, 0.0025, 0.003, 0.0035},
  {1, 1.25, 1.5, 1.75},
  {{4009.17, 2055.7, 1637.47, 3250.82}, {3815.49, 1510.61, 784.307, 523.871},
   {3332.88, 1856.43, 631.29, 394.349}, {2343.07, 1456.68, 624.48, 355.33},
   {2254.09, 783.825, 492.391, 319.098}, {2380.21, 770.234, 388.819, 276.807},
   {1600.58, 790.572, 384.398, 190.109}, {1489.74, 670.421, 373.212, 182.114}}, {}}
```

```
In[53]:= {cst2, evs2, coms2, facs2, scos2, res2} =
          FactorAnalysis[dataset2, ExtractedFactors → 2]

         ExtractedFactors has been assigned a value
           larger than 1, EigenValueLimit option will not take any effect.

         Datasets evolution at top level is:
           {0.0005, 0.00075, 0.001, 0.0015, 0.002, 0.0025, 0.003, 0.0035}.

Out[53]= {{0.0005, 0.00075, 0.001, 0.0015, 0.002, 0.0025, 0.003, 0.0035},
          {{1, 3.37639, 0.874146, 0.874146}, {2, 0.486109, 0.125854, 1.}},
          {0.937009, 0.933706, 0.994876, 0.996905},
          {{-0.89301, -0.881746, -0.532561, -0.332929},
           {-0.373553, -0.395261, -0.843359, -0.941389}},
          {{4.21824, 1.75977}, {0.356044, 0.519378}, {-0.533655, -0.546354},
           {-0.619579, -0.507107}, {-0.507173, 0.0110333},
           {-0.740808, -0.168234}, {-1.09521, -0.573401}, {-1.07786, -0.495084}},
          {{2.22045 × 10^-16, -0.0643722, -0.000719294, 0.00267705},
           {-0.0643722, 0., -0.000880348, -0.00150262},
           {-0.000719294, -0.000880348, 0., -0.00393587},
           {0.00267705, -0.00150262, -0.00393587, 0.}}}

In[54]:= scos2

Out[54]= {{4.21824, 1.75977}, {0.356044, 0.519378},
          {-0.533655, -0.546354}, {-0.619579, -0.507107}, {-0.507173, 0.0110333},
          {-0.740808, -0.168234}, {-1.09521, -0.573401}, {-1.07786, -0.495084}}

In[57]:= ResScoFl = Transpose[{residuals, Transpose[scos2][[1]]}]

Out[57]= {{0.0005, 4.21824}, {0.00075, 0.356044}, {0.001, -0.533655}, {0.0015, -0.619579},
          {0.002, -0.507173}, {0.0025, -0.740808}, {0.003, -1.09521}, {0.0035, -1.07786}}

In[58]:= ResScoFlp = ListPlot[ResScoFl, PlotStyle → PointSize[0.03]]

Out[58]=
```

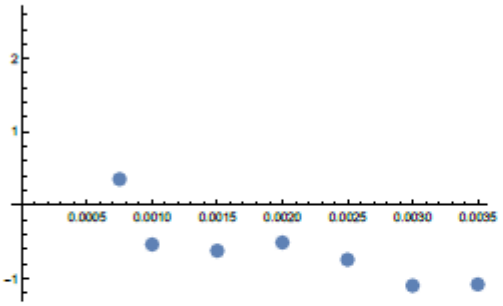


```
In[65]:= ResScoFlfit = NonlinearModelFit[ResScoFl,
           a x^4 + b x^3 + c x^2 + d x + f, {a, b, c, d, f}, x] // Normal

Out[65]= 18.1837 - 42 275.3 x + 3.2713 × 10^7 x^2 - 1.04533 × 10^10 x^3 + 1.17431 × 10^12 x^4
```

```
In[66]:= ResScoFlfitp = Plot[ResScoFlfit, {x, 0.0005, 0.0035}]
```

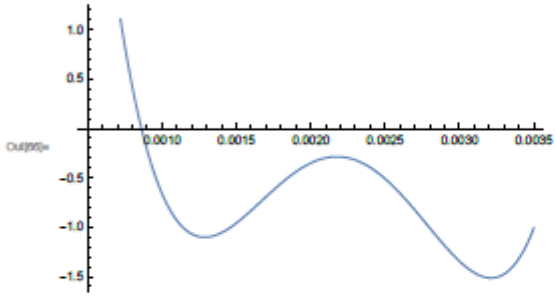


```
In[67]:= Show[ResScoFlfitp, ResScoFlp]
```

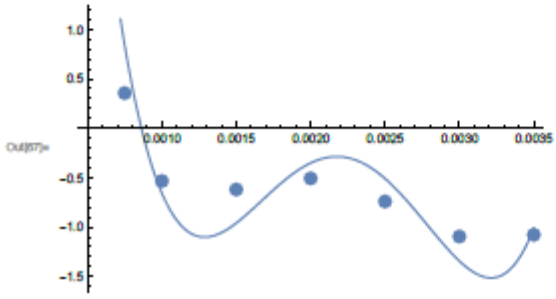


```
In[68]:= Solve[D[ResScoFlfit, {x, 1}] == 0, x]
Out[68]= {{x → 0.00128725}, {x → 0.00217623}, {x → 0.00321274}}
```

This tells you with residual = 0.0013, the convergence time could be minimised. We cannot take residual = 0.0032 as it would possibly too rough. So the conclusion from this analysis is that to optimise the simulation, grid size = 1.34 residual = 0.0013.